Alexandrov RESEARCH INSTITUTE OF TECHNOLOGY
NITI

Phase diagrams for multicomponent systems containing corium and products of its interaction with NPP materials

(CORPHAD)

Phase 2

INVESTIGATION OF TERNARY METAL-OXIDIC SYSTEMS: SYSTEM Fe–Zr–O

PROGRESS REPORT

01/05/06 – 30/11/06

Project title	Phase diagrams for multicomponent systems containing corium and products of its interaction with NPP materials (CORPHAD, 1950.2)	
Commissioned by	ISTC	
File specification	CORPHAD/RCP-0604	
Implementing organization	The Alexandrov Research Institute of Technology (NITI) of the Atomic Energy Agency of the Russian Federation NITI, Sosnovy Bor, 188540 Leningrad Region, Russia	
Project manager	Name	Yu. N. Aniskevich
	Signature	
	Signature	November, 2006

Authors

Dr., Prof.	V. B. Khabensky
Dr.	S. V. Bechta
Ph.D.	V. S. Granovsky
Prof, Corr.Mem. RAS	V. V. Gusarov
	V. I. Almyashev
	S. A. Vitol
	E. V. Krushinov
Dr., Prof.	Yu. B. Petrov
Ph.D.	S. Yu. Kotova
Ph.D.	A.A. Sulatsky
Ph. D.	I. V. Kulagin
Ph. D.	D. B. Lopukh
Ph.D.	L. P. Mezentseva
	E. K. Kalyago
	V. V. Martynov
	A. V. Lysenko
	R. A. Kosarevsky
	E. V. Shevchenko
	V. G. Bliznyuk
	V. R. Bulygin
	E. M. Belyaeva
	N. E. Kamensky

CONTENTS

Introduction

The present work has been carried out within the ISTC CORPHAD Project in order to specify phase diagrams of corium-based systems and products of its interaction with NPP materials. The availability of credible information about phase equilibria in such systems is very important for a consistent prediction of physicochemical phenomena taking place in a faulty nuclear reactor during the core heatup and meltdown, molten pool formation and evolution, as well as also in the cases of melt interaction with materials limiting its attitude position.

The metal-oxidic system Zr–Fe-O is one of the basic systems essential for the reliable determination of phase ratios during the in-vessel retention of corium. Due to an extremely high chemical activity of melts in the concentration domain of interest, such systems can be investigated only in an inert atmosphere or in the atmosphere with regulated partial pressure of oxygen, and only by applying the cold crucible technology. In addition to the mentioned peculiarity, this system is prone to stratification /1/, as is shown by thermodynamic calculations. The published sources offer no experimental data for the concentration domain of interest. These circumstances considerably complicate methodologies of both melt preparation, manipulation and investigation.

The present work was aimed at the experimental evaluation of liquidus and solidus temperatures (T_{liq} and T_{sol}) for the compositions recommended by the CORPHAD collaborators, and at identifying compositions of the liquids that coexist in the miscibility gap. Besides, peculiarities of crystallization of melts at different cooling rates were investigated.

In order to make a preliminary evaluation of an equilibrium composition for the investigated compositions, the authors performed thermodynamic calculations using the GEMINI-2 code and NUCLEA-05 database.

The results offered in the present report have been obtained from an experimental series and are meant for updating the phase diagram database.

1. State of the art review

The binary diagram of the Zr-O system has been investigated by many authors (see list of publications in /2/). The ZrO_2 phases in their monoclinic (baddeleyite), tetragonal and cubic modifications are the most well-studied within the system. It is also mentioned in literature sources that there exist the Zr solid solution in ZrO_2, oxygen solid solution in α-Zr and in β-Zr, as well as phases of Zr_6O and Zr_3O. The data on the existence of phases of ZrO, Zr_2O, Zr_2O_3 are doubtful.

Fig. 1.1 offers two early versions of a phase diagram for the Zr-O system, which are based on the data from /3, 4/ and differ mainly by the limit of oxygen solubility in zirconium. In /5/ the stress was made on studying the more oxygen-rich part of the diagram (Fig. 1.2).

In the late 70s the diagram was specified (the eutectic point, limits of oxygen solubility in zirconium) and new data were obtained for the high-temperature domain on the side of ZrO_2 /6/ (Fig. 1.3).

More detailed investigation of the high-temperature domain and the domain of oxygen solid solutions in α-Zr were carried out by the authors of /7/ (Fig. 1.4).

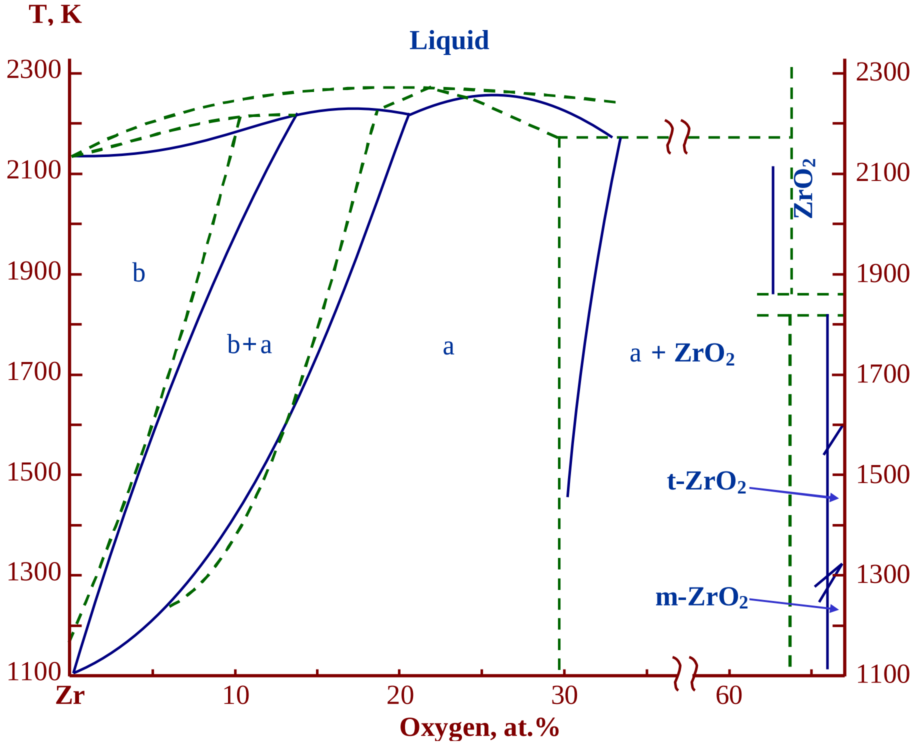

Fig. 1.1. Phase diagram of the Zr-O system according to – – – /3/ and ——/4/

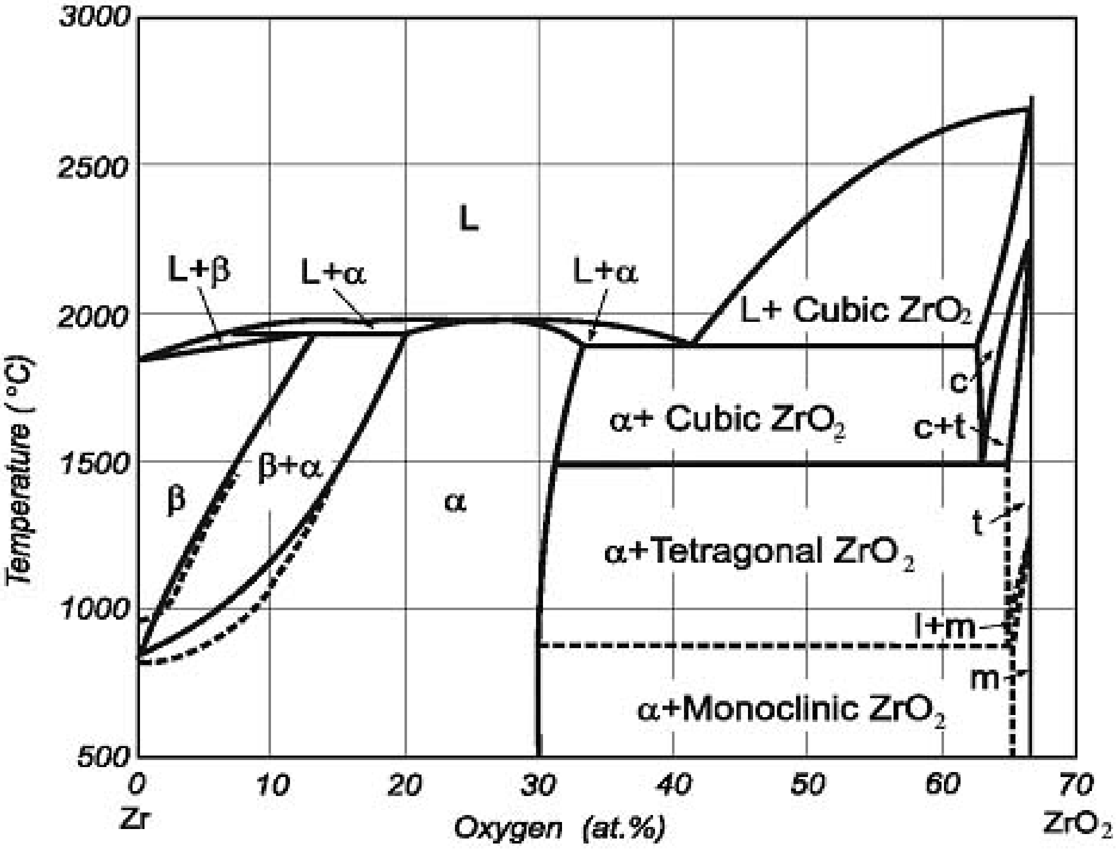

Fig. 1.2. Phase diagram of the Zr-O system according to /5/

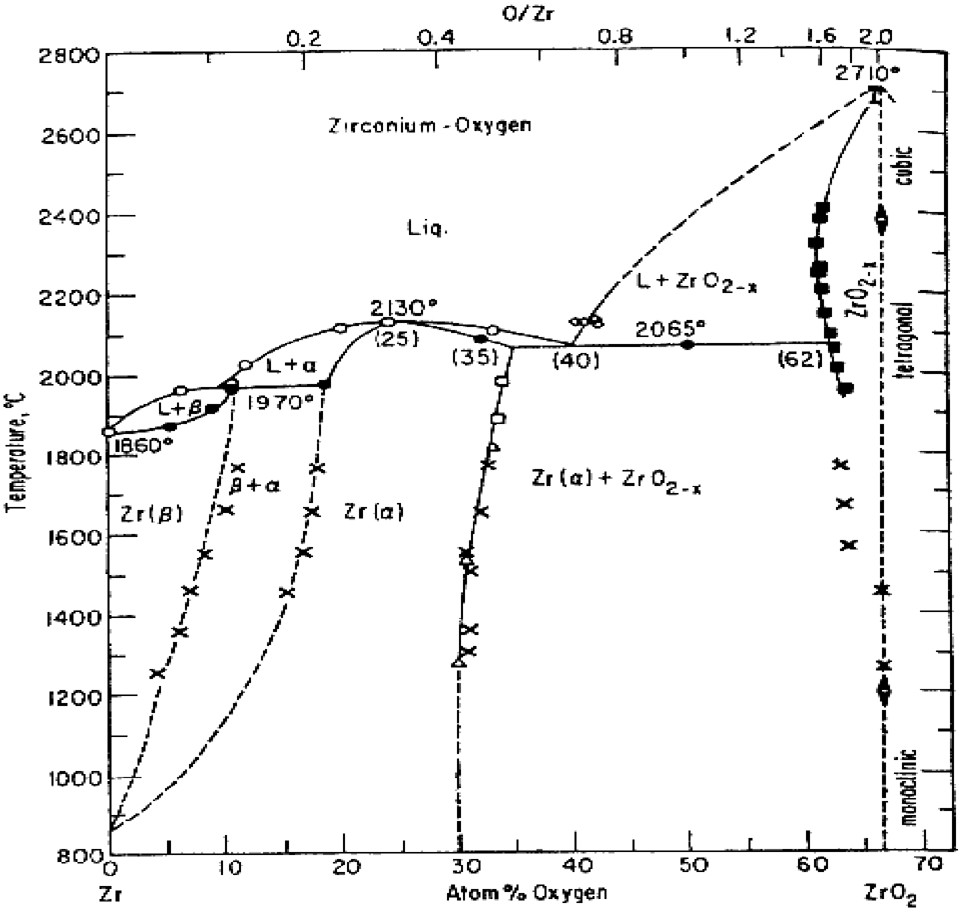

Fig. 1.3. Phase diagram of the Zr-O system according to /6/

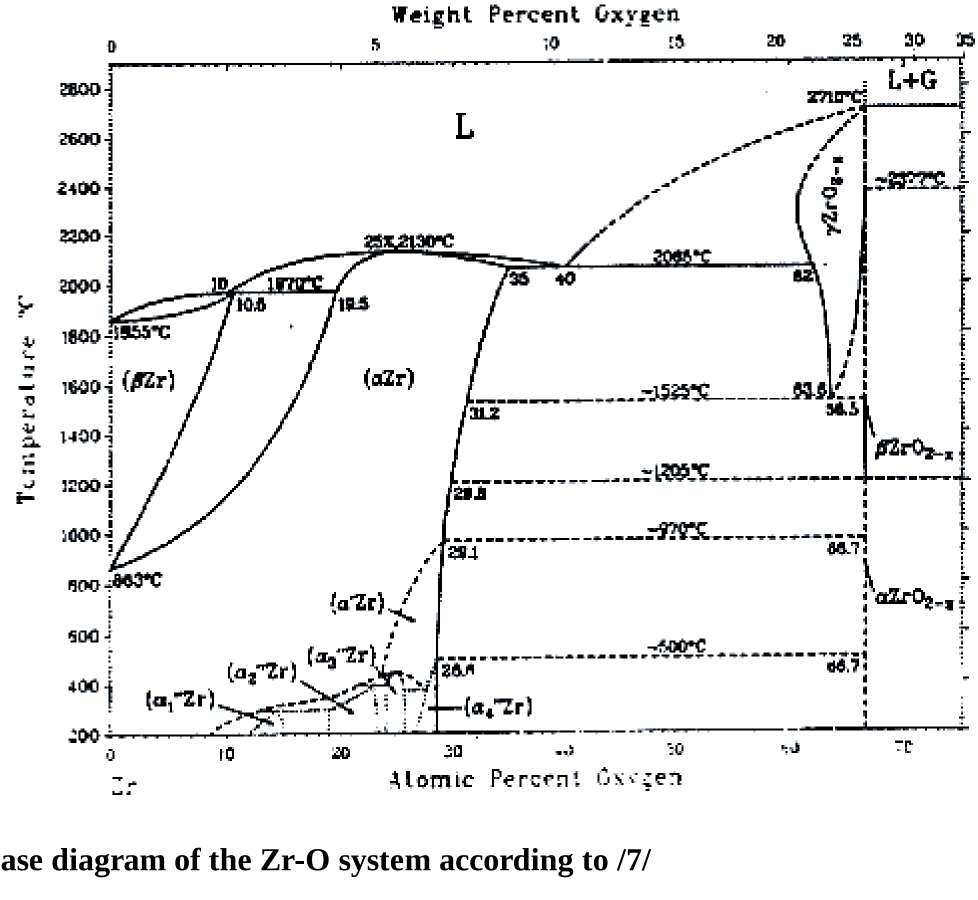

Fig. 1.4. Phase diagram of the Zr-O system according to /7/

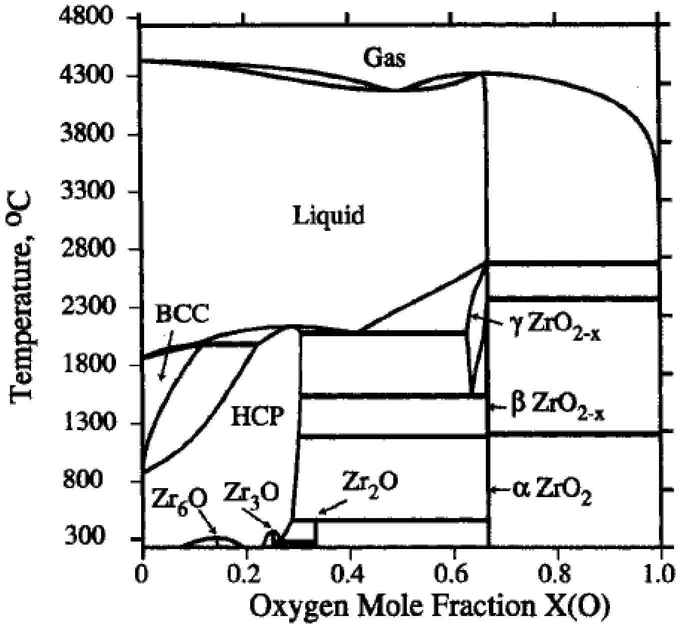

Fig. 1.5. Phase diagram of the Zr-O system according to /8/

The work /8/ is noteworthy. Its authors performed thermodynamic modeling of phase equilibria in the Zr-O system (Fig. 1.5). Of special importance in this work is the prediction of temperature boundaries of Zr_6O and Zr_3O existence, and of the limits of the α-Zr-based solid solution solubility in the said compounds.

The performed investigations are numerous, but still there remain unclear questions about the limits of phases existence in the system, and even about the possible existence of phases which are not represented in any known phase diagram.

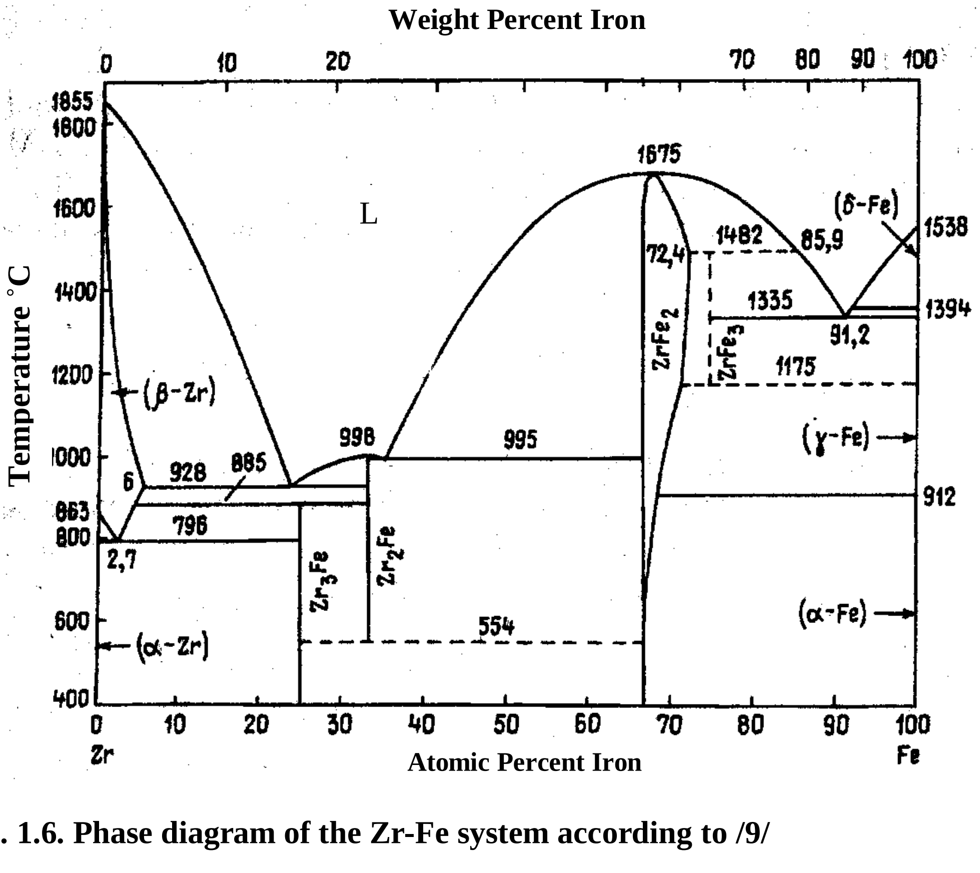

Fig. 1.6. Phase diagram of the Zr-Fe system according to /9/

The binary system Zr-Fe has also been the subject of numerous studies. A generalized phase diagram (Fig. 1.6), constructed using data of different authors, is given in /9/. The diagram indicates four intermetallic phases, namely Zr_3Fe, Zr_2Fe, $ZrFe_2$ and $ZrFe_3$. The intermetallide $ZrFe_2$ is stable within 66.0 through 72.9 at. % Fe and melts congruently at 1675ºC. According to different authors, the maximum solubility of Fe in β-Zr is about 6 at. %.

The binary diagram of the Fe–O system, a fundamental one for many metallurgical processes, has been studied sufficiently well. High-temperature equilibria between metallic iron and its oxides have been most comprehensively studied in /10/. The area of stratification stretches from 0.4 up to 50 at. % of O (Fig. 1.4). Note the insignificant solubility of oxygen in Fe, which grows with the increasing temperature.

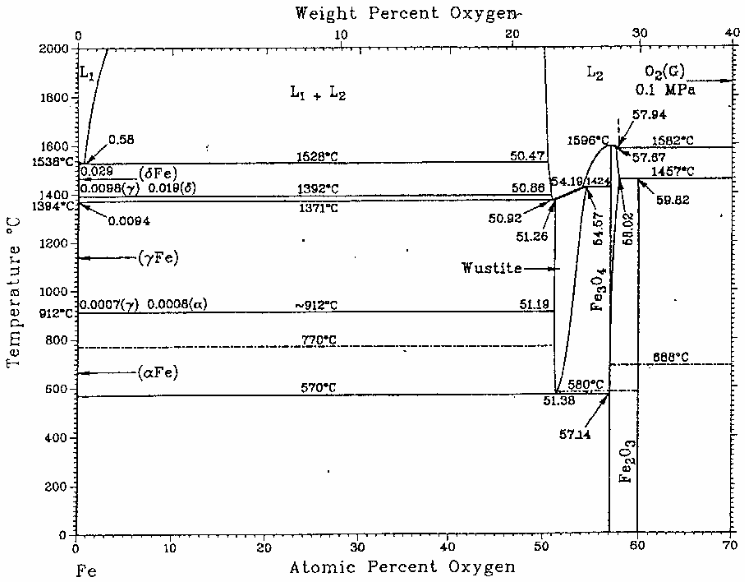

Fig. 1.7. Phase diagram of the Zr-O system according to /10/ at a pressure of 1 atm.

A study of a particular section of the Zr-Fe-O system in the binary oxidic system ZrO_2-$FeO_{1.33}$ in air (Fig. 1.8) has been performed within the framework of ECOSTAR Project /12/. Miscibility gap has been shown in this diagram. It adjoins the oxidic corner of the Zr-Fe-O system and contains no metallic or metal-rich melts. Nevertheless, it also demonstrates the complex nature of the whole system that requires investigation.

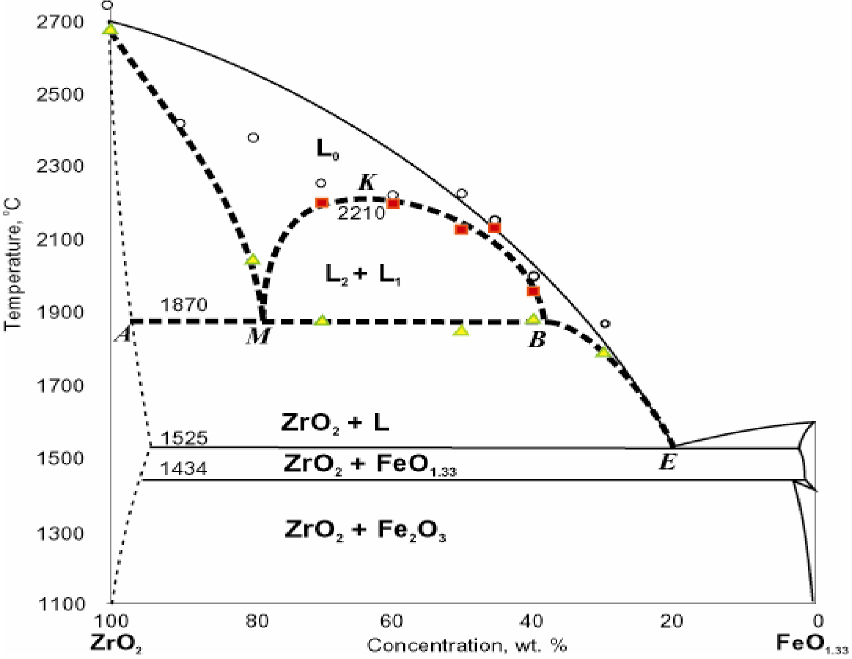

Continuous lines –data of /11/; dotted lines – results from /12/

Fig. 1.8. Pseudobinary diagram for the ZrO_2–$FeO_{1.33}$ system

Binary diagrams illustrate a complex structure of both the subsolidus domain, and of the liquidus surface of a ternary system.

2. Experimental methodologies and description of facilities

The facilities and detailed descriptions of experimental methodologies are given in /13/. Measurements of T_{liq} was performed by means of visual polythermal analysis in the cold crucible (VPA IMCC). Determination of T_{sol} was made by the method of differential thermal analysis (DTA) using the SETARAM analyzer. Compositions of the coexisting liquids were determined using the results of the physicochemical analysis of ingots and samples produced by IMCC.

3. Description and results of tests

3.1. Analysis of initial charge materials

When preparing the test, the charge components, i.e., zirconia, metallic zirconium and iron, were checked for the main substance and impurities content.

The composition of charge components is given in Tab. 3.1.

Table. 3.1. Charge components

Components	Main substance content, %	Impurities, mass %	Notes
ZrO_2 powder, <100 mm dispersivity	(ZrO_2+HfO_2) >99.3	$Al_2O_3<0.03$; $Fe_2O_3<0.05$; $CaO<0.03$; $MgO<0.02$; $SiO_2<0.2$; $TiO_2<0.1$; $P_2O_5<0.15$; $(Na_2O+K_2O)<0.02$.	Certificate data
metallic Fe	>99.9	Si-0.0005; Mg-0.0001; Cu-0.0001; Ni-0.019; Pb-0.0001; Zn-0.00028	Certificate data
metallic Zr **(alloy Nb-1)**	>99.0	Nb<1.0	XRF results

3.2. Experimental matrix

The matrix of the performed tests is presented in Tab. 3.2.

Table 3.2. Experimental matrix

CORD	Charge composition			Mass, g	Test objective
	Zr	Fe	O		
	mass %/at.%				
30[1)]	74.1/49	17.6/19	8.3/32	407.1	$T_{liq.}$ measurements, tie-lines
33[1)]	74.1/49	17.6/19	8.3/32	407.0	
35[1)]	74.1/49	17.6/19	8.3/32	407.0	$T_{liq.}$ measurements, equilibrium crystallization of ingot
39	68.7/45	23.3/25	8.0/30	399.9	$T_{liq.}$ measurements, tie-lines
44[2)]	81.1/63	14.7/19	4.2/18	321.5	$T_{liq.}$ measurements
45	43.9/30	53.6/60	2.6/10	326.5	$T_{liq.}$ measurements, tie-lines

[1)] - ZrO_2 was introduced into the crucible in a larger quantity, as an allowance was made for that part of ZrO_2 that would crystallize during crust formation. Therefore, the charge composition slightly differs from the specified composition, it being at. %: 50-Zr; 20-Fe; 30-O.

[2)] – because of crust formation on the crucible sections during melting. To melt the crust and raise level of the melt, ZrO_2 (m=12.8 g) was added. Therefore, the charge composition slightly differs from the specified composition, it being at. %: 65-Zr; 20-Fe; 15-O.

Melt compositions, for which T_{liq}, T_{sol} and tie-line were measured, had been recommended by IRSN (Dr. M. Barrachin). The applied melting technology cannot ensure identity of the melt and charge compositions because a part of the refractory phase separates from the melt and crystallizes on the cold crucible surfaces. Therefore, a preliminarily evaluated amount of excessive zirconia was introduced into the charge.

3.3. Experimental procedures

The experimental procedures for T_{liq} determination were identical and included:

- Charge materials preparation and their thorough mixing in argon.
- Furnace loading with the specified composition and its blowing with argon.
- Molten pool production and its superheating .
- Measurements of molten pool depth and bottom crust thickness.
- Melt sampling.
- Lifting of the crucible with melt relative to the inductor for local cooling of the surface of the superheated molten pool, and videorecording of the process. Returning of the crucible to the initial position. Checking of reproducibility of the values of melt surface temperature and of the power removed from the crucible bottom and walls achieved before lifting of the crucible. Repetition of these operations several times.
- Heating termination. Pool surface videorecording.
- Ingot extraction from the crucible for the subsequent analysis.

It should be noted that a slightly different technique of melt surface cooling was used in CORD30. It's essence is in shifting the movable electromagnetic screen, as described in /14/.

Brief comments to the tests are given below.

CORD30

The first test with the Zr-Fe-O system was also the first one with a considerable amount of metal using the IMCC technology on the Rasplav facility.

Electrical characteristics of the high-frequency generator and history of the molten pool surface temperature throughout the test are given in Fig. 3.1.

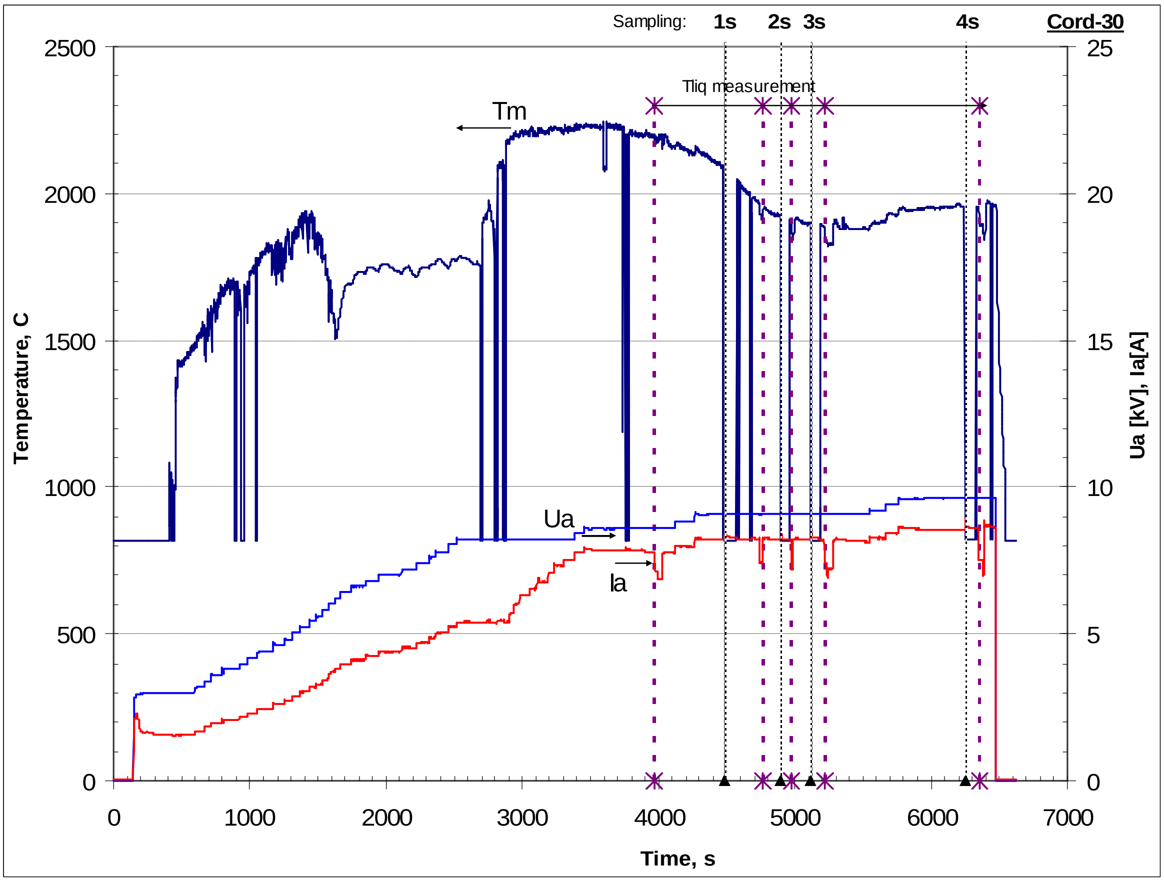

Fig. 3.1. History of the anode current (Ia), anode voltage (Ua) and pyrometer readings (Tm) in CORD30

During the test, T_{liq} was measured several times by applying the VPA IMCC method and the water-cooled screen. The temperature was observed to decrease from 2169 down to 1852°C (Fig. 3.2). Melt was sampled between these two measurements. The drop of the measured T_{liq} is explained by the reduced oxygen concentration in the melt due to crystallization of a ZrO_2-rich layer on the pool bottom. An increase of power in the melt did not lead to melting of the bottom crust.

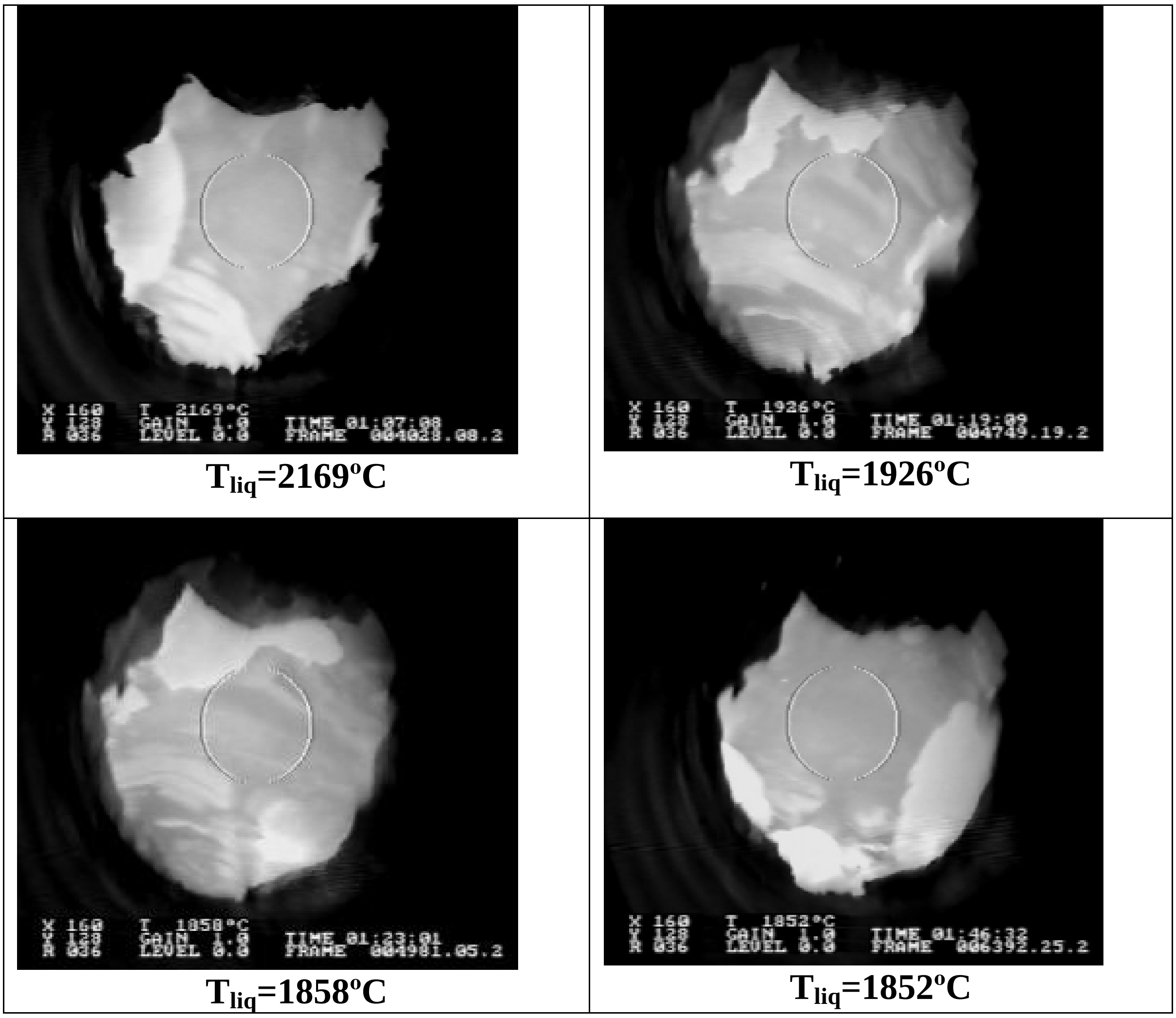

T_{liq}=2169°C

T_{liq}=1926°C

T_{liq}=1858°C

T_{liq}=1852°C

Fig. 3.2 Videoframes of the melt surface during T_{liq} measurements

In the end of the test, a stationary thermal condition was achieved in the 'melt – bottom crust' system. A thermogram of T_{liq} measurement for this condition is presented in Fig. 3.3.

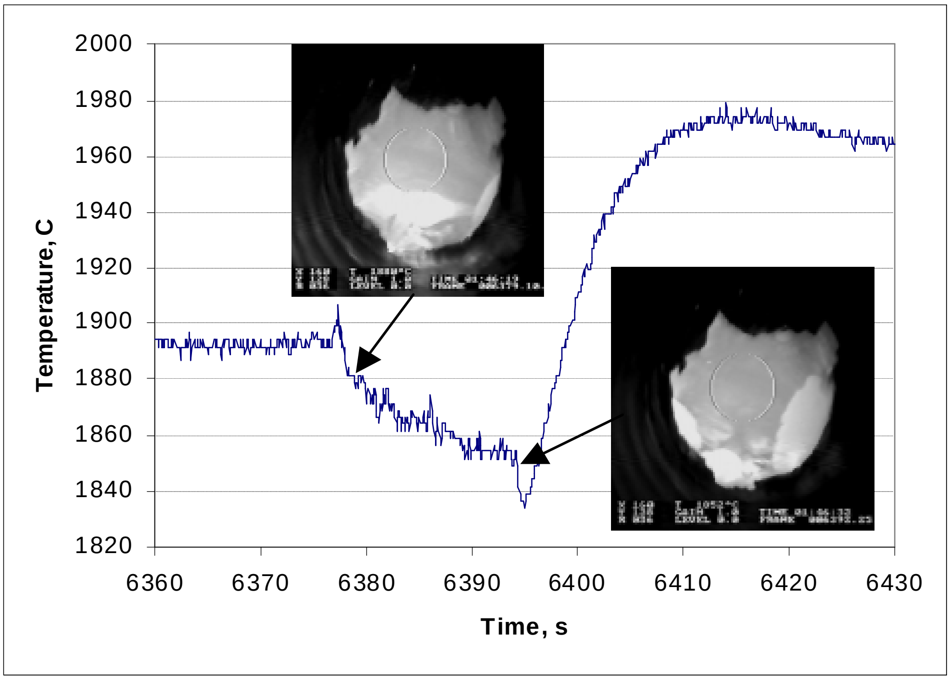

Fig. 3.3. Thermogram with the molten pool surface videoframes. T_{liq}=1852°C

CORD32

The induction system was optimized in order to increase efficiency of the furnace, and then it was decided to repeat the test, but melt ejection from the crucible occurred during molten pool formation and homogenization. The water-cooled pyrometer shaft got burned through and water emerged onto the molten pool surface. The test was aborted and performed again later.

CORD33

The previous test was repeated for measuring T_{liq} of the specified composition. Electrical characteristics of the high-frequency generator and history of the melt surface temperature throughout the test are given in Fig. 3.4. The melt was sampled three times and T_{liq} measured two times by VPA IMCC when lifting the crucible with melt relative to the inductor. It should be noted that the melt surface temperature dropped for about 80°C during the test. The bottom crust thickness was measured at 1450 s and found to be less than 1 mm. The temperature, from which the melt was cooled and crystallized, equaled 2420°C. No bottom crust measuring was performed before heating termination. When the ingot was cut and a thin section prepared, two layers differing in colour and texture were recorded for the macrostructure.

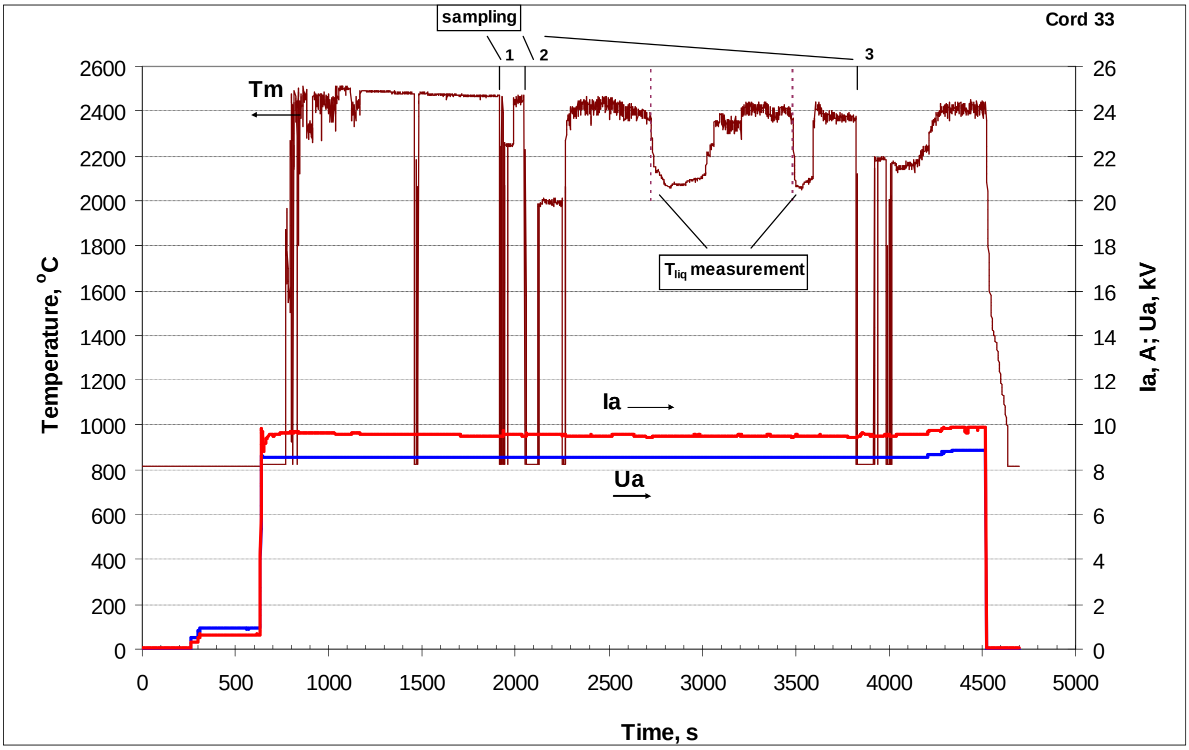

Fig. 3.4. History of the anode current (Ia), anode voltage (Ua) and pyrometer readings (Tm) in CORD33

CORD35

The present test was aimed at melt slow crystallization under the conditions close to equilibrium in the concentration domain of the miscibility gap. Electrical characteristics of the high-frequency generator and history of the melt surface temperature throughout the test are given in Fig. 3.5. Equilibrium crystallization was achieved by slow continous shifting the crucible with melt relative to the inductor at 10 mm/h. Besides, T_{liq} was measured during the test in order to check the measurements made in CORD33, and the melt was sampled three times. The third sample was taken in the end of the test before crystallization of the molten pool. At switching the HF heating off, T_{liq} of the molten pool was evaluated. The temperature, from which the melt was cooled, amounted to 2120°C.

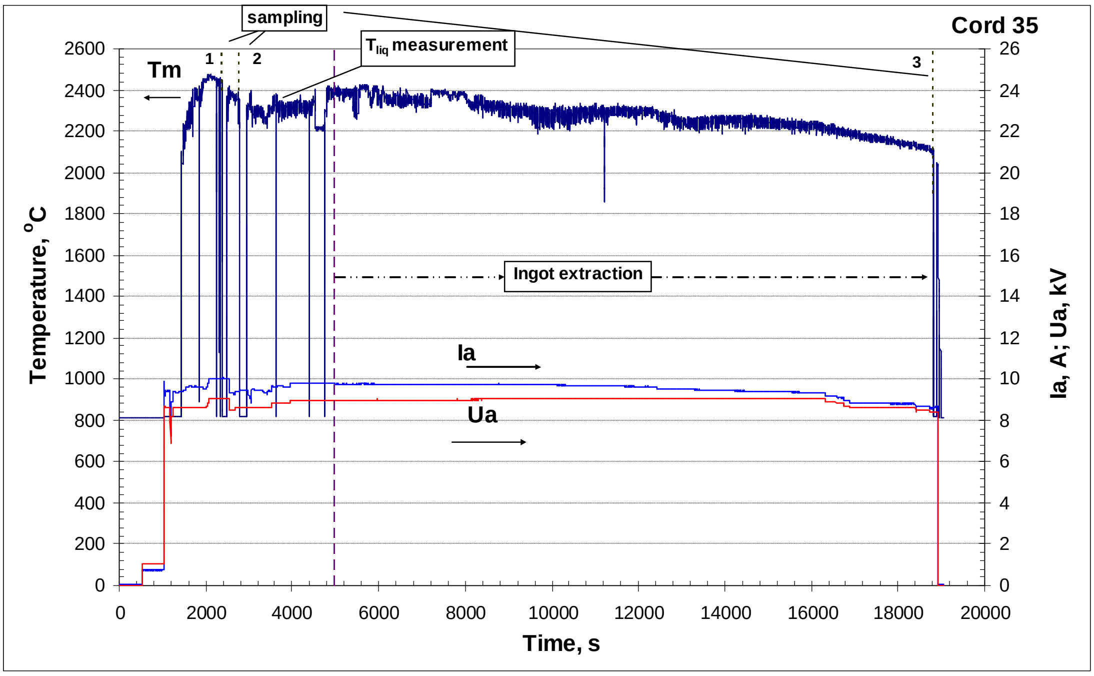

Fig. 3.5. History of the anode current (Ia), anode voltage (Ua) and pyrometer readings (Tm) in CORD35

CORD39

The experimental technique of CORD33 was used for the test, but the melt composition differed. Electrical characteristics of the high-frequency generator and history of the melt surface temperature throughout the test are given in Fig. 3.6. T_{liq} was measured three times and melt sampled two times during the test. The temperature, from which the melt was cooled, equaled 2520°C. As in CORD33, the analysis of an image of thin section from the ingot longitudinal section has shown melt stratification into two layers.

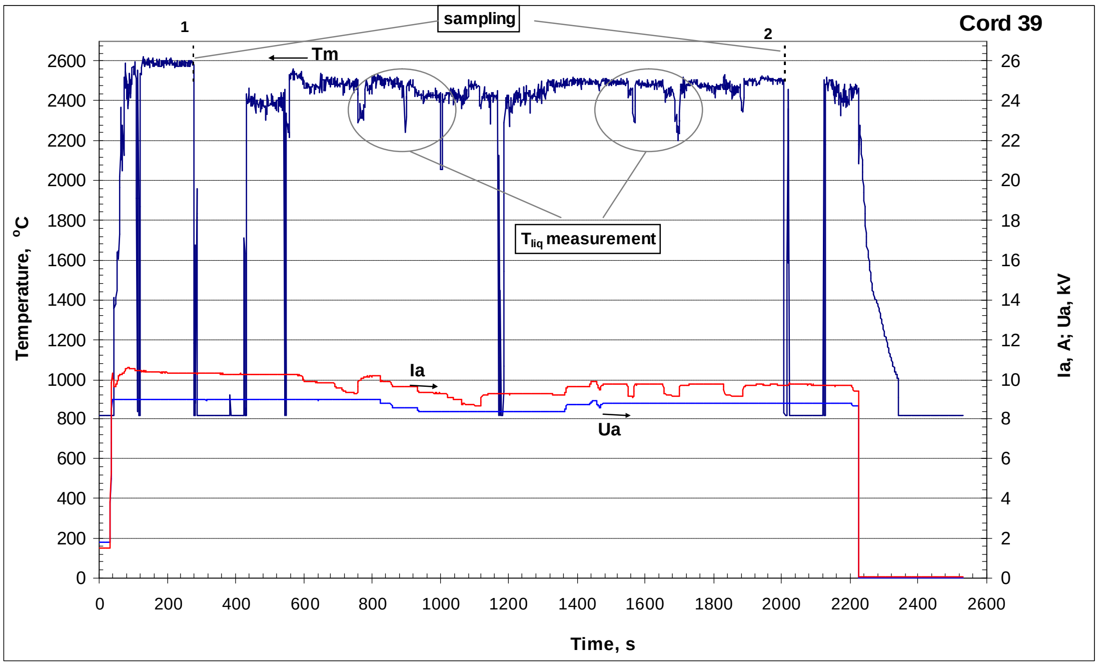

Fig. 3.6. History of the anode current (Ia), anode voltage (Ua) and pyrometer readings (Tm) in CORD39

CORD44

This test was aimed at determining T_{liq} and the possibility of stratification of the melt with the specified composition. Electrical characteristics of the high-frequency generator and history of the melt surface temperature throughout the test are given in Fig. 3.7. T_{liq} was measured three times and melt sampled two times during the test. The temperature, from which the melt was cooled, equaled 1820°C. The analysis of an image of thin section from the ingot longitudinal section has discovered no melt stratification.

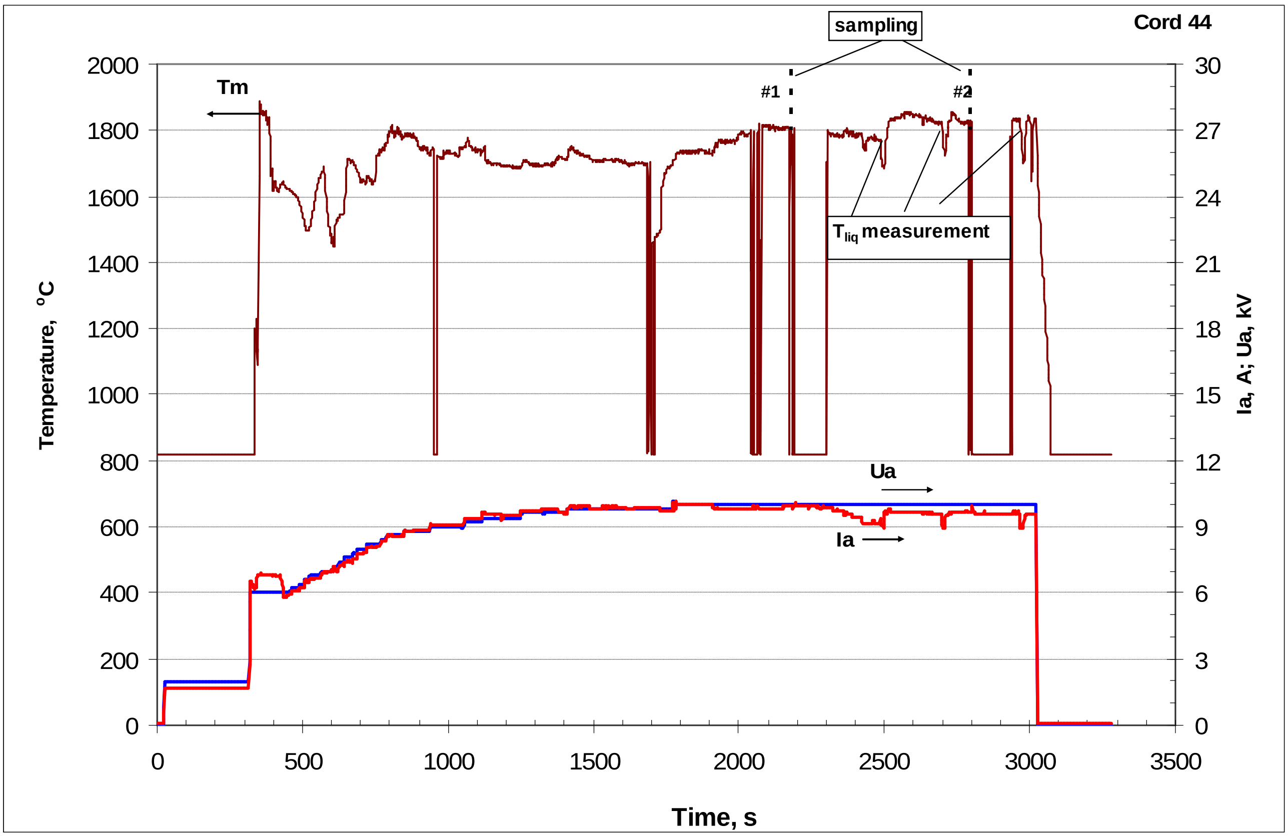

Fig. 3.7. History of the anode current (Ia), anode voltage (Ua) and pyrometer readings (Tm) in CORD44

CORD45

Similarly to CORD44, this test was aimed at determining T_{liq} of the specified composition and of the miscibility gap tie-line, i.e. of compositions of the coexisting liquids. Electrical characteristics of the high-frequency generator and history of the melt surface temperature throughout the test are given in Fig. 3.8. T_{liq} was measured twice and melt sampled two times during the test. The temperature, from which the melt was cooled, amounted to 2540°C. It should be noted that the pressure of iron vapours above the melt was high during the test, and it was the reason of abundant aerosols, which have increased the error of measuring the molten pool surface temperature by pyrometry and reduced the concentration of iron in the melt.

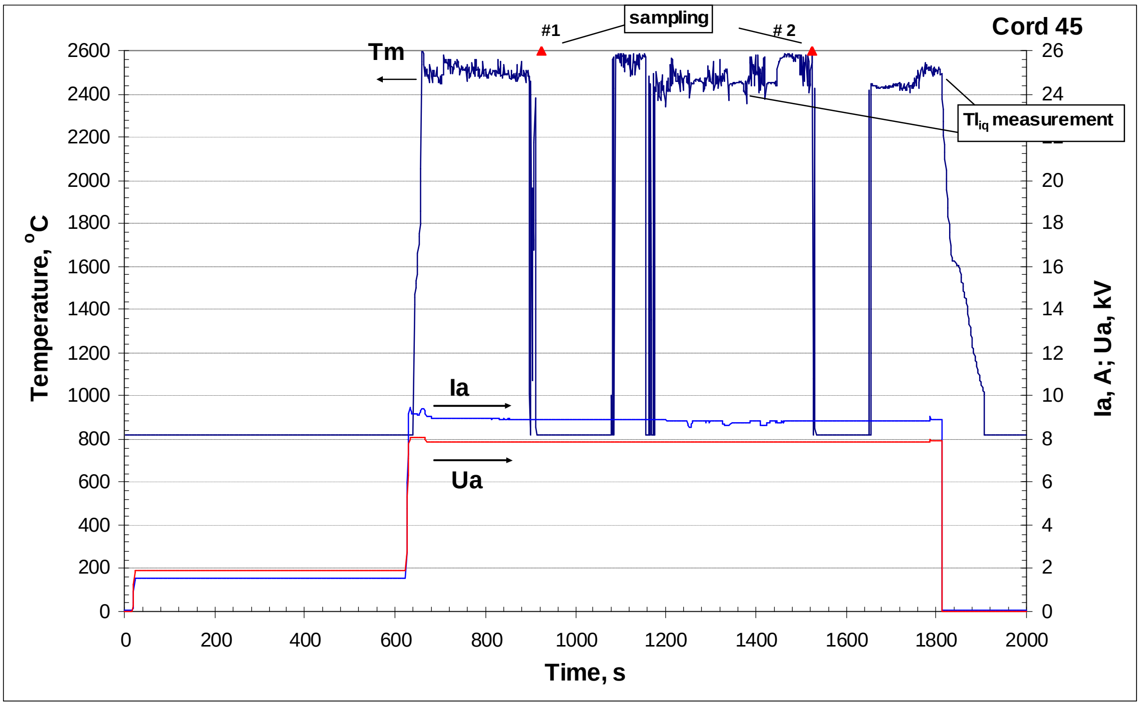

Fig. 3.8. History of the anode current (Ia), anode voltage (Ua) and pyrometer readings (Tm) in CORD45

3.4. Posttest analysis

Comprehensive physicochemical studies of the melt samples and ingots were carried out for determining compositions of the melt corresponding to the measured liquidus temperatures, compositions of the liquids coexisting in the miscibility gap and for studying the path of crystallization.

3.4.1. Ingots macrostructure

After the tests, the furnaces were disassembled, ingots extracted from crucibles and cut longitudinally. One half of the ingot was used for making a microsection for SEM/EDX analysis, and from the other one samples were taken for XRF, chemical analysis, and oxygen content determination by means of carbothermal reduction (CTR).

Fig. 3.9 presents images of longitudinal sections of the ingots from CORD33, 35, 39, 44, 45 showing locations where samples were taken for XRF, chemical analysis, CTR and bottle density determination.

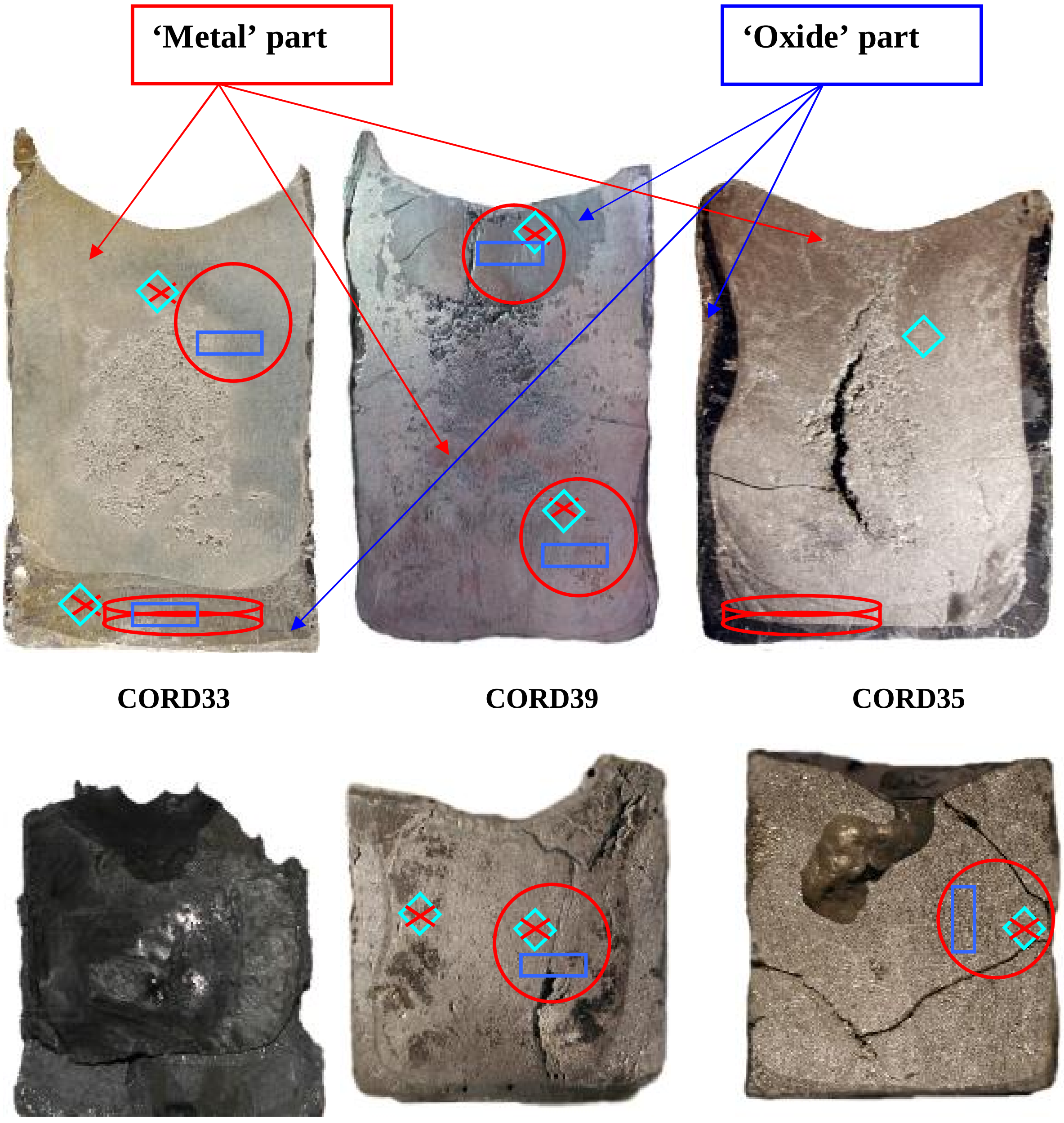

✕ - chemical analysis; ○ - XRF; ◇- bottle density determination;

▭ -CTR.

Fig. 3.9. Longitudinal sections of ingots from CORD30, 33, 35, 39,44,45 and locations of sampling

3.4.2. Material balances of the tests

In order to make up material balances of the tests, the initial charge components and fused products were weighed with accuracy up to 0.1 g.

Material balances of CORD30, 33, 35, 39, 44, 45 are given in Tab. 3.3.

Table 3.3. Material balances of CORD30, 33, 35, 39, 44, 45

CORD	Introduced into melt, g		Collected, g	
30 2)	**ZrO$_2$**	130.7	**Rod samples**	31.3
	Zr	204.9	**Corium from probe 3)**	6.5
	Fe	71.5	**Ingot 1)**	360.2
			Spillages	6.6
			Aerosols	0.1
	Σ	**407.1**	**Σ**	**404.7**
	Debalance	**2.4**		
33 2)	**ZrO$_2$**	130.6	**Ingot**	330.4
	Zr	204.9	**Rod samples**	53.3
	Fe	71.5	**Corium from probe 3)**	8.1
			Spillages	7.8
			Aerosols	1.9
	Σ	**407.0**	**Σ**	**401.5**
	Debalance	**5.5**		
35 2)	**ZrO$_2$**	130.6	**Ingot**	308.9
	Zr	205.0	**Rod samples**	53.0
	Fe	71.4	**Corium from probe 3)**	12.4
			Spillages	13.1
			Above-melt crust	5.3
			Aerosols 4)	7.8
	Σ	**407.0**	**Σ**	**400.5**
	Debalance	**6.5**		
39	**ZrO$_2$**	123.6	**Ingot**	325.7
	Zr	183.0	**Spillages**	8.9
	Fe	93.3	**Rod samples**	52.2
			Aerosols	4.9
			Above-melt crust	7.8
	Σ	**399.9**	**Σ**	**399.5**
	Debalance	**0.4**		
44	**Zr**	222.2	**Ingot**	282.8
	Fe	47.3	**Rod samples**	12.2
	ZrO$_2$	39.2	**Corium from probe 3)**	1.3
	ZrO$_2$ 5) (additional)	12.8	**Above-melt crust**	23.2
			Spillages	1.8
	Σ	**321.5**	**Σ**	**321.3**
	Debalance	**0.2**		
45	**Zr**	119.4	**Ingot**	300.9
	Fe	174.9	**Rod samples**	8.4
	ZrO$_2$	32.2	**Aerosols**	11.5
			Spillages	4.5
	Σ	**326.5**	**Σ**	**325.3**
	Debalance	**1.2**		

1) – ingot weighed together with crusts located above the melt surface (m=82 g);

2) – a larger quantity of ZrO$_2$ was introduced into the melt allowing for the amount used in crust formation;

3) – a tungsten probe was used for measuring molten pool depth and bottom crust thickness;

4) – the aerosol deposits on the crucible sections oxidized in air during disassembly of the furnace and changed their colour from dark-grey to orange; a part of them ignited spontaneously at opening the furnace;

5) – during melting a crust formed on the crucible sections and could not be broken off back into the melt. To melt the crust, ZrO$_2$ (m=12.8 g) was added into the crucible.

The given data indicate a significant amount of aerosols in the tests. This is connected with high temperature of melts and substantial evaporation of iron, as a consequence.

3.4.3. Densities of the oxidic and metallic parts of the corium ingot

In order to calculate masses of the oxidic and metallic parts of ingots from CORD33, 39 with the aim of making up the per-element mass balance, bottle densities were determined for the parts and the volumes were calculated from their areas in the longitudinal section (supposing axial symmetry). Masses (*m*) were calculated using the formula 3.1.

$$m = V \cdot r \qquad (3.1)$$

where V is the volume of the oxidic/metallic part, cm^3;

r is bottle density of the oxidic/metallic part, g/cm^3.

Bottle densities of the metallic and oxidic parts were determined according to the technique described in /15/. Locations of samples taking for analytical purposes are shown in Fig. 3.9. High-purity ethyl alcohol was used as the liquid for the bottle method. Tab. 3.4 summarizes the results of bottle density measuring for the metallic and oxidic parts of ingots from CORD 33, 39, and the calculated volumes.

Tab.3.4. Bottle densities measuring and the calculated volumes of the metallic and oxidic parts of ingots from CORD 33, 39

CORD	Oxidic part		Metallic part	
	Density, g/cm^3	Volume, cm^3	Density, g/cm^3	Volume, cm^3
33	6.9	15.4	6.5	34.5
39	5.6	5.2	6.4	46.3

The error of bottle density determination was ±2 %, and that of volume measurement was ± 3%.

3.4.4. Chemical analysis

The melt rod samples from CORD30, 33, 35, 39, 44 and 45, the samples prepared from ingots from CORD33, 39, 44, 45 and the above-melt crust from CORD44 were analyzed for the content of Fe and Zr.

The samples from CORD30 and 35 were dissolved in a mixture of concentrated orthophosphoric and sulphuric acids (1:2) in argon.

The method of total zirconium determination is based on the formation of a stained complex compound of zirconium (IV) with xylenol orange in a solution of sulphuric acid with the equivalent molar concentration of 0.3-0.4 mol./dm^3 /16-18/.

The method of total iron determination is based on the reaction of orthophenanthroline with ions of bivalent iron within the 3–9 pH range, followed formation of a complex compound with a orange-red colour. The colour develops fast at pH=3.0-3.5 in presence of excessive orthophenathroline and keeps stable within several days. The range of measured iron concentrations lies within 0.4–400 mg/dm^3. The total relative error does not exceed ±5% provided that the measured optical densities are within 0.2–0.6 range /19, 20/.

For the samples from CORD33, 39, 44, 45 a new analytical technique has been applied. The 0.1 - 0.5 g samples chosen from the ingot were fused with (3.0±0.5) g of potassium pyrosulfate at (900±25)ºC until obtaining a transparent fusion cake, which was later dissolved in 200 – 250 ml 1M solution of sulphuric acid. Then the determination of total zirconium (Zr^{4+}) was done by photocolorimetry with xylenol orange /16-18/ and of Fe_{total} – by photocolorimetry with orthophenanthroline /19, 20/.

Chemical analysis permitted determination of zirconium and iron in a sample, and oxygen was calculated from residue. In order to increase precision of chemical analysis, oxygen concentration was determined in the same samples by means of carbothermal reduction (see Tab. 3.64), and the data from Zr and Fe determination were renormalized using the new data for oxygen.

In order to destroy the intermetallic compounds possibly influencing the results of chemical analysis, the samples taken from ingots from CORD33, 44 and 45 were oxidized. The samples were oxidized within 4 hours by heating up to 1100ºC in air and crushed in the vibrating mill down to particles sized <50 μm. Then the elemental analysis of the oxidized samples was done using the techniques described above. The obtained results were also renormalized taking the oxygen determined by CTR into account.

Tab. 3.5 presents the results of chemical analysis of the fused products from CORD30, 33, 35, 39, 44 and 45, renormalized taking into account the oxygen determined by CTR.

Table 3.5. Results of chemical analysis for CORD30, 33, 35, 39, 44, 45

CORD	**Sample**	**Content, mass%**			**Content, at.%**		
		Zr	**Fe**	**O**[1)]	**Zr**	**Fe**	**O**
30	Rod sample No.1	74.6	22.7	2.68	58.7	29.2	12.0
	Rod sample No.2	73.9	24.2	1.89	59.5	31.9	8.7
	Rod sample No.3	71.1	27.4	1.57	57.0	35.8	7.2
	Rod sample No.4	74.0	24.2	1.76	59.9	32.0	8.1
33	Rod sample No.2	74.7	19.6	5.7	53.7	23.0	23.3
	Rod sample No.3	75.8	18.5	5.7	54.7	21.8	23.5
	Ingot (metal-rich part, oxidized)	78.3	17.0	4.7	58.9	20.9	20.2
	Ingot (metal-rich part, oxidized)	66.7	13.8	19.5	33.3	11.2	55.5
	Ingot (metal-rich part) (*with correction for oxygen)*	79.0	16.3	4.7	59.6	20.1	20.2
	Ingot (oxide-rich part)	78.5	7.3	14.2	45.8	6.9	47.2
35	Rod sample No.2	73.6	20.8	5.6	52.8	24.3	22.9
	Rod sample No.3	76.6	20.7	2.72	60.8	26.8	12.3
39	Rod sample No.1	67.9	25.9	6.20	46.7	29.0	24.3
	Rod sample No.2	68.4	25.2	6.40	46.8	28.2	25.0
	Ingot (oxide-rich part)	79.7	5.4	14.90	45.9	5.1	49.0
	Ingot (metal-rich part, oxidized)	70.9	22.7	6.40	49.1	25.7	25.3
44	Rod sample No.1	79.1	20.3	0.63	68.2	28.6	3.1
	Rod sample No.2	79.1	20.2	0.63	68.3	28.6	3.1
	Ingot – central area	81.7	17.3	1.03	70.5	24.4	5.1
	Ingot – central area (metal-rich part, oxidized)	69.0	12.8	18.2[2)]	35.6	10.8	53.6

	Ingot – central area (metal-rich part, oxidized) (*with correction for oxygen)*	83.5	15.5	1.03	72.8	22.1	5.1
	Ingot – lateral side	69.6	9.4	21.05	33.9	7.5	58.6
	Above-melt crust	67.5	11.4	21.05	32.8	9.0	58.2
45	Rod sample No.1	43.4	54.6	1.94	30.2	62.1	7.7
	Rod sample No.2	43.1	55.0	1.98	29.9	62.3	7.8
	Ingot	44.6	53.6	1.76	31.4	61.6	7.1
	Ingot (metal-rich part, oxidized)	32.4	38.8	28.8 2)	12.5	24.4	63.2
	Ingot (metal-rich part, oxidized) (*with correction for oxygen)*	44.7	53.5	1.76	31.4	61.5	7.1

1) – oxygen was specified according to CTR results (Tab. 3.64) and the data on the main elements were normalized;
2) – oxygen determined from residue.

It has been mentioned already that in CORD30 the temperature of the melt dropped, the most refractory phase crystallized on the bottom and due to this the melt was getting depleted in ZrO_2, while the content of Fe was increasing, accordingly. This is confirmed by the results of analysis of melt samples, which demonstrate the decreasing oxygen and increasing iron contents from the first sample to the third one. Before the 4th melt sampling the temperature has increased insignificantly (see Fig. 3.1) and a part of the refractory phase has obviously melted. As a results, the content of Zr in the rod sample has increased, while that of Fe decreased (Tab. 3.5). Notable is the coincidence (within the error of method) of the composition of samples No.2 from CORD33 and No.2 from CORD35, as it indicates reproducibility of results related to the stratification area. In CORD35, like in CORD30, the content of Fe increased and that of oxygen decreased after the primary crystallization phases had crystallized (sample No.3 CORD35, Tab. 3.3)

A sample was prepared from the crystallized layer of the primary crystallization phase from CORD35 and according to the volumetric analysis the content of free Zr was found to equal 4.2 mass %.

For some tests, elemental material balances have been made up (see Tabs.3.6–3.9.)

Tab. 3.6 offers the elemental material balance for CORD33 taking into account the data from Tab. 3.5.

Table 3.6. Elemental material balance for CORD33 according to chemical analysis

Element	Introduced, g 1)	Mass of the ingot oxidic part, g 2)	Mass of the ingot metallic part, g 2)	Collected, g				Δ, g
				Samples 3), g	Oxidic part, g	Metallic part, g	Total, g	
Zr	291.74	106	224	46.07	83.56	176.86	306.49	+14.75
Fe	70.02			11.83	7.75	36.59	56.17	-13.85
O	30.04			3.50	15.11	10.53	29.14	-0.90

1) – introduced into the melt, the spillages (m=7.8 g), debalance (m=5.5 g) and aerosols (m=1.9 g) excluded;
2) – masses of the oxidic and metallic parts were calculated on the basis of their densities and volumes (Tab. 3.4);.
3) – the mass of sample No.1 - 17.8 g, of rod sample No.2 - 17.3 g; of rod sample No.3 - 18.2 g, of sample from the probe - 8.1 g.

It is seen from Tab.3.6. that the debalance for the main elements is ~ 15 g. The SEM/EDX analysis of the ingot oxidic part has shown it to be inhomogeneous (Fig. 3.25, Region 1-1-1). As the oxidic part analysis did not use the average sample, the error was obviously the greatest and it explains such a significant debalance.

Tab.3.7 offers the elemental material balance for CORD39 taking into account the data of chemical analysis.

Table 3.7. Elemental material balance for CORD39 according to chemical analysis

Element	Introduced, g 1)	Mass of the ingot oxidic part 2), g/ density, g/cm^3	Mass of the ingot metallic part 2), g/ density, g/cm^3	Collected, g				Δ, g
				Samples 3), g)	Oxidic part, g 4)	Metallic part, g	Total, g	
Zr	267.62	<u>36</u> 5.6	<u>297</u> 6.4	35.53	29.05	210.63	275.21	+7.59
Fe	89.49			13.40	1.98	67.39	82.77	-6.72
O	28.59			3.27	5.43	19.01	27.71	-0.88

1) – introduced into the melt, the spillages (m=8.9 g), debalance (m=0.4 g) and aerosols (m=4.9 g) excluded;

2) – masses of the oxidic and metallic parts were calculated on the basis of their densities and volumes (Tab. 3.4);

3) – the mass of sample No.1 - 36.3 g, of sample No.2 - 15.9 g;

4) – includes the above-melt crust, the mass of which is 7.8 g.

Apparently, the debalance of elements is due to the fact that the above-melt crust was not analyzed and its mass summed with that of the ingot oxidic part.

The error of Zr determination by photocolorimetry was less than 3 relative % and that for Fe – less than 5 relative %.

3.4.5. X-ray fluorescence (XRF) analysis

The elemental composition of the samples was determined by the XRF method using the SPECTROSCAN MAX-GV /23/.

All samples were crushed into 100 µm particles, quartered and further ground into particles not exceeding 50 µm, and then the powder was compacted into pellets for the analysis. Also, samples representing flat, ground plates ~ 10×15 mm^2 were cut from the characteristic zones for analysis. All the works on both rod and ingot samples preparation were performed in argon.

Quantitative analysis of samples from the oxidic parts of ingots, rod samples and aerosols from CORD 33, 35, 39, 44 and 45 employed the method of fundamental parameters (MFP) /13/. The samples taken from the metal-rich parts of ingots from CORD 33, 39, 44 and 45 were first oxidized within 4 hours by heating up to 1100ºC in air and then analyzed by spectrometer using stoichiometric oxidic calibration specimens.

Tab.3.10 contains the results of analysis of corium samples from CORD30, 33, 35, 39, 44, 45.

Table 3.10. XRF data for samples from CORD30, 33, 35, 39, 44, 45

CORD	Sample	Content, mass %			Content, at.%		
		Zr	Fe	O1)	Zr	Fe	O
30	Rod sample No.1	71.7	25.6	2.68	55.7	32.5	11.9
	Rod sample No.2	71.0	27.1	1.89	56.3	35.1	8.5
	Rod sample No.3	69.2	29.2	1.57	55.0	37.9	7.1
	Rod sample No.4	71.6	26.6	1.76	57.3	34.7	8.0
33	Rod sample No.2	73.2	21.1	5.7	52.2	24.6	23.2
	Rod sample No.3	74.1	20.2	5.7	53.1	23.6	23.3
	Ingot (metal-rich part, oxidized)	64.9	13.2	21.9 2)	30.7	10.2	59.1
	Ingot (top part, oxidized) (*with correction for oxygen)*	79.2	16.1	4.7	59.9	19.9	20.3
	Ingot (oxide-rich part)	80.7	5.1	14.2	47.5	4.9	47.6
35	Rod sample No.2	73.8	20.6	5.60	53.0	24.1	22.9
	Rod sample No.3	75.1	22.2	2.72	59.2	28.5	12.2
	Ingot (oxidic layer)	73.8	0.3	25.9	33.2	0.2	66.6
39	Rod sample No.1	65.7	28.1	6.20	44.7	31.3	24.1
	Rod sample No.2	68.3	25.3	6.40	46.7	28.3	25.0
	Ingot (top part)	77.5	7.6	14.90	44.3	7.1	48.6
	Ingot (oxide-rich part, oxidized)	60.6	18.8	20.6 2)	29.0	14.7	56.3
	Ingot (metal-rich part, oxidized)	71.4	22.2	6.40	49.6	25.1	25.3
44	Rod sample No.1	78.6	20.8	0.63	67.7	29.3	3.1
	Rod sample No.2	78.0	21.4	0.63	66.9	30.0	3.1
	Above-melt crust	69.9	9.1	21.05	34.1	7.2	58.6
	Ingot – center (metal-rich part, oxidized)	66.4	9.8	23.8 2)	30.4	7.3	62.2
	Ingot – center (metal-rich part, oxidized) (*with correction for oxygen)*	86.2	12.7	1.03	76.4	18.4	5.2
45	Rod sample No.1	39.8	58.2	1.94	27.3	65.1	7.6
	Rod sample No.2	39.8	58.2	1.98	27.2	65.0	7.7
	Ingot (metal-rich part, oxidized)	33.8	43.1	23.1 2)	14.3	29.8	55.8
	Ingot (metal-rich part, oxidized) (*with correction for oxygen)*	43.2	55.1	1.76	30.2	62.8	7.0
	Aerosols	20.2	71.5	8.22	11.0	63.5	25.5

1) – oxygen was specified according to CTR results (Tab. 3.64) and the data on the main elements were normalized;

2) – oxygen determined from residue.

Both chemical analysis and XRF of rod samples from CORD30 have shown a decreased content of Zr and increased of Fe in the samples.

Tab. 3.11 contains the elemental material balance for CORD33 taking into account the XRF data.

Table 3.11. Elemental material balance for CORD33 based on the XRF data

Element	Introduced, g [1]	Mass of the ingot oxidic part[2], g/ density, g/cm^3	Mass of the ingot metallic part[2], g/ density, g/cm^3	Collected, g				Δ, g
				Samples[3], g	Oxidic part, g	Metallic part, g	Total, g	
Zr	291.74	106 6.9	224 6.5	45.12	85.89	177.38	308.39	+16.65
Fe	70.02			12.78	5.41	36.08	54.27	-15.75
O	30.04			3.50	15.11	10.53	29.14	-0.90

[1] – introduced into the melt, the spillages (m=7.8 g), debalance (m=5.5 g) and aerosols (m=1.9 g) excluded;

[2] – masses of the oxidic and metallic parts were calculated on the basis of their densities and volumes (Tab. 3.4);

[3] – the mass of rod sample No.1 - 17.3 g, of rod sample No.2 - 18.2 g; of a sample (taken by spoon) – 17.8 g.

It is obvious from Tab.3.11 that debalance for the main elements is ~ 17 g (compare with ~ 15 g in Tab. 3.6). This is obviously determined by inhomogeneity of the ingot oxidic part and a greater error in calculations of its composition.

Tab.3.12 contains the elemental material balance for CORD39 taking into account the XRF data.

Table 3.12. Elemental material balance for CORD39 based on the XRF data

Element	Introduced, g [1]	Mass of the ingot oxidic part[2], g/ density, g/cm^3	Mass of the ingot metallic part[2], g/ density, g/cm^3	Collected, g				Δ, g
				Samples[3], g	Oxidic part, g [4]	Metallic part, g	Total, g	
Zr	267.62	36 5.6	297 6.4	34.69	28.26	212.19	275.14	+7.52
Fe	89.49			14.24	2.77	65.83	82.84	-6.65
O	28.59			3.27	5.43	19.01	27.71	-0.88

[1] – introduced into the melt, the spillages (m=8.9 g), debalance (m=0.4 g) and aerosols (m=4.9 g) excluded;

[2] – masses of the oxidic and metallic parts were calculated on the basis of their densities and volumes (Tab.3.4).

[3] – the mass of sample No.1 - 36.3 g, of sample No.2 - 15.9 g;

[4] – includes the above-melt crust, the mass of which is 7.8 g.

It is seen from Tab. 3.12 that debalance for the main elements is ~ 7.5 g.

The error of Zr and Fe content determination by XRF was less than 5 relative %.

3.4.6. SEM/EDX analysis

Microstructure and elemental composition of the samples were studied by means of scanning electron microscopy (SEM) and energy dispersive X-ray spectrometry (EDX).

The SEM study employed the ABT-55 scanning electron microscope, and the OxfordLink microprobe attachment was used for the elemental analysis of the samples' regions marked for examination.

The spectral characteristic was taken for each sample for determining its integral composition and that for each separate phase. The quantitative analysis was made by comparing spectral intensity of the reference (superpure, specially prepared substances) and studied samples. The used references of U, Zr, Cr, Fe, Si, Ca, Ni were a part of the Link microprobe attachment set.

The threshold of reliable element identification depends on its sequential number in the Mendeleyev's periodic table and varies from 0.3 to 0.5 mass %. Detection of smaller quantities of elements is unreliable.

The EDX analyzer of the ABT-55 microscope is insensitive to light elements (to oxygen, for instance), therefore the quantity of oxygen was determined with this instrument from the mass deficiency and the error was ~5 mass %.

After the tests, the ingots were cut along the axis, and polished sections were produced from the halves or quarters. Melt samples represented 0.5 – 1.0 mm-thick crystalline flakes quenched on the rod cold surface. Thin sections were prepared from them, too. Then thin sections were examined by SEM and the coexisting phases analyzed.

CORD30

Though objectives of the test had not been achieved, the samples of melt and corium ingot were subjected to SEM/EDX. It was mentioned above that a ZrO_2-rich layer crystallized on the pool bottom during the test. As sampling was done at different time, the samples are characterized by different temperature conditions (Fig. 3.1) of molten pool liquid part. Templates were made from the melt samples and analyzed.

Noteworthy is that the samples differ microstructurally. For instance, round inclusions of the ZrO_2 phase were found in the 1st, most refractory(2169°C) sample (Fig. 3.10, Tab. 3.15, Points P4, P4a). In the 2nd and 3rd samples (1950, 1852°C), the primary crystallization phase ZrO_{2-x} in the form of dendrites is evenly spread across the whole surface of thin section (a darker phase) (Figs. 3.11, 3.12 and Tab. 3.16, Point P3). The further cooling causes crystallization of the Zr_6Fe_3O-based phase (Figs. 3.11, 3.12 and Tab. 3.16, Points P1 and P2). The 4th sample (1950°C) is inhomogeneous in terms of microstructure and composition (Fig. 3.13, Tab.3.18, SQ1 and SQ2).

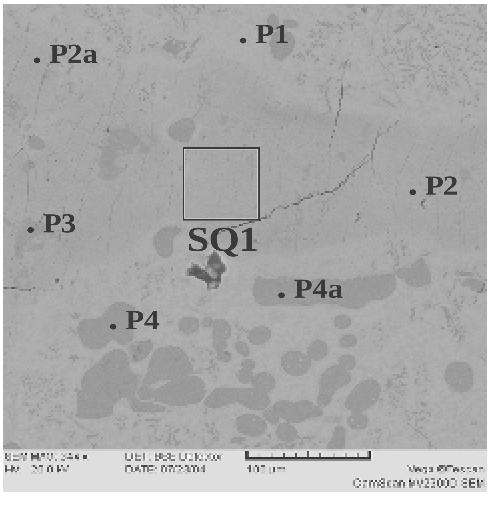

Fig. 3.10. Micrograph of sample No.1 from CORD30

Table 3.15. EDX data for sample No.1

No.		Zr	Fe	O
SQ1	mass %	70.45	21.59	7.96
	mol.%	46.62	23.33	30.04
P1	mass %	74.07	22.35	3.59
	mol.%	56.53	27.86	15.60
P2	mass %	72.13	14.77	13.10
	mol.%	42.19	14.12	43.69
P2a	mass %	69.93	15.09	14.97
	mol.%	38.86	13.7	47.44
P3	mass %	59.13	23.68	17.19
	mol.%	30.20	19.75	50.06
P4	mass %	77.23	-	22.77
	mol.%	37.30	-	62.70
P4a	mass %	76.56	0.84	22.59
	mol.%	37.03	0.67	62.3

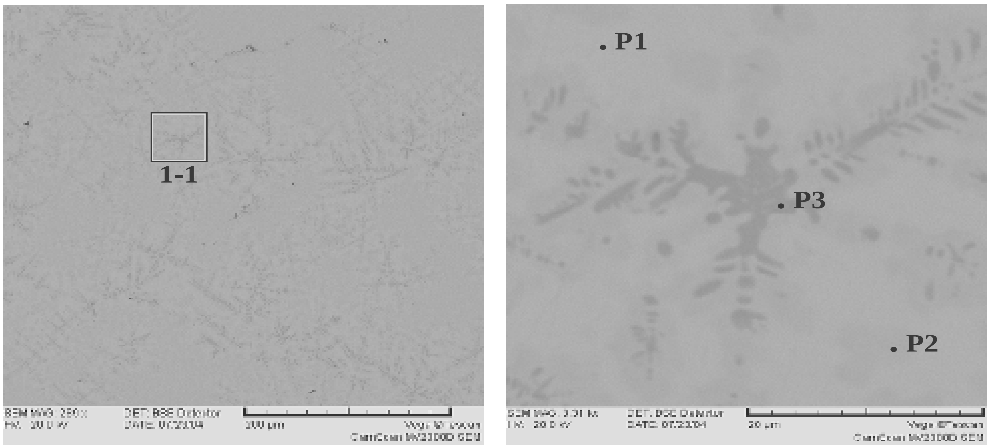

1 (SQ1) 1-1

Fig. 3.11. Micrographs of sample No.2 from CORD30

Table 3.16. EDX data for sample No.2

No.		Zr	Fe	O
SQ1	mass %	70.91	23.9	5.19
	mol.%	50.82	27.98	21.2
P1	mass %	70.93	23	6.07
	mol.%	49.57	26.26	24.18
P2	mass %	70.21	25.53	4.26
	mol.%	51.54	30.61	17.85
P3	mass %	72.58	4.86	22.56
	mol.%	34.71	3.8	61.49

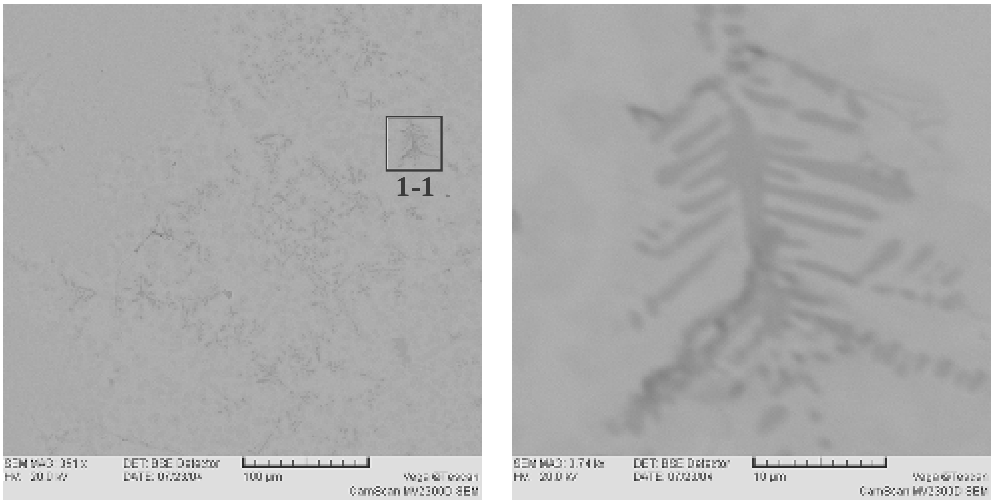

1 (SQ1) 1-1

Fig. 3.12. Micrographs of sample No.3 from CORD30

Table 3.17. EDX data for sample No.3

No.		Zr	Fe	O
SQ1	mass %	70.69	24.26	5.04
	mol.%	50.83	28.49	20.68

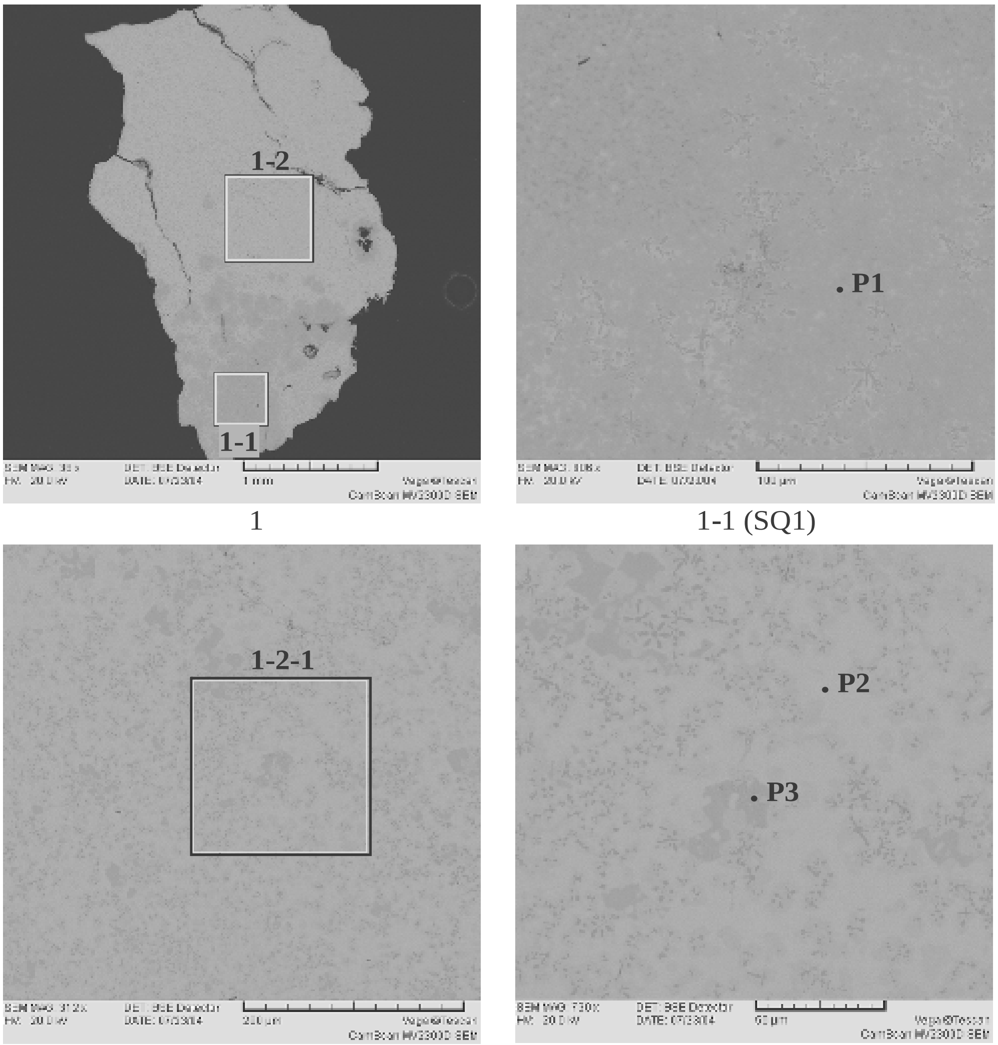

1 1-1 (SQ1)

1-2 (SQ2) 1-2-1

Fig. 3.13. Micrographs of sample No.4 from CORD30

Table 3.18. EDX data for sample No.4

No.		Zr	Fe	O
SQ1	mass %	71.68	23.22	5.1
	mol.%	51.69	27.35	20.96
SQ2	mass %	46.75	50.02	3.23
	mol.%	31.84	55.63	12.53
P1	mass %	75.83	21.17	3.0
	mol.%	59.46	27.11	13.43
P2	mass %	51.54	46.13	2.33
	mol.%	36.77	53.76	9.48
P3	mass %	45.69	52.28	2.04
	mol.%	32.02	59.84	8.14

After crystallization from 1970°C, the ingot was cut along the axis and a template was produced from it. The ingot consists of two parts separated by a crack. The top part represents the result of molten pool crystallization after switching off the heating. Most likely, the lower part was solid at when the heating was terminated. Microstructurally, the top part of the ingot shows the dendritic character of crystallization across the whole surface of thin section (Figs. 3.15, 3.16, 3.19). The analysis of its microstructure suggests the existence of three main phases, namely Zr_6Fe_3O, $ZrFe_2(O)$ and ZrO_2 (Fig. 3.15, Tab. 3.19, Points P1, P2, P3). It should be noted that the two latter phases are hard to distinguish by contrast of the phases.

Microstructure of the bottom part is more complex, it being the result of the long-term phases annealing after their crystallization on the pool bottom. The matrix phase is ZrO_2 (Fig. 3.17, Tab. 3.22, Point P4), from which the phases Zr_6Fe_3O and $ZrFe_2(O)$ have crystallized (Fig. 3.17, Tab. 3.21, Points P1 and P3).

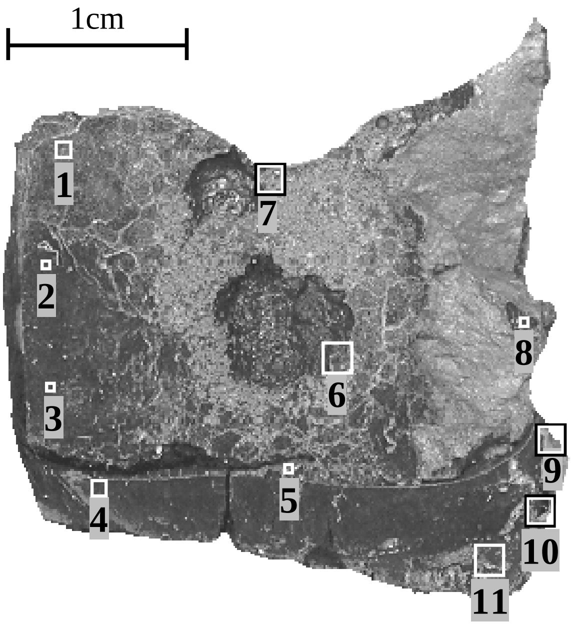

Fig. 3.14. Axial section of the ingot from CORD30 (1970°C) with regions marked for SEM/EDX analysis

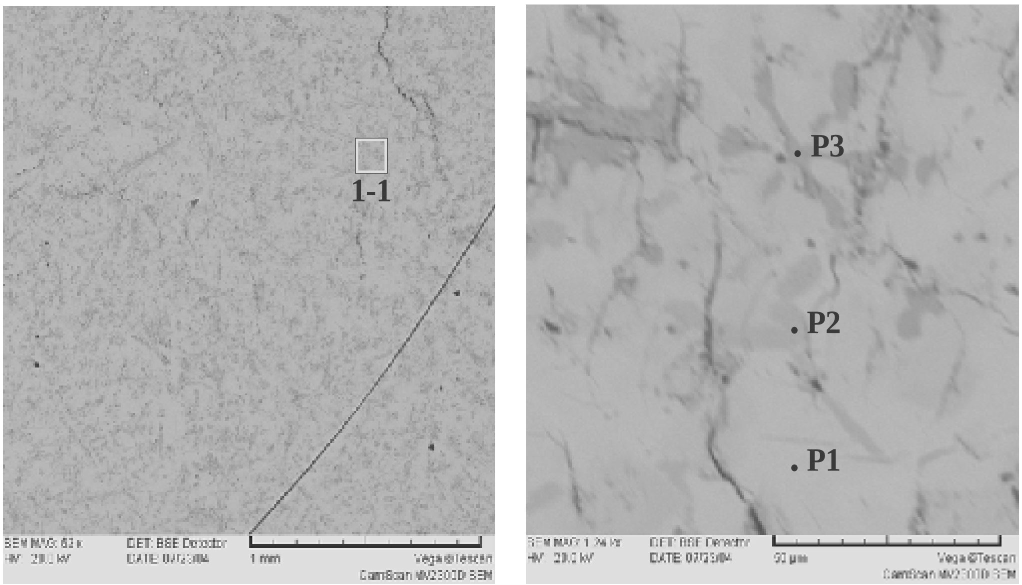

1 (SQ1) 1-1

Fig. 3.15. Micrographs of region 1 in the top part of the ingot from CORD30

Table 3.19. EDX data for region 1

No.		Zr	Fe	O
SQ1	mass %	70.26	22.78	6.96
	mol.%	47.75	25.29	26.96
P1	mass %	74.16	21.88	3.96
	mol.%	55.98	26.97	17.05
P2	mass %	46.04	48.5	5.46
	mol.%	29.44	50.65	19.91
P3	mass %	74.08	0.61	25.31
	mol.%	33.77	0.45	65.78

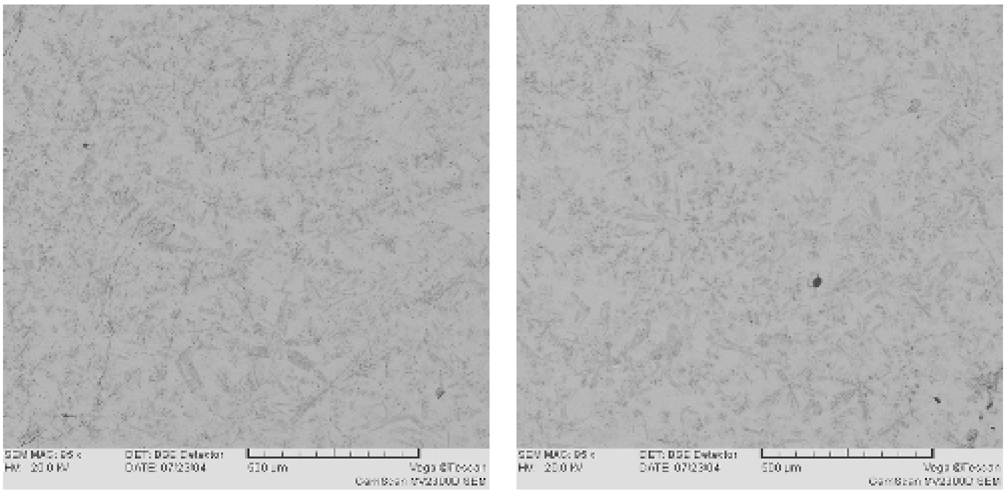

2 (SQ1) 3 (SQ2)

Fig. 3.16. Micrographs of regions 2 and 3 in the top part of the ingot from CORD30

Table 3.20. EDX data for regions 2 and 3

No.		Zr	Fe	O
SQ1	mass %	69.61	22.92	7.48
	mol.%	46.50	25.01	28.49
SQ2	mass %	69.94	22.85	7.22
	mol.%	47.13	25.14	27.73

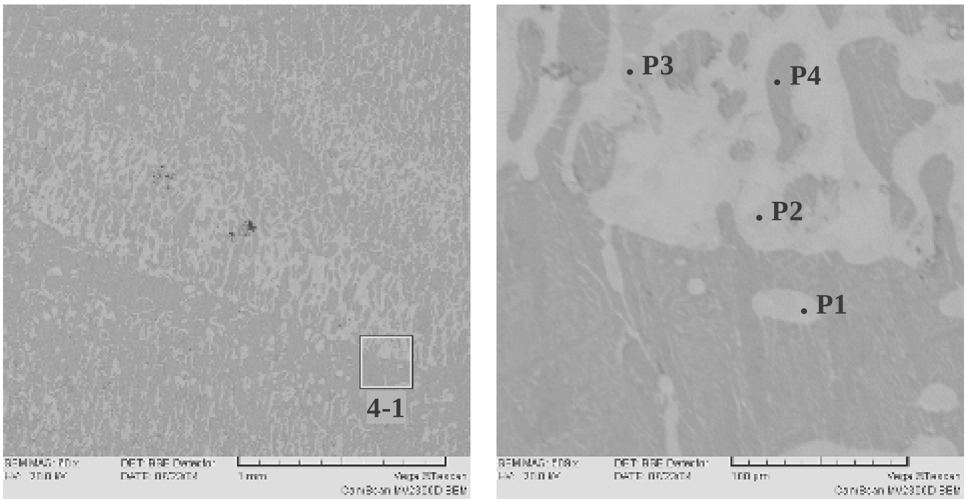

4 (SQ1) 4-1

Fig. 3.17. Micrographs of region 4 in the bottom part of the ingot from CORD30

Table 3.21. EDX data for region 4

No.		Zr	Fe	O
SQ1	mass %	74.44	7.08	18.47
	mol.%	38.91	6.05	55.05
P1	mass %	75.8	20.54	3.66
	mol.%	58.2	25.76	16.04
P2	mass %	61.52	33.59	4.88
	mol.%	42.65	38.04	19.31
P3	mass %	45.76	51.33	2.91
	mol.%	31.30	57.35	11.35
P4	mass %	74.55	-	25.45
	mol.%	33.94	-	66.06

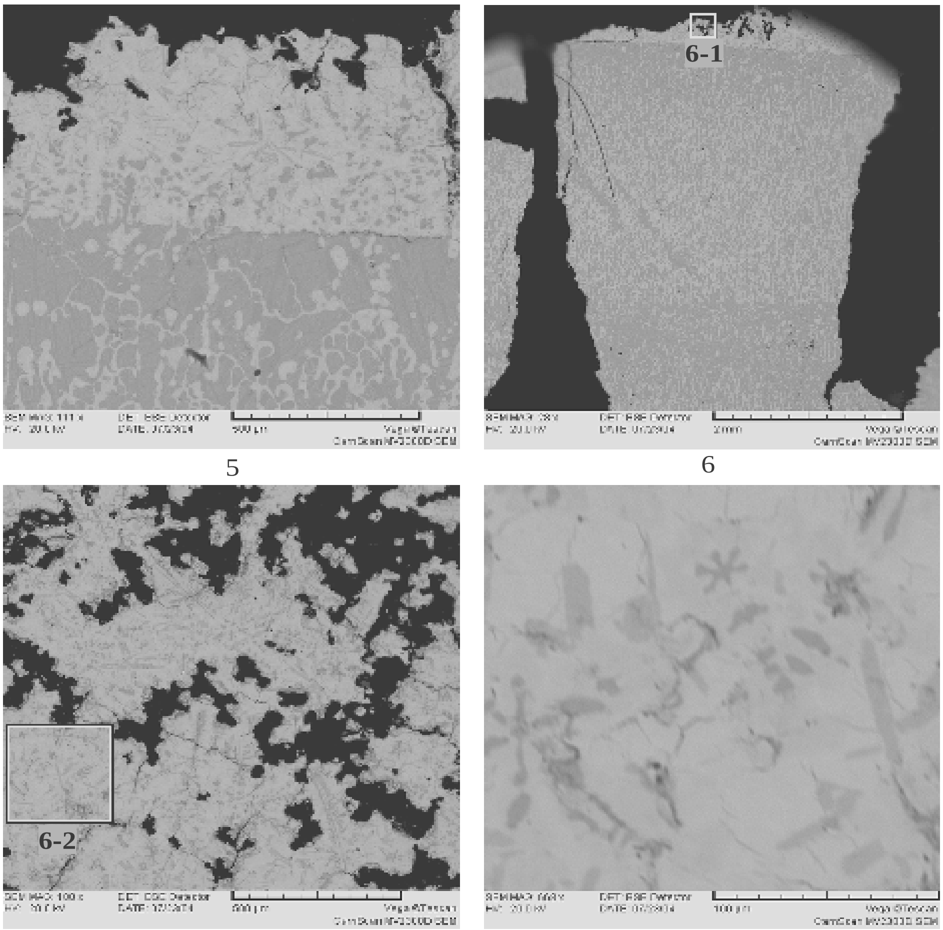

5 6

6-1 6-2 (SQ1)

Fig. 3.18. Micrographs of regions 5 (boundary) and 6 in the top layer of the ingot from CORD30

Table 3.22. EDX data for region 6

No.		**Zr**	**Fe**	**O**
SQ1	mass %	70.69	22.25	7.06
	mol.%	47.99	24.67	27.34

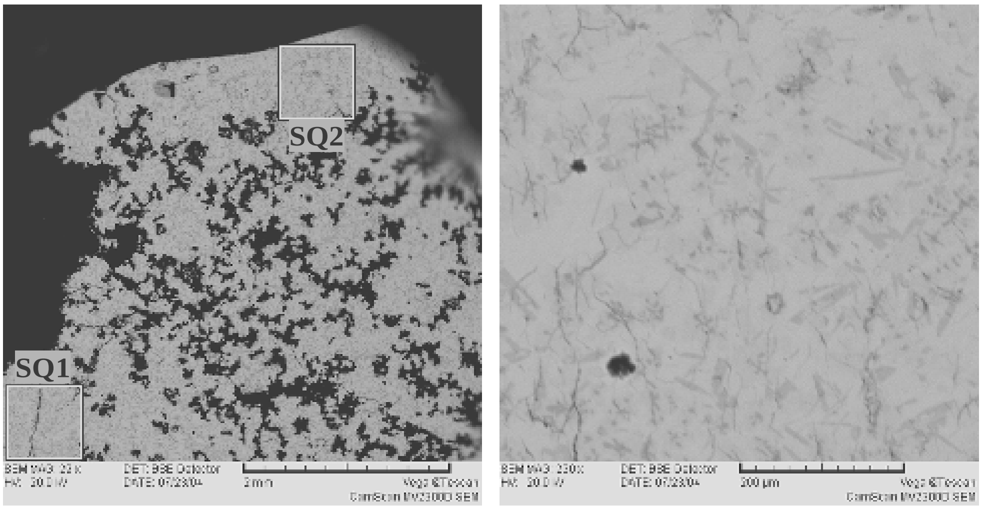

7 8 (SQ3)

Fig. 3.19. Micrographs of regions 7 and 8 in the top layer of the ingot from CORD30

Table 3.23. EDX data for regions 7 and 8

No.		Zr	Fe	O
SQ1	mass %	70.86	20.65	8.49
	mol.%	46.32	22.05	31.64
SQ2	mass %	69.87	24.51	5.62
	mol.%	49.22	28.21	22.57
SQ3	mass %	71.36	22.81	5.84
	mol.%	50.29	26.25	23.46

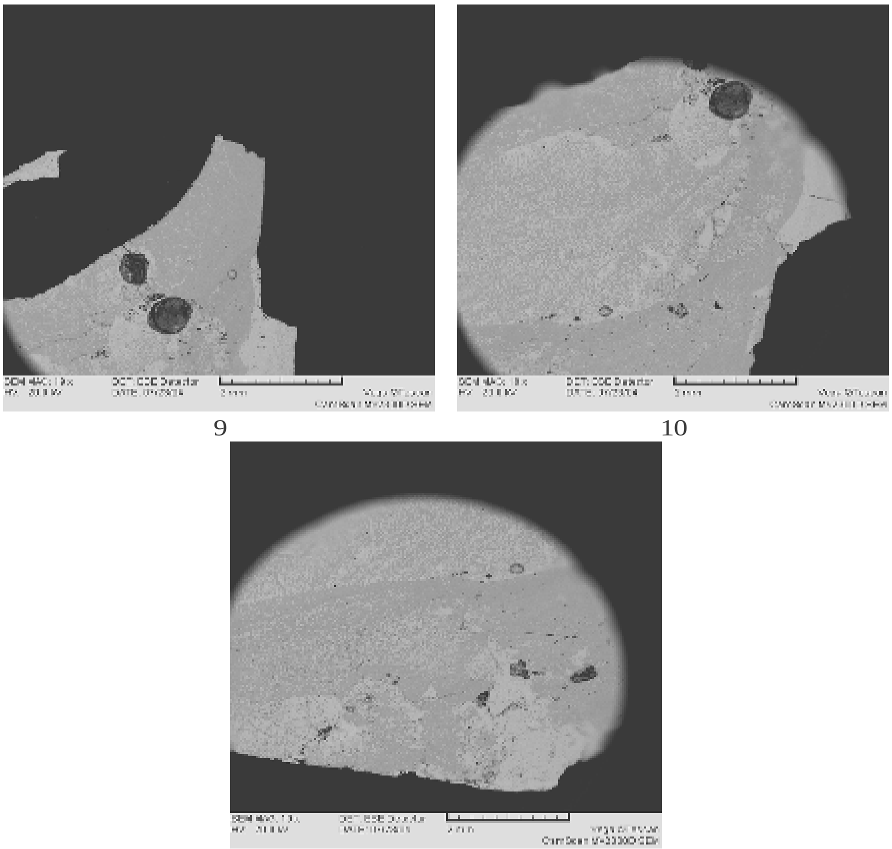

9 10

11

Fig. 3.20. Micrographs of regions 9-11 in the bottom layer of the ingot from CORD30

CORD33

Templates were produced from melt samples and analyzed (Figs. 3.16–3.18, Tabs. 3.24–3.26). All samples have a fine-grain dendritic structure characteristic of the conditions of rapid quenching. To all appearance , the dendrite-forming phase is (α-Zr(O)) with a small content of iron (Fig. 3.21, Tab. 3.24, Points P2, P4, P6). Due to the absence of clear phase boundaries, other phases were impossible to identify.

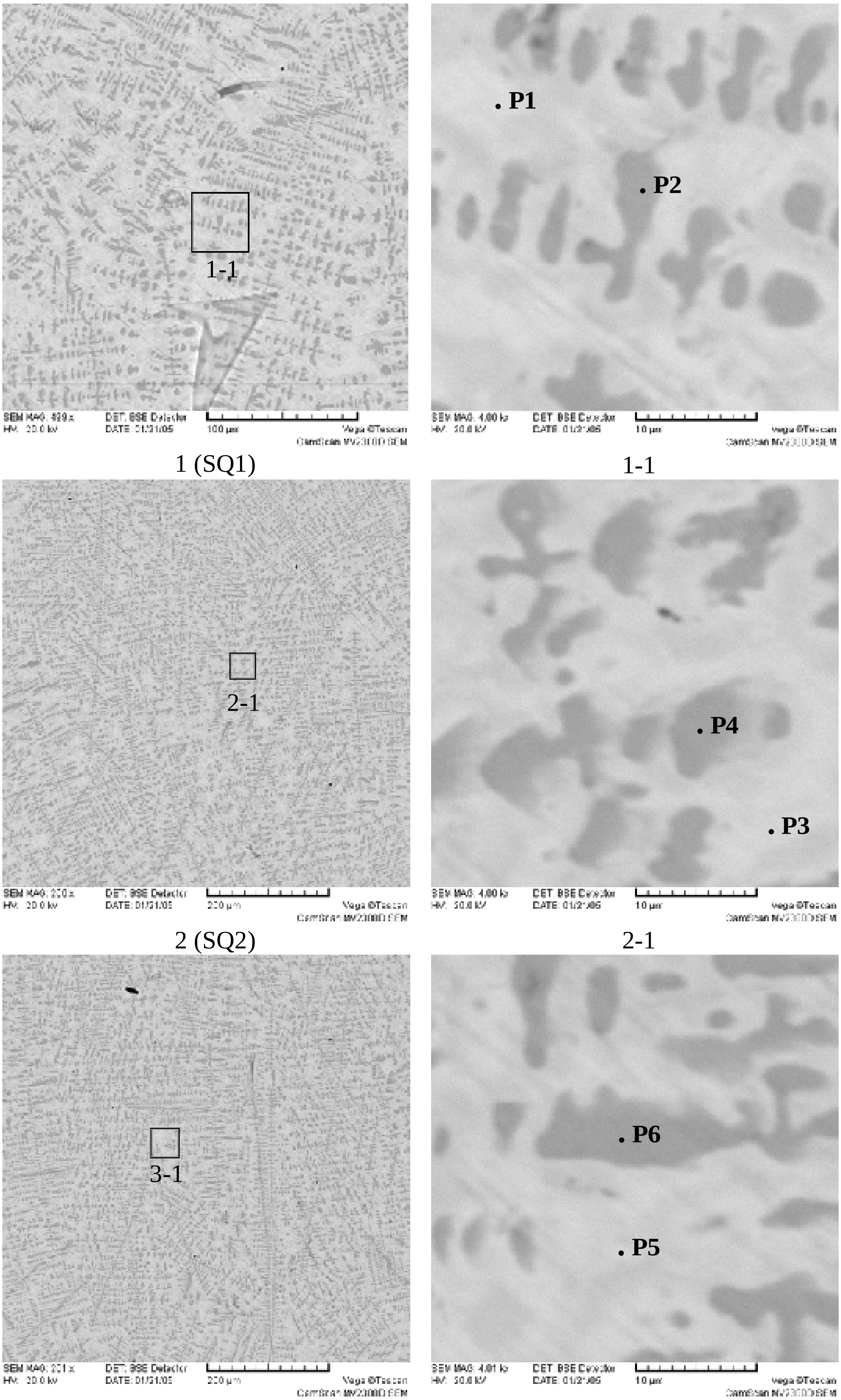

1 (SQ1) 1-1

2 (SQ2) 2-1

3 (SQ3) 3-1

Fig. 3.21. Micrographs of sample No.2 (2480°C) from CORD33

Table 3.24. EDX data for sample No.2

No.		Zr	Fe	O
SQ1	mass %	72.62	20.27	7.11
	mol.%	49.64	22.63	27.72
SQ2	mass %	72.57	20.07	7.37
	mol.%	49.25	22.24	28.51
SQ3	mass %	72.70	20.31	6.99
	mol.%	49.89	22.76	27.34
P1	mass %	80.08	15.01	4.91
	mol.%	60.39	18.48	21.13
P3	mass %	68.45	25.92	5.62
	mol.%	47.91	29.64	22.45
P5	mass %	70.82	25.44	3.74
	mol.%	52.96	31.08	15.96
P2	mass %	79.99	1.20	18.81
	mol.%	42.28	1.03	56.69
P4	mass %	80.83	1.91	17.26
	mol.%	44.33	1.71	53.96
P6	mass %	80.51	1.13	18.36
	mol.%	43.05	0.99	55.96

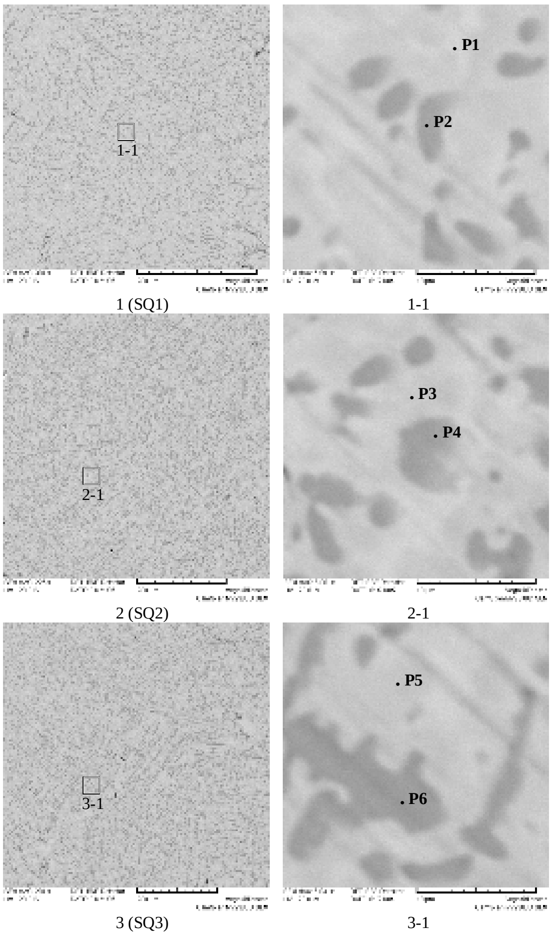

1 (SQ1) 1-1

2 (SQ2) 2-1

3 (SQ3) 3-1

Fig. 3.22. Micrographs of sample No.3 (2390°C) from CORD33

Table 3.25. EDX data for sample No.3

No.		Zr	Fe	O
SQ1	mass %	72.87	20.98	6.15
	mol.%	51.24	24.10	24.66
SQ2	mass %	73.07	19.87	7.06
	mol.%	50.13	22.27	27.60
SQ3	mass %	73.32	20.42	6.26
	mol.%	51.51	23.43	25.06
P1	mass %	69.00	27.57	3.43
	mol.%	51.66	33.71	14.63
P3	mass %	69.84	27.01	3.15
	mol.%	52.95	33.45	13.60
P5	mass %	64.36	32.57	3.06
	mol.%	47.66	39.40	12.94
P2	mass %	78.61	5.92	15.47
	mol.%	44.54	5.48	49.98
P4	mass %	80.75	3.16	16.09
	mol.%	45.45	2.90	51.64
P6	mass %	80.79	2.33	16.88
	mol.%	44.68	2.11	53.21

After crystallization, the ingot was cut along the axis and a template was produced from one half (Fig. 3.24). It should be noted that the separation of the ingot into layers could be revealed only after polishing and etching the of the thin section. Microstructure of the top metal-rich part of the ingot is dendritic across the whole surface of the thin section (Figs. 3.26–3.28), it being the evidence of crystallization under quenching conditions. Also noteworthy is the sample's porosity, which is apparently due to shrinking of the forming intermetallic phases, or to the release of the dissolved gases. The fine-dispersed structure does help to reliably identify composition of the crystallized phases by SEM/EDX.

Microstructure of the bottom oxide-rich part is even more complicated. A refractory oxide-rich liquid is monotectic under the immiscibility conditions, and thus the monotectic structure should be observed. The analysis of microstructure of region 1 (Fig. 3.25) has shown the ZrO_{2-x} phase to be the primary crystallization phase, in which uneven distribution of intermetallic phases was observed. This may be due to the experimental procedure. Sample No.3 was taken in the end of the test (Fig. 3.4) at a temperature close to T_{liq} (2390°C), and this led to melt cooling and crust formation at the melt surface, as a consequence.

Apparently, composition of the crust corresponded to that of the primary crystallization phase of the molten pool metal-rich part. Presumably, crystallization of the oxide-rich part of the molten pool containing a large quantity of the refractory phase also occurred at this time. Then, power in the melt was increased. This caused crust melting and rising of the molten pool surface temperature. It is unknown, if the layer that had crystallized at the poll bottom melted or not. Under such a scenario, a temperature gradient in the oxide-rich layer and components repartitioning are possible and can influence the results of analysis on determining the tie-line direction. It can be asserted that during the test before sample No.3 was taken all the charge in the crucible was in the molten state and the oxidic part of the pool was located slightly above the bottom. This is confirmed by the fact that the crystallized ingot has a layer of crystallized metal-rich liquid under the oxidic layer (Fig. 3.25, region 1-1-1).

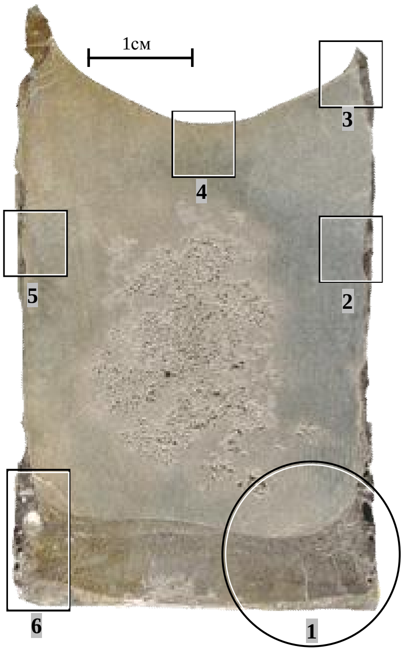

Fig. 3.24. Axial section of the ingot from CORD33 with regions marked for SEM/EDX analysis

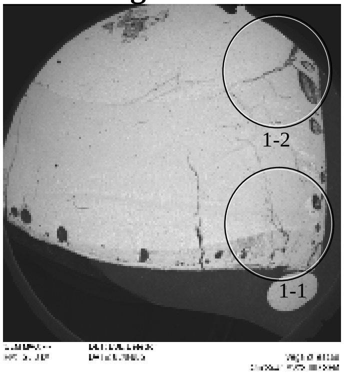

1

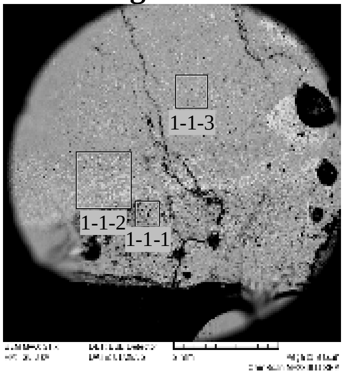

1-1

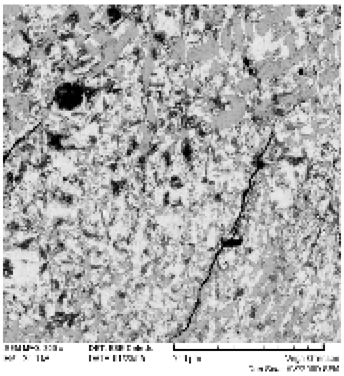

1-1-1

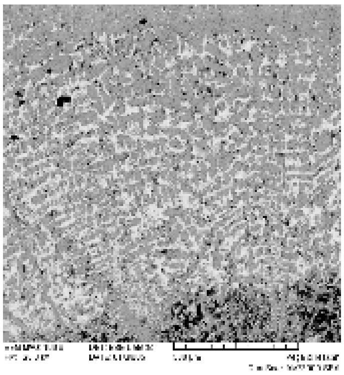

1-1-2

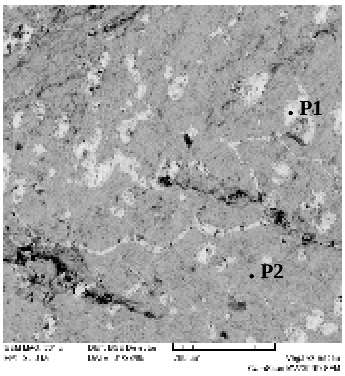

1-1-3

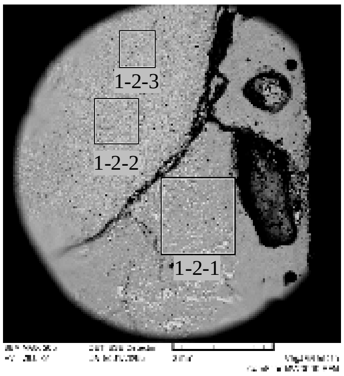

1-2

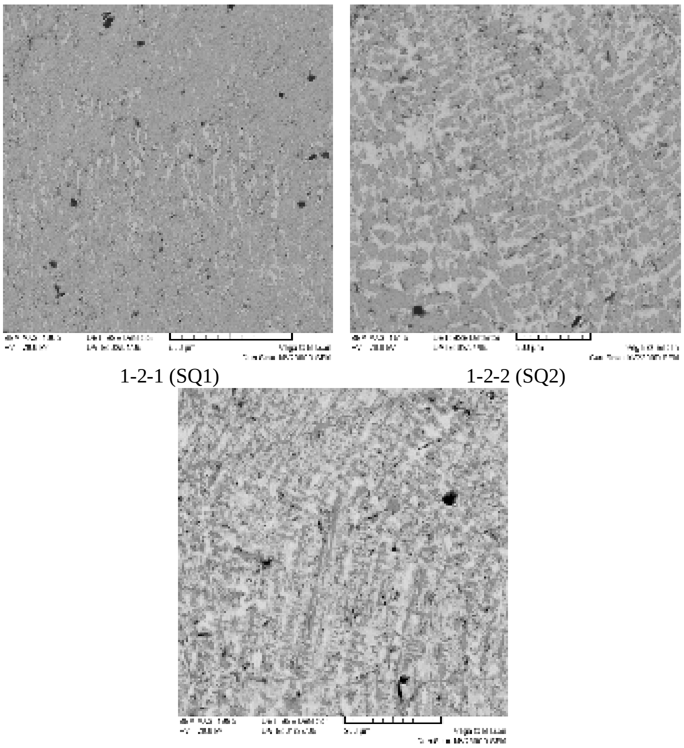

1-2-1 (SQ1)

1-2-2 (SQ2)

1-2-3

Fig. 3.25. Micrographs of region 1 in the bottom part of the ingot from CORD33

Table 3.27. EDX data for region 1

No.		Zr	Fe	O
SQ1	mass %	78.51	7.28	14.22
	mol.%	45.79	6.93	47.28
SQ2	mass %	71.84	17.99	10.17
	mol.%	45.13	18.45	36.42
P1	mass %	69.26	28.02	2.72
	mol.%	53.06	35.06	11.88
P2	mass %	83.67	0.64	15.69
	mol.%	48.05	0.60	51.35

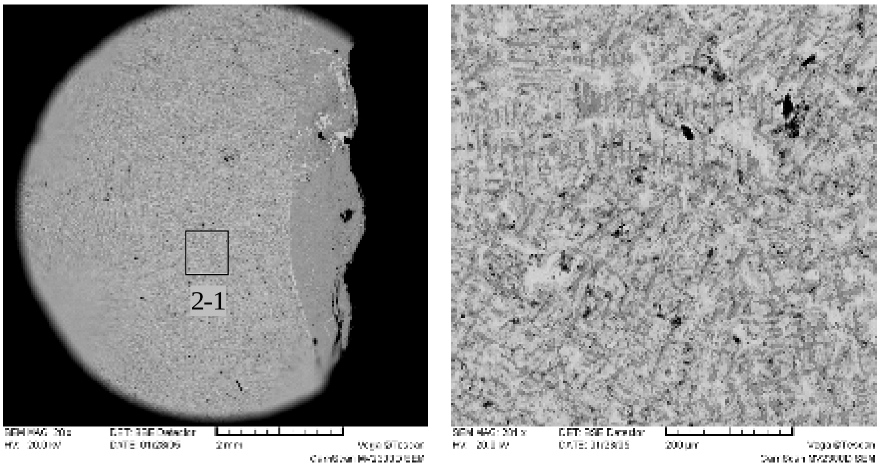

2

2-1

Fig. 3.26. Micrographs of region 2 in the top part of the ingot from CORD33

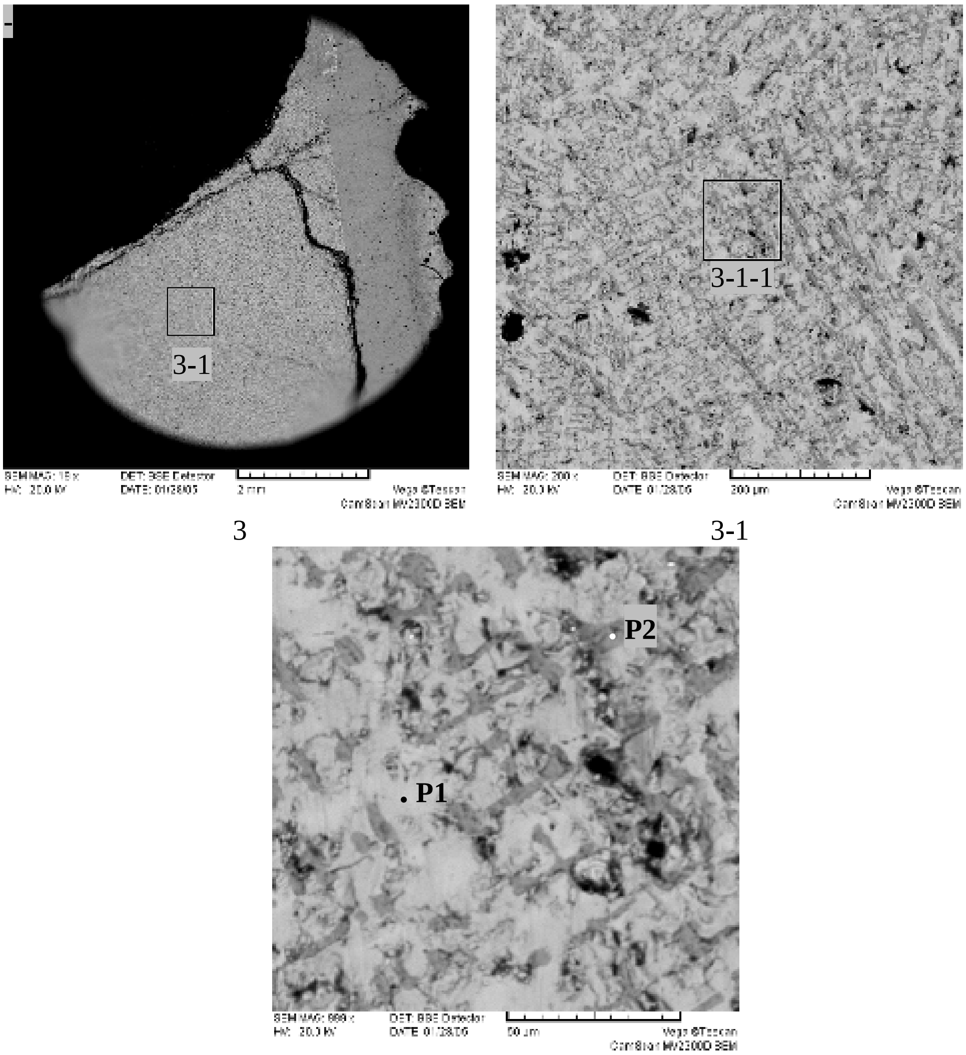

3 3-1

3-1-1

Fig. 3.27. Micrographs of region 3 in the top part of the ingot from CORD33

Table 3.28. EDX data for region 3

No.		Zr	Fe	O
P1	mass %	71.07	25.92	3.01
	mol.%	54.43	32.42	13.15
P2	mass %	80.23	5.78	13.98
	mol.%	47.36	5.58	47.06

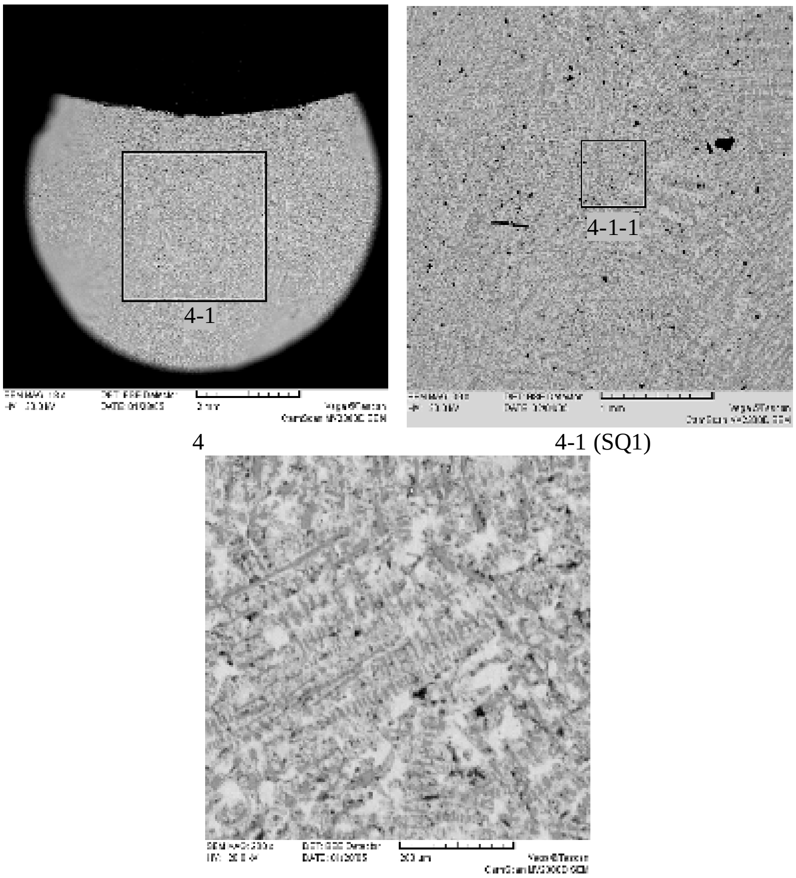

4 4-1 (SQ1)

4-1-1

Fig. 3.28. Micrographs of region 4 in the top part of the ingot from CORD33

Table 3.29. EDX data for region 4

No.		Zr	Fe	O
SQ1	mass %	64.84	18.24	16.93
	mol.%	33.92	15.58	50.49
	mol.% MeO_x	68.52	31.48	

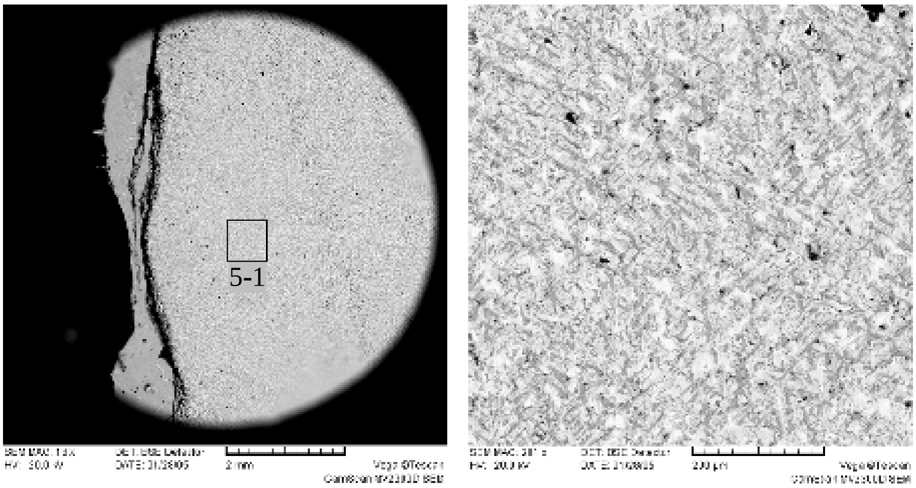

5 5-1

Fig. 3.29. Micrographs of region 5 in the top part of the ingot from CORD33

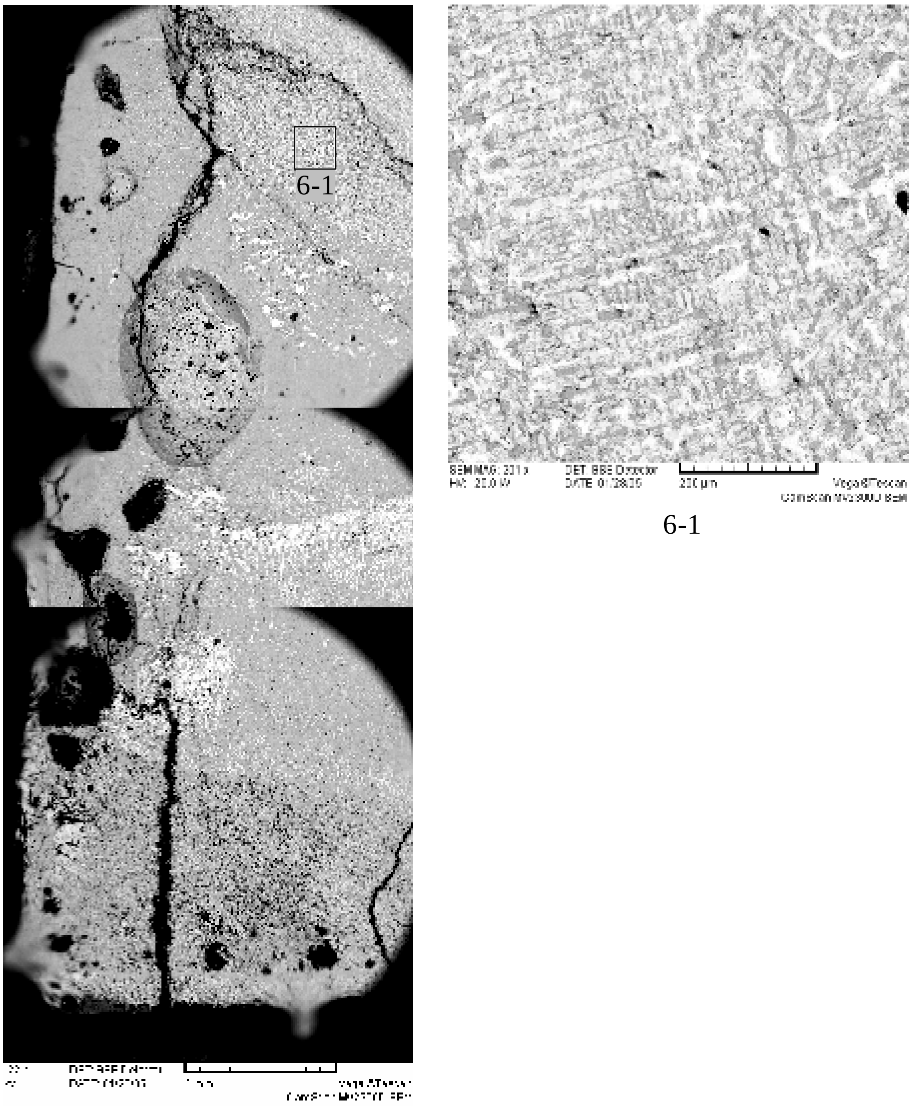

6

6-1

Fig. 3.30. Micrographs of region 6 in the bottom part of the ingot from CORD33

CORD35

It has been mentioned above that the test included a lengthy process of equilibrium crystallization of the melt in the bottom and peripheral parts of the pool. Crystallization was achieved by means of slow vertical shifting of the crucible relative to the inductor. The molten pool was cooling at its bottom when leaving the inductor electromagnetic field. This was leading to the reduction of total heat content in the melt and crystallization of the latter at the bottom and along periphery of the pool in accordance with the equilibrium diagram.

Before crystallization began, two rod samples were taken. Sample No.1 was taken hot from the crucible and its surface got partially oxidized. To our opinion, the regions of the sample adjoining the rod did not get oxidized. After crystallization of the molten pool for 4 hours 25 min, the 3rd rod sample was taken from the still uncrystallized part. The samples were meant for comparing melt compositions before and after crystallization of a part of the molten pool. The results of SEM/EDX analysis of the samples are presented in Figs. 3.31–3.33 and in Tabs. 3.30–3.32. Bulk composition of the 1st and 2nd samples corresponded to that of samples from CORD33, thus showing results reproducibility. The 3rd sample was depleted in oxygen as the result of ZrO_{2-x}, crystallization (to be shown below).

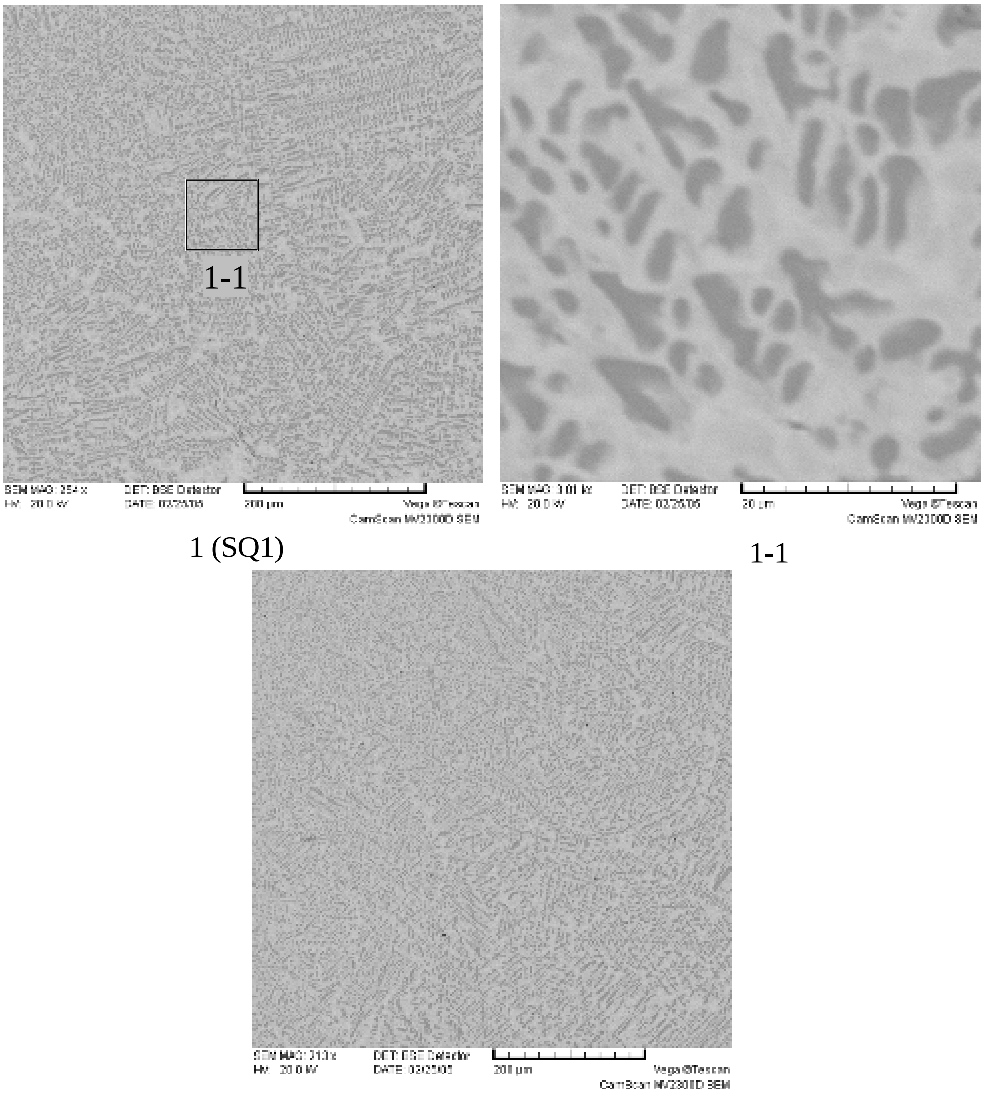

1 (SQ1)

1-1

2 (SQ2)

Fig. 31. Micrographs of sample No.1 from CORD35 (T=2475°C)

Table 3.30. EDX data for sample No.1

No.		Zr	Fe	O
SQ1	mass %	72.87	19.16	7.97
	mol.%	48.71	20.92	30.37
	mol.% MeO_x	69.95	30.05	
SQ2	mass %	72.72	20.23	7.05
	mol.%	49.82	22.64	27.54
	mol.% MeO_x	68.76	31.24	

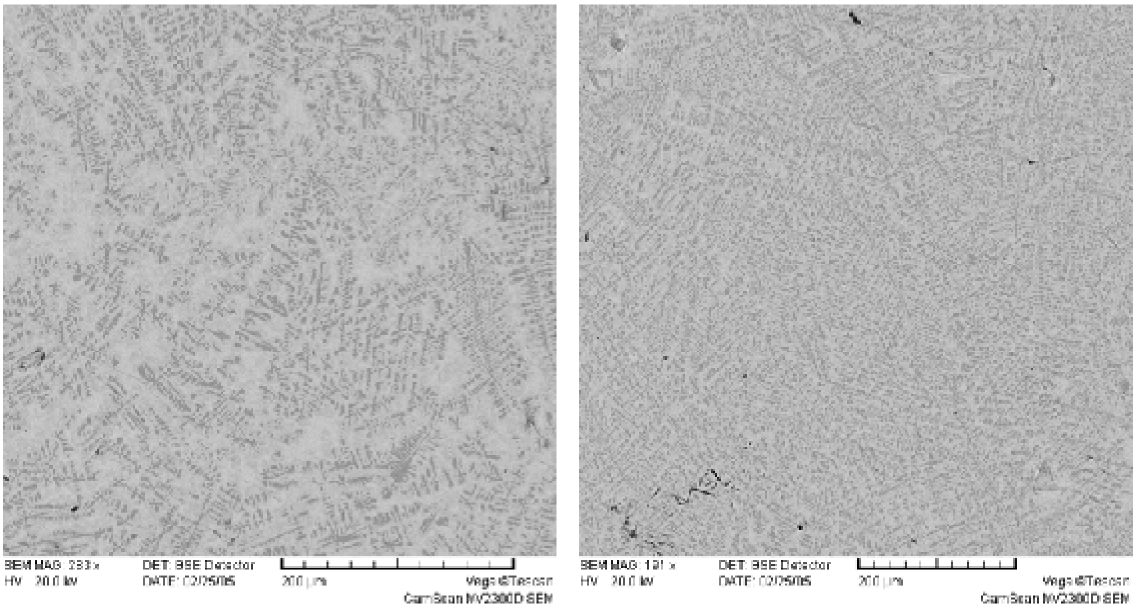

1 (SQ1) 2 (SQ2)

Fig.3.32. Micrographs of sample No.2 from CORD35 (T=2400°C)

Table 3.31. EDX data for sample No.2

No.		**Zr**	**Fe**	**O**
SQ1	mass %	71.86	21.27	6.87
	mol.%	49.29	23.83	26.87
	mol.% MeO_x	67.41	32.59	
SQ2	mass %	72.38	20.63	6.99
	mol.%	49.60	23.09	27.31
	mol.% MeO_x	68.23	31.77	

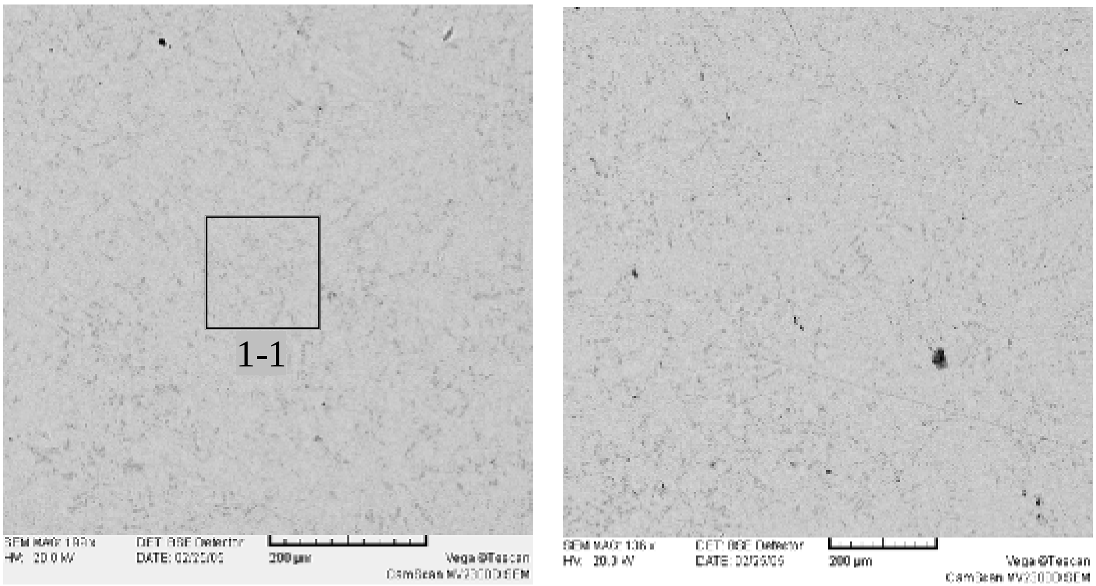

1 (SQ1) 2 (SQ2)

Fig.3.33. Micrographs of sample No.3 from CORD35 (T=2120°C)

Table 3.32. EDX data for sample No.3

No.		Zr	Fe	O
SQ1	mass %	75.50	19.82	4.68
	mol.%	56.11	24.06	19.83
	mol.% MeO_x	69.99	30.01	
SQ2	mass %	74.82	20.47	4.71
	mol.%	55.38	24.75	19.88
	mol.% MeO_x	69.11	30.89	

The ingot produced by cooling the melt from 2120°C, was cut along the axis and a template was produced from one half (Fig. 3.34). The SEM/EDX results for the examined regions are presented in Figs. 3.35–3.43 and in Tabs. 3.33–3.36. The ingot periphery and its bottom part demonstrate the crystallized layer of the equilibrium primary crystallization phase, which has a clear boundary with the rest of the cooled melt. Microstructure of the primary crystallization phase layer may be observed in the examined regions 4, 6–10 (Fig. 3.34). This layer consists of the ZrO_2 and α-Zr(O) phases (Fig. 3.38, Tab. 3.34). Depending on the temperature of the layer and direction of the heat removal isotherm, the α-Zr(O) phase was crystallizing in the form of threads and round inclusions. The treads of α-Zr(O) alternate with ZrO_2 so densely that is it impossible to clearly identify the ZrO_2 phase.

Fig. 3.34. Axial cut of the ingot from CORD35 (cooled from 2120°C) with regions marked for SEM/EDX examination

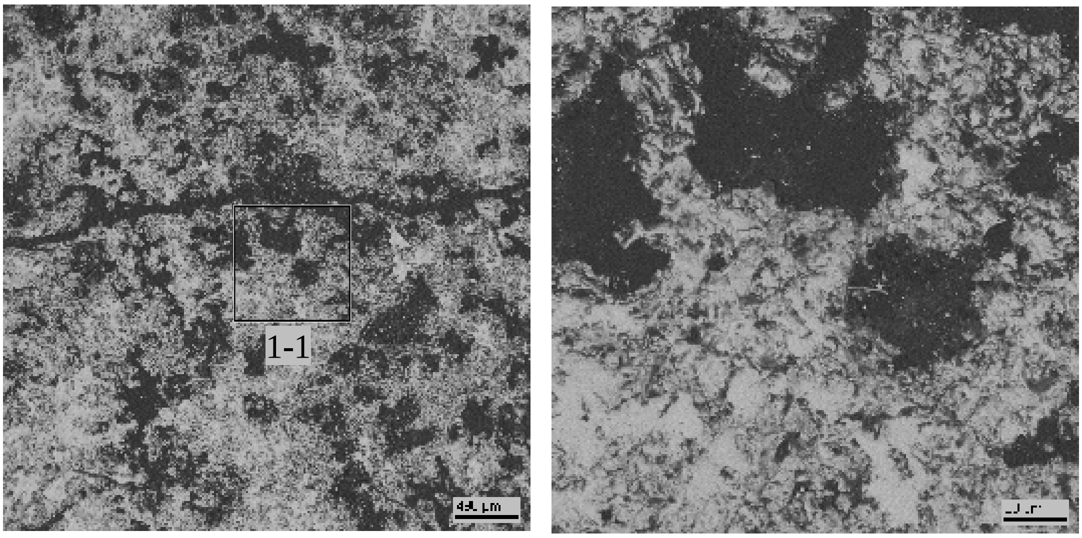

1

1-1

Fig. 3.35. Micrographs of region 1 in the ingot from CORD35

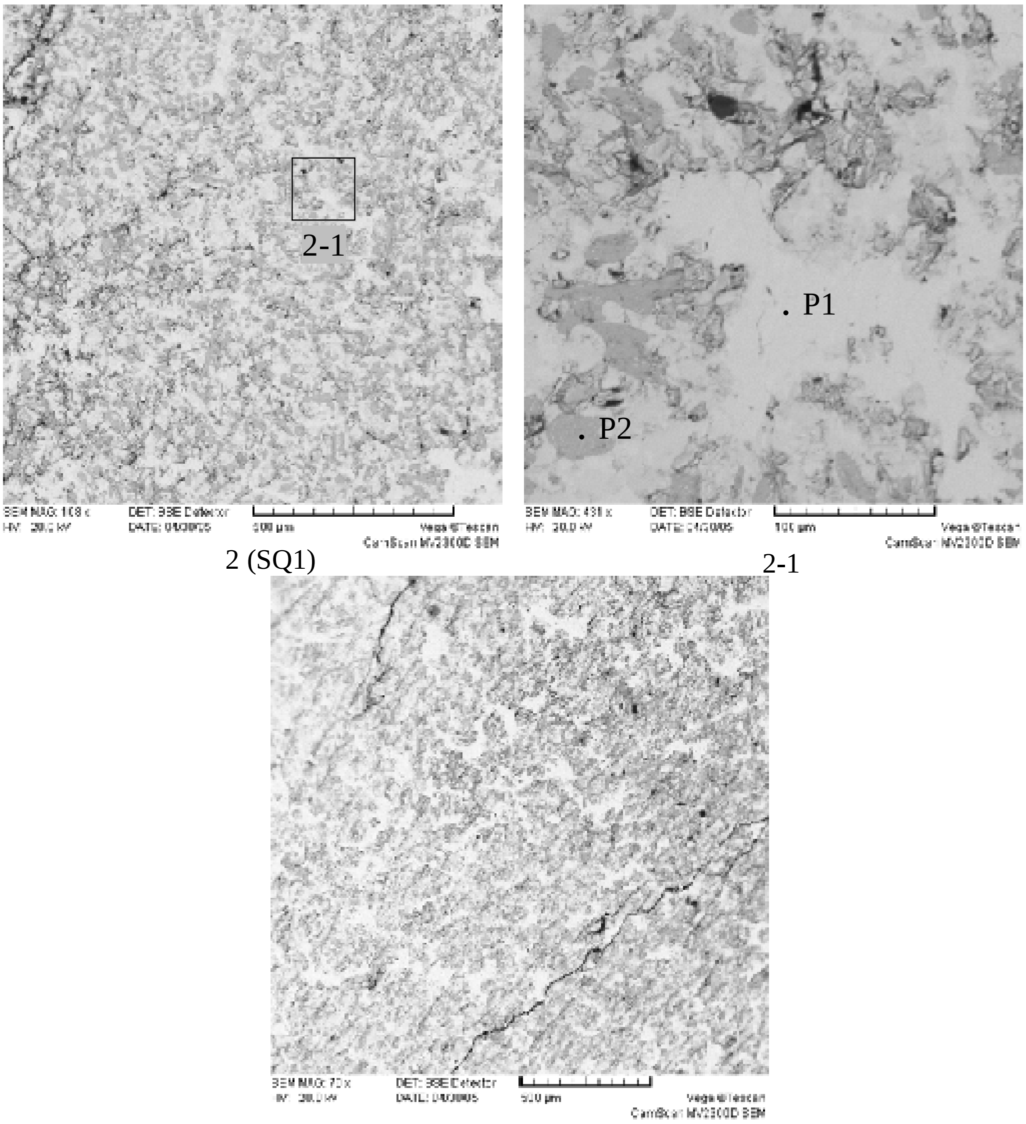

2 (SQ1)

2-1

3 (SQ2)

Fig. 3.36. Micrographs of regions 2 and 3 in the ingot from CORD35

Table 3.33. EDX data for regions 2 and 3

No.		Zr	Fe	O
SQ1	mass %	74.5	17.71	7.79
	mol.%	50.39	19.57	30.04
	mol.% MeO_x	72.03	27.97	
SQ2	mass %	72.34	20.85	6.81
	mol.%	49.81	23.45	26.74
	mol.% MeO_x	67.99	32.01	
P1	mass %	76.26	21.13	2.61
	mol.%	60.69	27.47	11.84
	mol.% MeO_x	68.84	31.16	
P2	mass %	84.2	0.68	15.12
	mol.%	49.09	0.65	50.26
	mol.% MeO_x	98.7	1.3	

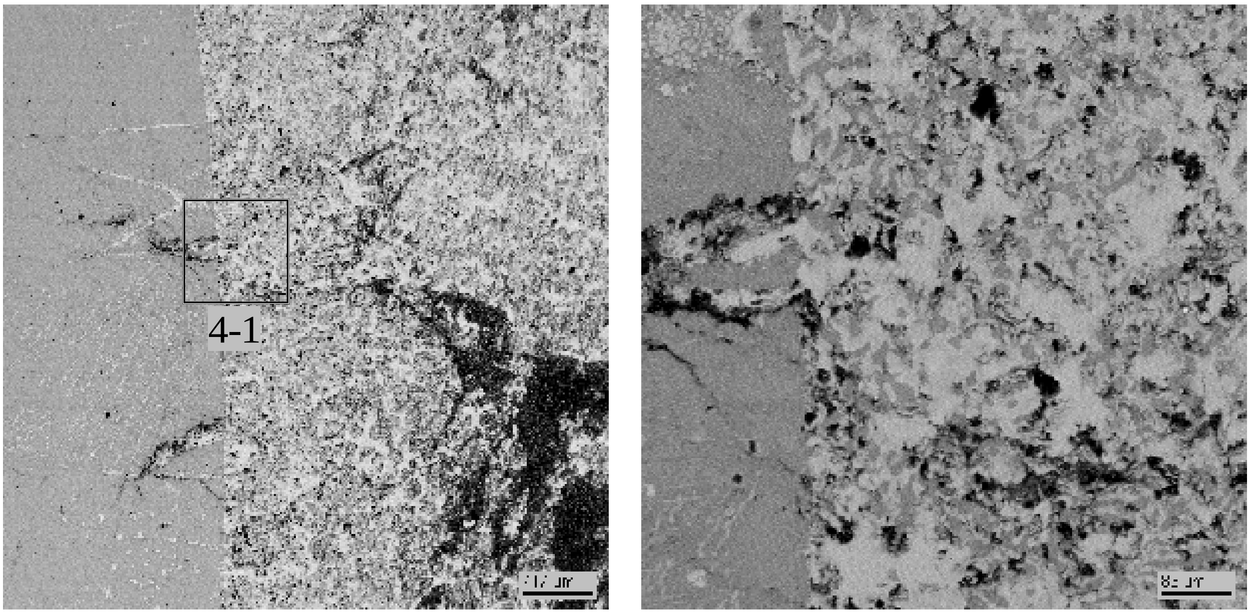

4 4-1

Fig. 3.37. Micrographs of region 4 in the ingot from CORD35

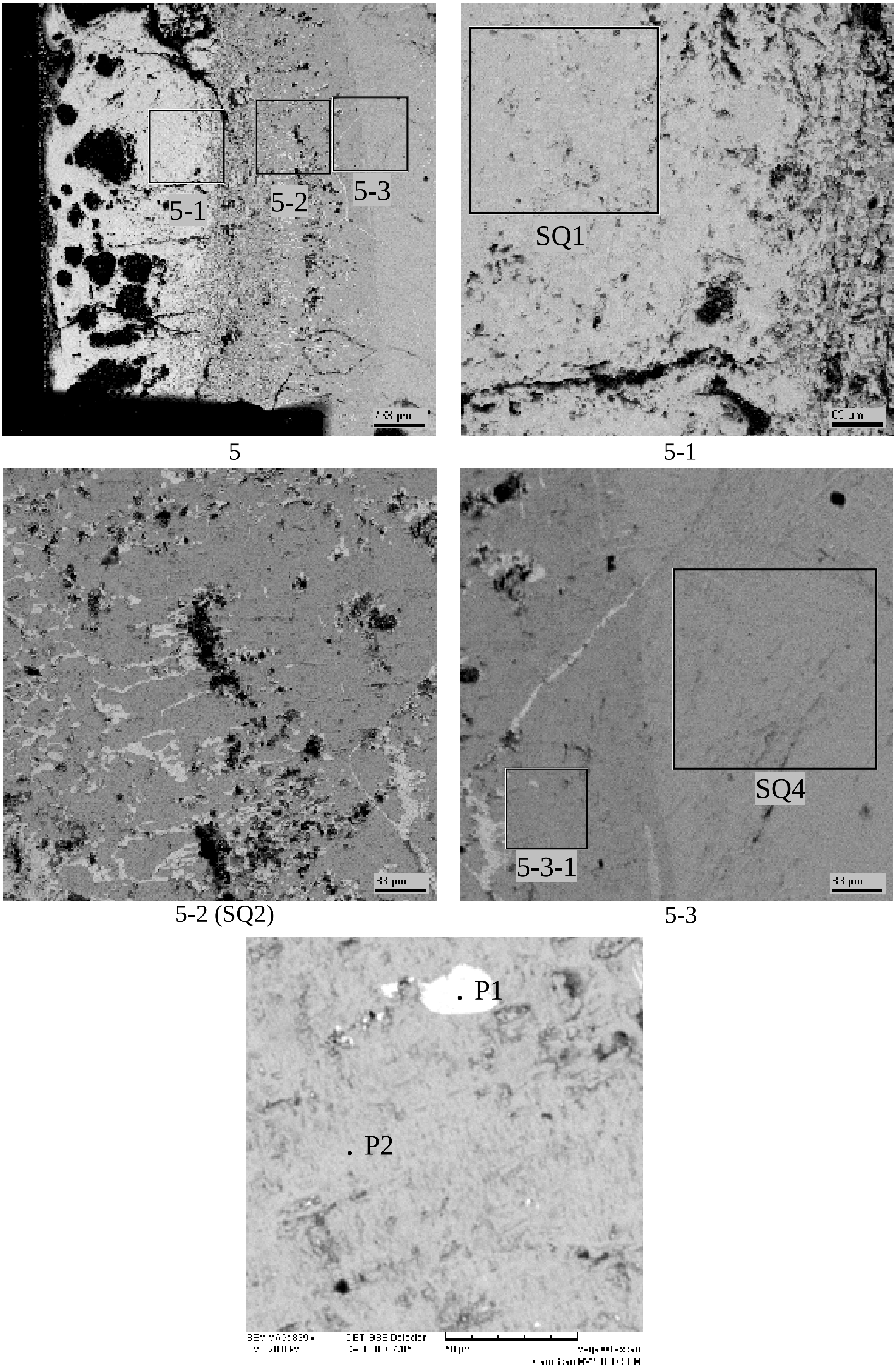

5

5-1

5-2 (SQ2)

5-3

5-3-1 (SQ3)

Fig. 3.38. Micrographs of region 5 in the ingot from CORD35

Table 3.34. EDX data for region 5

No.		Zr	Fe	O
SQ1	mass %	73.51	21.34	5.15
	mol.%	53.37	25.31	21.32
	mol.% MeO_x	67.83	32.17	
SQ2	mass %	82.71	0.55	16.74
	mol.%	46.19	0.50	53.31
	mol.% MeO_x	98.93	1.07	
SQ3	mass %	83.61	-	16.39
	mol.%	47.22	-	52.78
	mol.% MeO_x	100	-	
SQ4	mass %	83.87	-	16.13
	mol.%	47.70	-	52.30
	mol.% MeO_x	100	-	
P1	mass %	94.27	-	5.73
	mol.%	74.26	-	25.74
	mol.% MeO_x	100	-	
P2	mass %	83.98	-	16.02
	mol.%	47.90	-	52.10
	mol.% MeO_x	100	-	

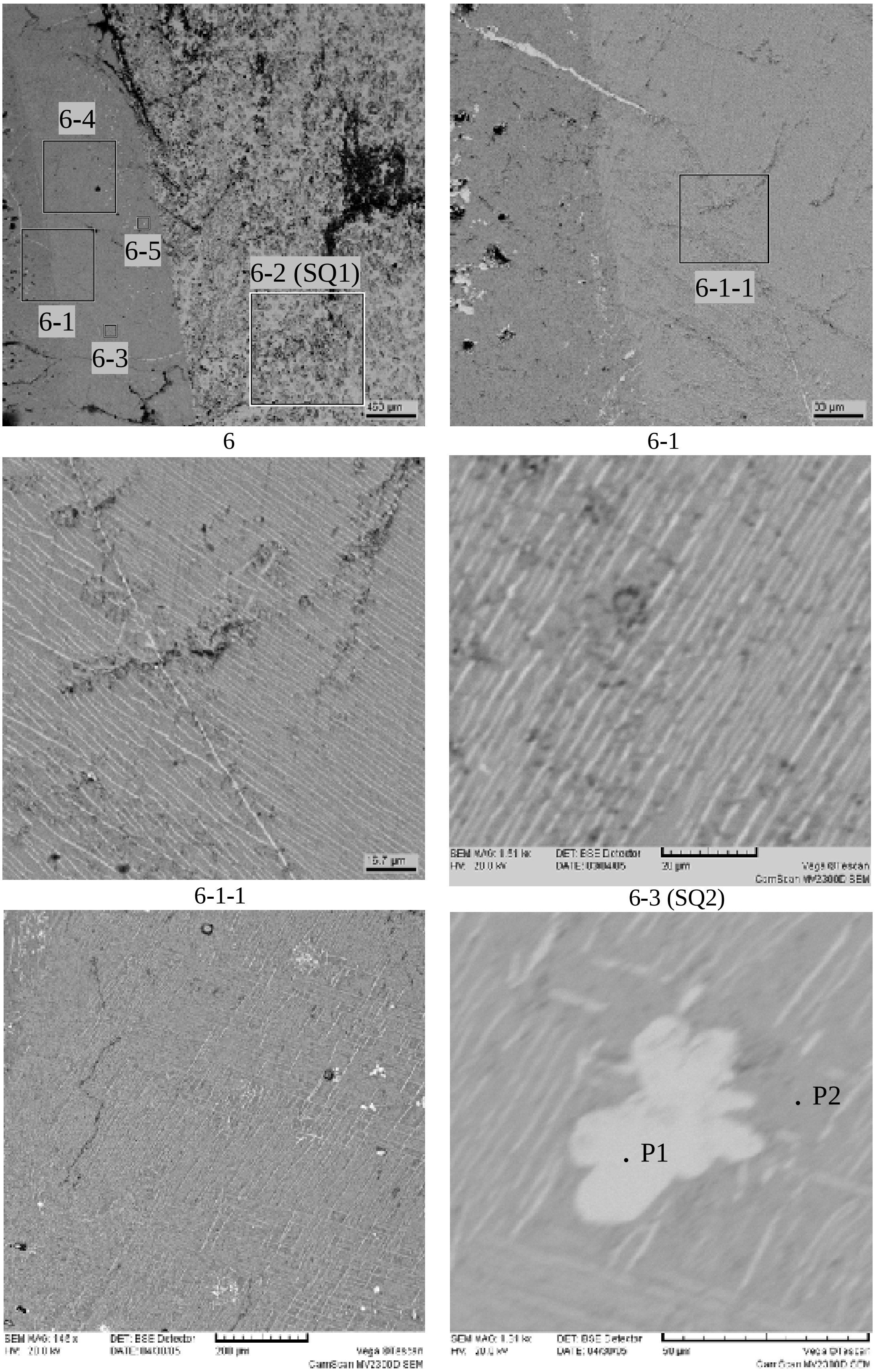

6 6-1

6-1-1 6-3 (SQ2)

6-4 (SQ3) 6-5

Fig. 3.39. Micrographs of region 6 in the ingot from CORD35

Table 3.35. EDX data for region 6

No.		Zr	Fe	O
SQ1	mass %	74.60	17.67	7.73
	mol.%	50.56	19.56	29.87
	mol.% MeO$_x$	72.10	27.90	
SQ2	mass %	84.65	-	15.35
	mol.%	49.17	-	50.83
	mol.% MeO$_x$	100	-	
SQ3	mass %	84.97	-	15.03
	mol.%	49.79	-	50.21
	mol.% MeO$_x$	100	-	
P1	mass %	94.73	-	5.27
	mol.%	75.92	-	24.08
	mol.% MeO$_x$	100	-	
P2	mass %	84.69	-	15.31
	mol.%	49.24	-	50.76
	mol.% MeO$_x$	100	-	

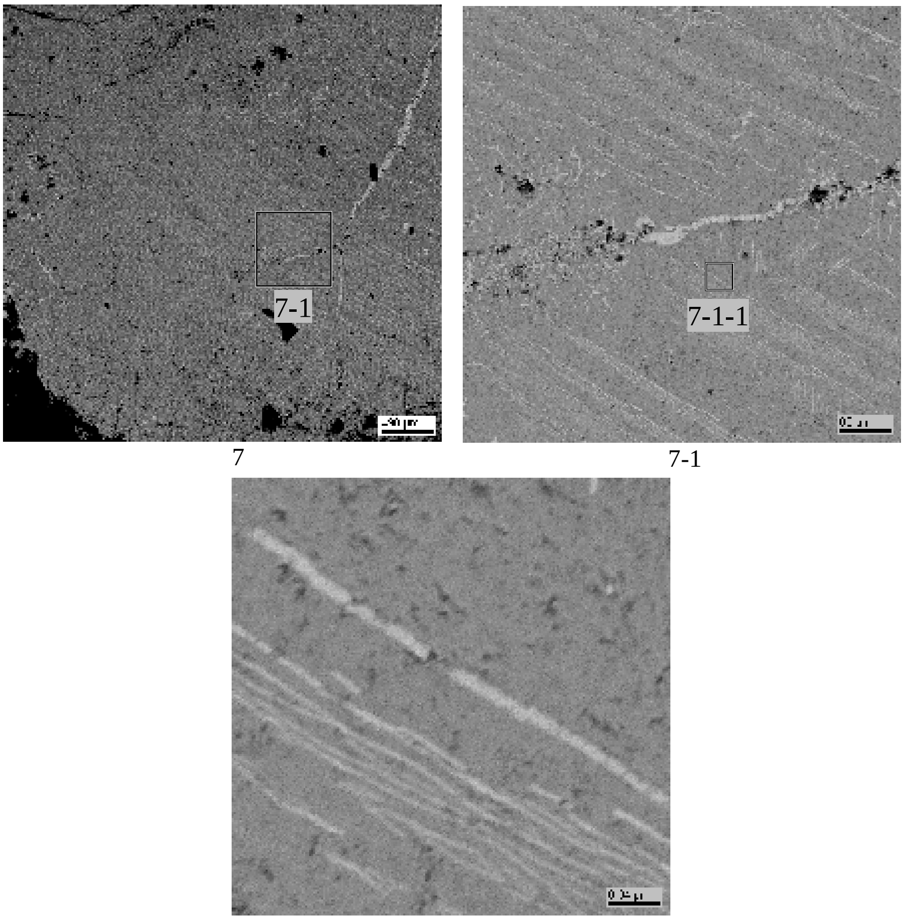

7 7-1

7-1-1

Fig. 3.40. Micrographs of region 7 in the ingot from CORD35

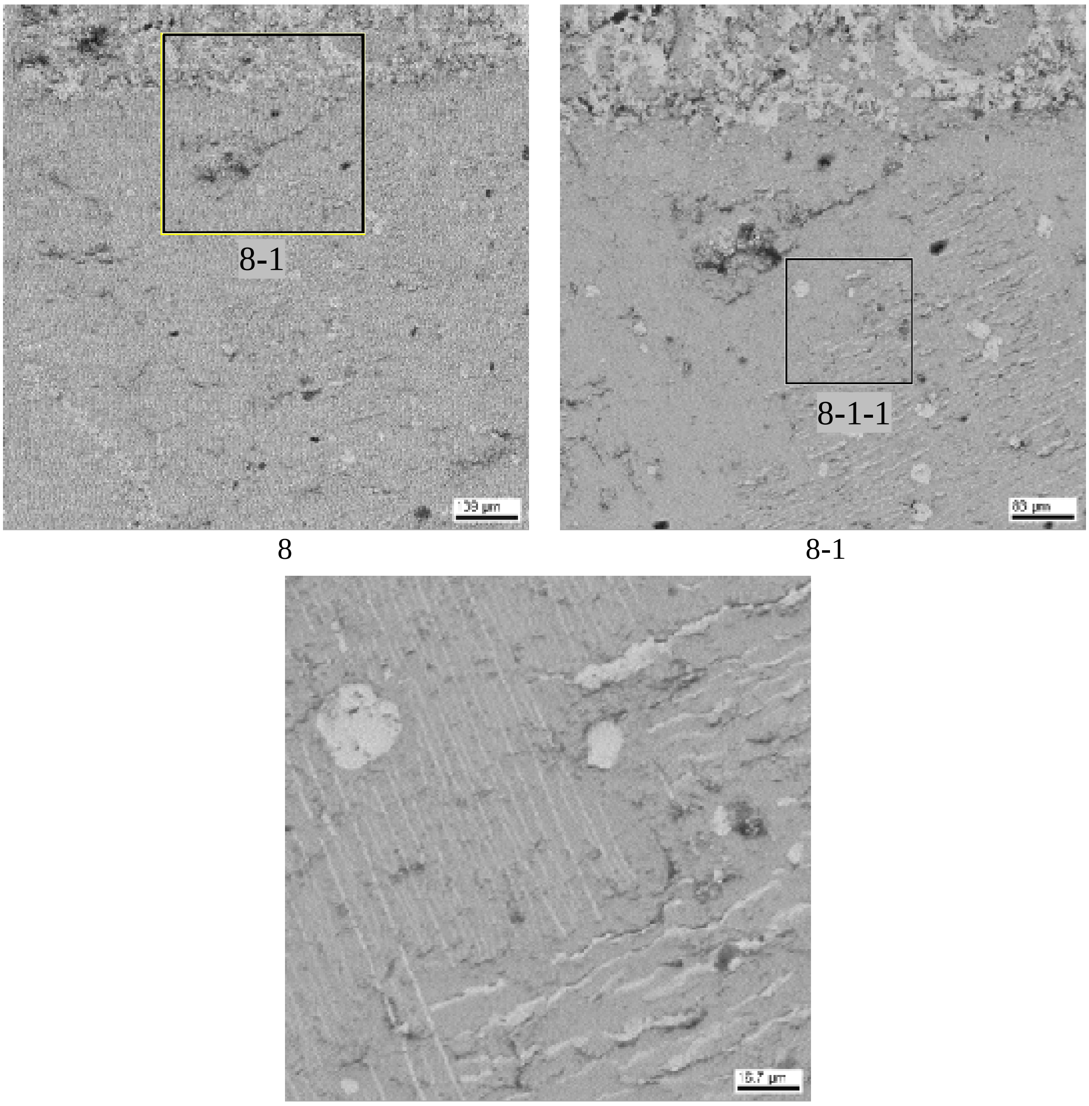

8 8-1

8-1-1 (SQ1)

Fig. 3.41. Micrographs of region 8 in the ingot from CORD35

Table 3.36. EDX data for region 8

No.		Zr	Fe	O
SQ1	mass %	84.82	-	15.18
	mol.%	49.49	-	50.51
	mol.% MeO_x	100	-	

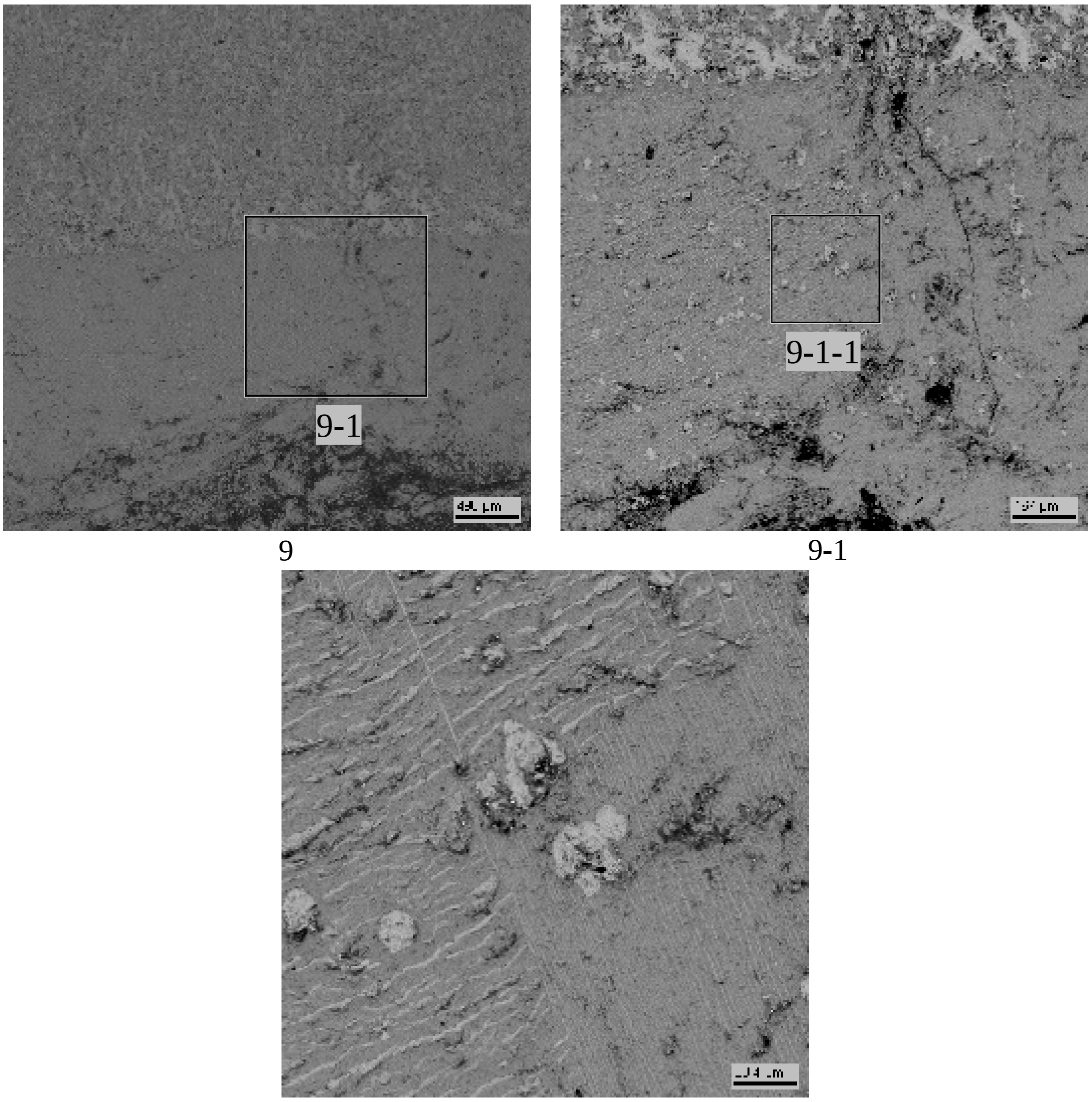

9 9-1

9-1-1

Fig. 3.42. Micrographs of region 9 in the ingot from CORD35

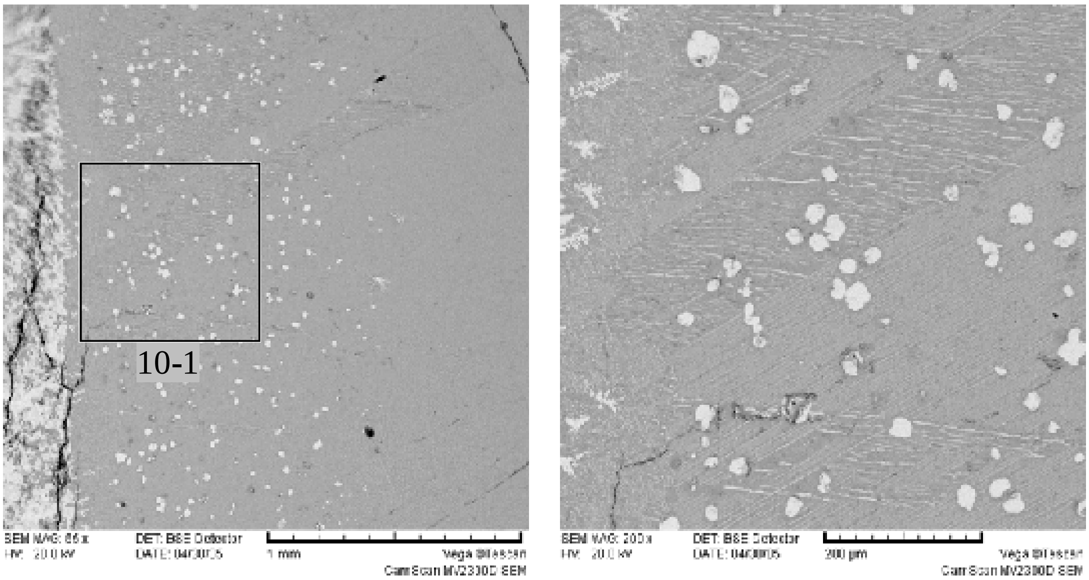

10 10-1

Fig. 3.43. Micrographs of region 10 in the ingot from CORD35

CORD39

Two rod samples of the melt were taken during the test and conventionally divided into several parts. Sample No.1 was divided into 4 and sample No.2 into two parts (Fig. 3.39). The results of SEM/EDX analysis of rod samples are given in Figs. 3.45–3.50 and in Tabs.3.37–3.42. Bulk composition of the sample parts is different. Separation of the second liquid has been observed in the samples' microstructure. It may be he result of secondary separation, or capturing of the second liquid when sampling was performed. In sample No.2-2 (Fig.3.50, Tab. 3.42) three phases can be distinguished: the $Zr_2Fe(O)$ intermetallic phase, $ZrFe_2(O)$ intermetallic phase and ZrO_2 with a small content of iron.

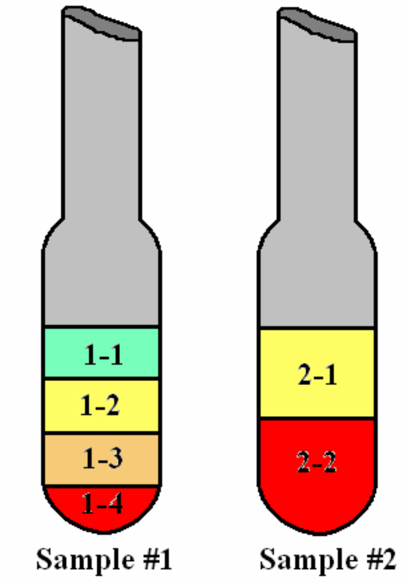

Fig. 3.44. Sketch of rod samplers from CORD39 with sampling regions marked for examination

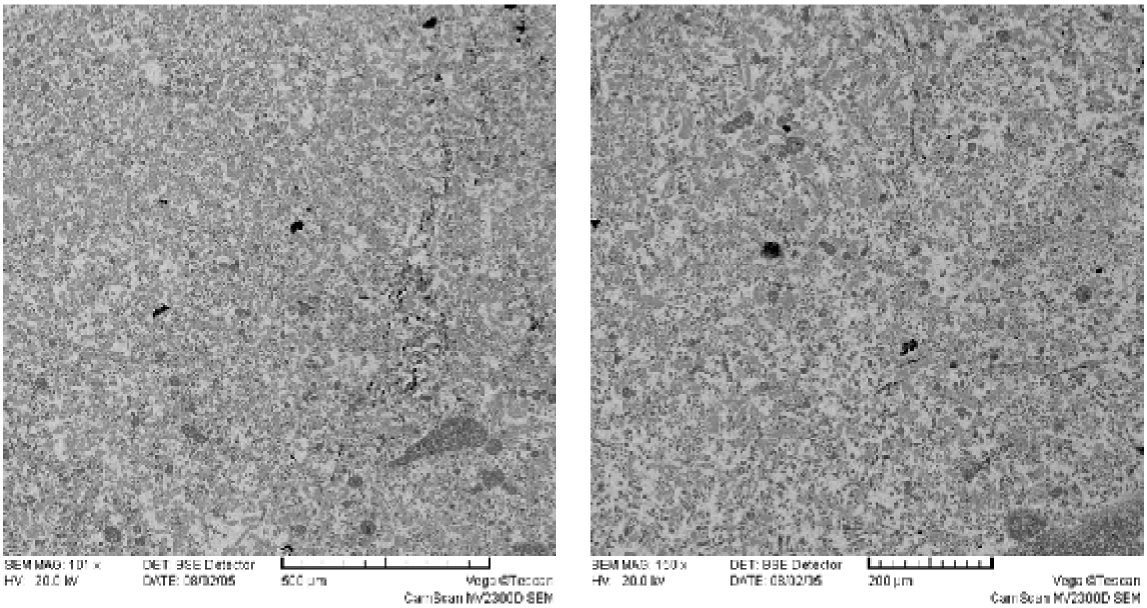

1 (SQ1)

2 (SQ2)

Fig. 3.45. Micrographs of sample No.1-1 from CORD39

Table 3.37. EDX data for sample No.1-1

No.		Zr	Fe	O
SQ1	mass %	61.61	29.53	8.86
	mol.%	38.42	30.08	31.49
	mol.% MeO_x	56.09	43.91	
SQ2	mass %	63.06	27.74	9.2
	mol.%	39.21	28.18	32.61
	mol.% MeO_x	58.19	41.81	

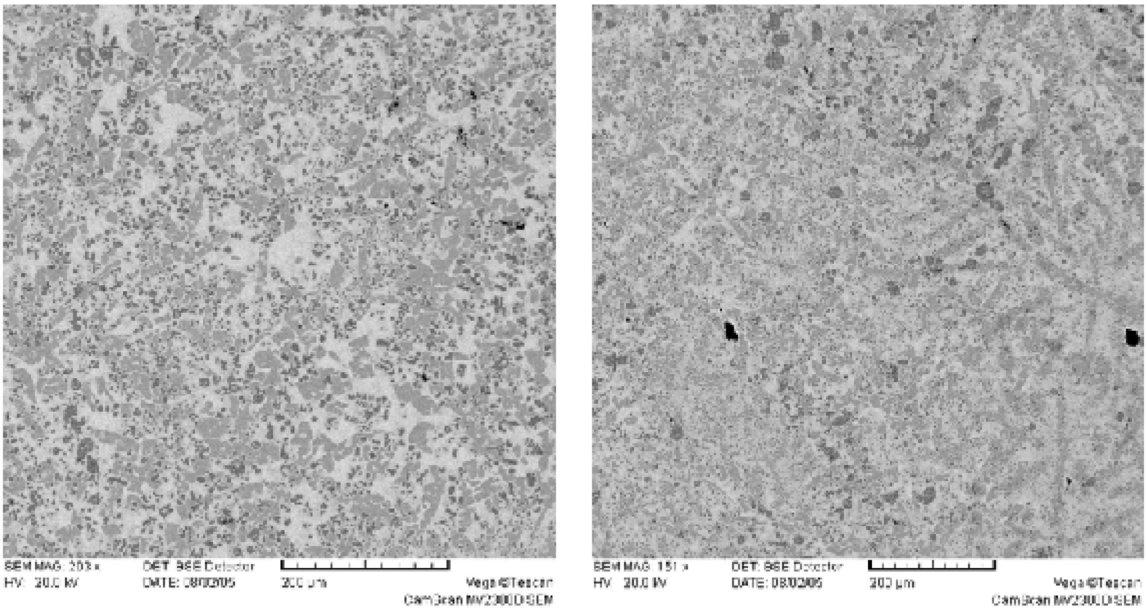

1 (SQ1) 2 (SQ2)

Fig. 3.46. Micrographs of sample No.1-2 from CORD39

Table 3.38. EDX data for sample No.1-2

No.		Zr	Fe	O
SQ1	mass %	61.25	30.72	8.03
	mol.%	38.96	31.92	29.12
	mol.% MeO_x	54.97	45.03	
SQ2	mass %	61.62	30.57	7.81
	mol.%	39.48	31.99	28.53
	mol.% MeO_x	55.24	44.76	

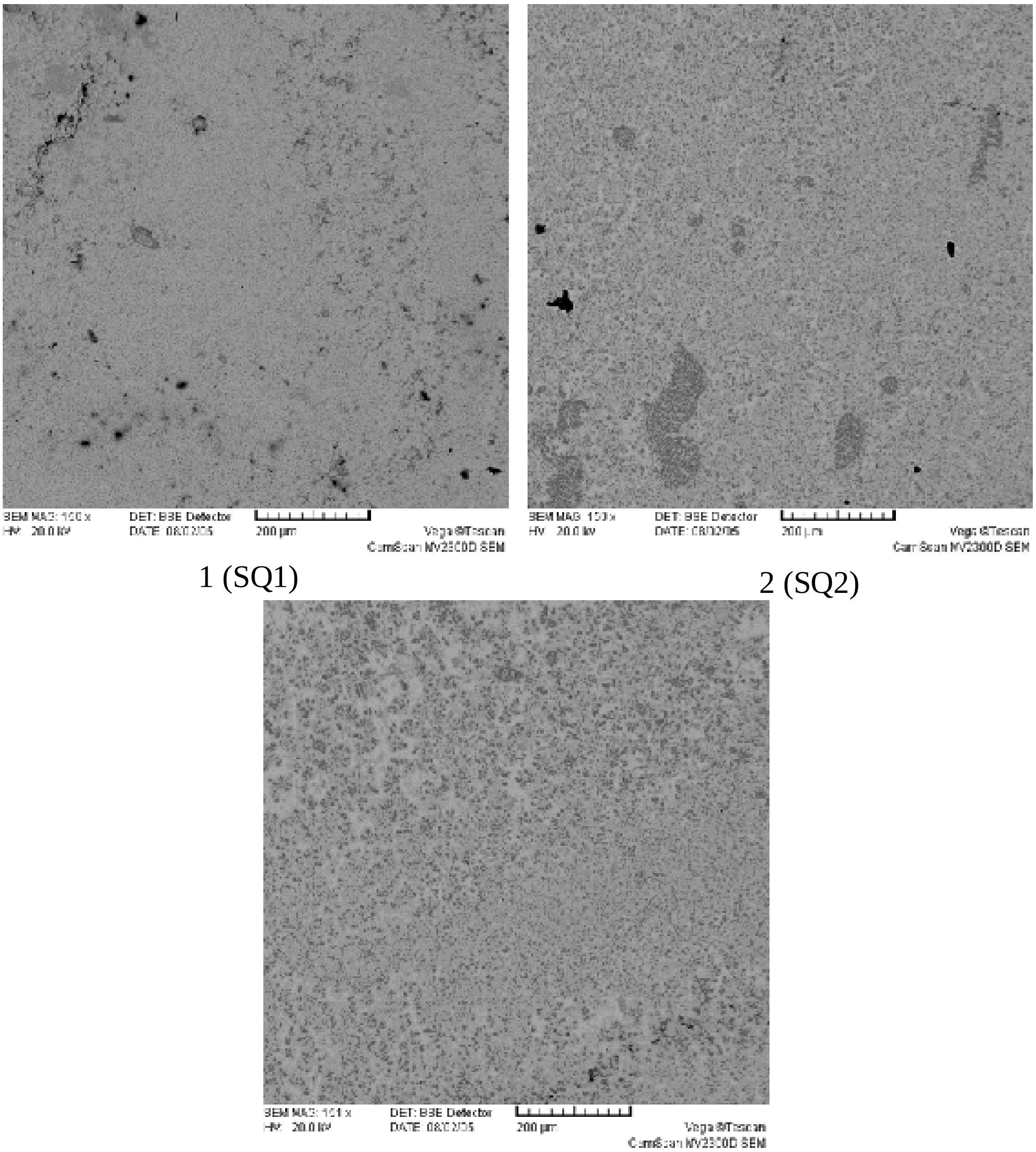

1 (SQ1)

2 (SQ2)

3 (SQ3)

Fig. 3.47. Micrographs of sample No.1-3 from CORD39

Table 3.39. EDX data for sample No.1-3

No.		Zr	Fe	O
SQ1	mass %	64.00	26.76	9.24
	mol.%	39.90	27.25	32.85
	mol.% MeO_x	59.41	40.59	
SQ2	mass %	65.07	25.73	9.20
	mol.%	40.78	26.34	32.89
	mol.% MeO_x	60.76	39.24	
SQ3	mass %	64.80	26.71	8.49
	mol.%	41.32	27.81	30.87
	mol.% MeO_x	59.76	40.24	

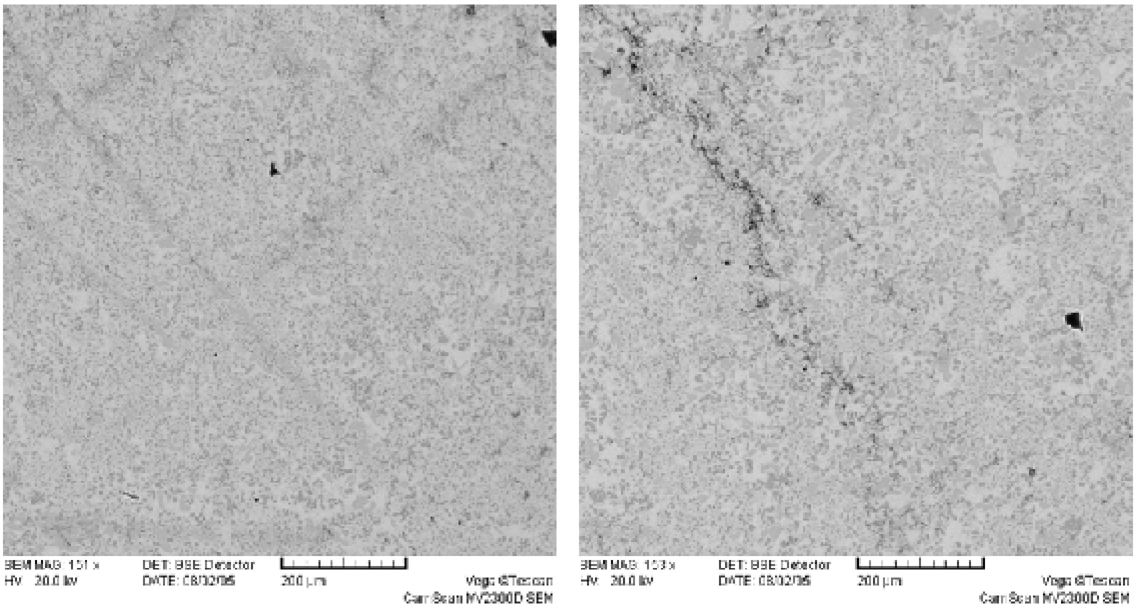

1 (SQ1) 2 (SQ2)

Fig. 3.48. Micrographs of sample No.1-4 from CORD39

Table 3.40. EDX data for sample No.1-4

No.		**Zr**	**Fe**	**O**
SQ1	mass %	61.65	28.5	9.85
	mol.%	37.51	28.32	34.17
	mol.% MeO$_x$	56.98	43.02	
SQ2	mass %	61.33	29.28	9.39
	mol.%	37.7	29.4	32.9
	mol.% MeO$_x$	56.18	43.82	

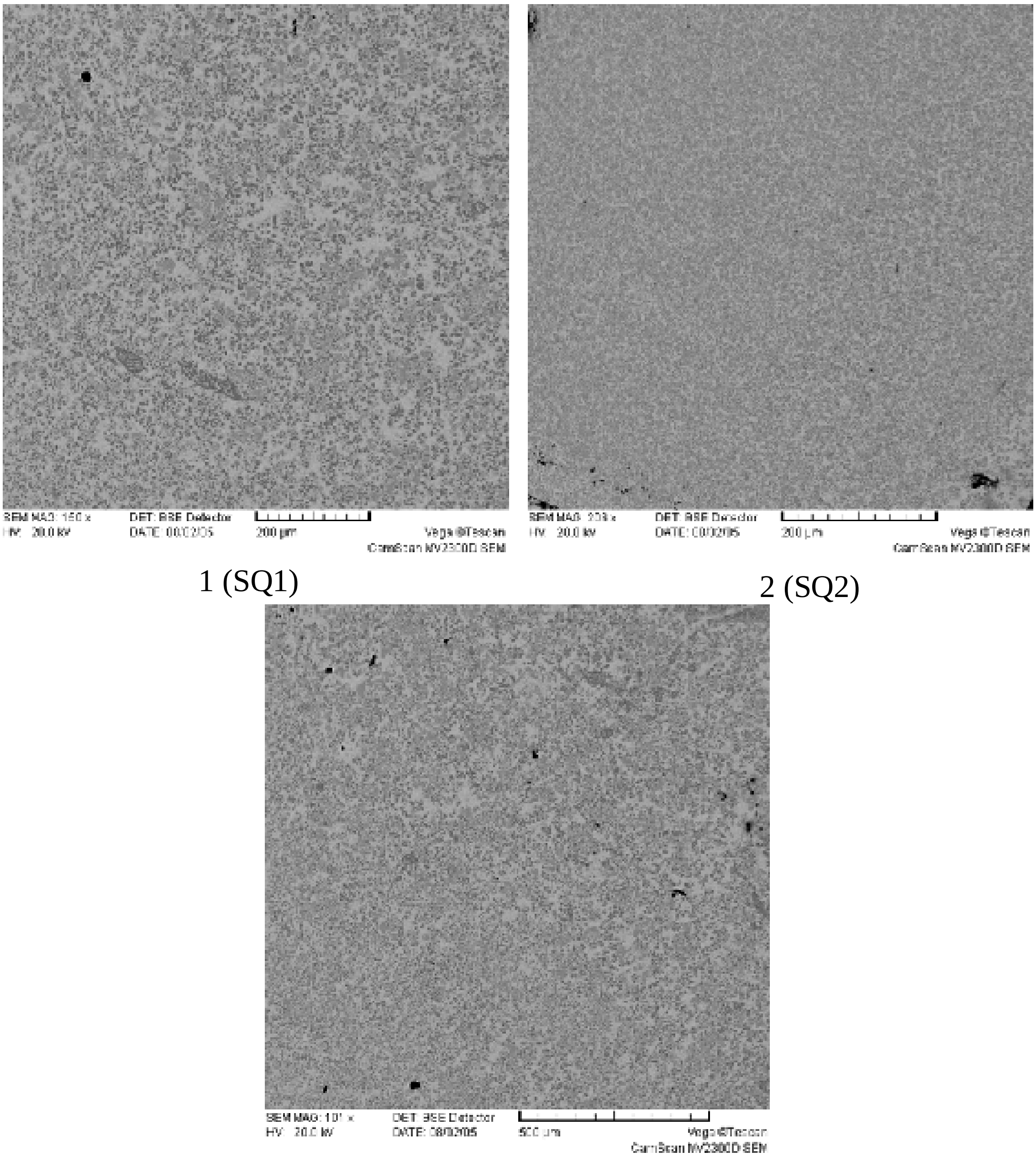

1 (SQ1)

2 (SQ2)

3 (SQ3)

Fig. 3.49. Micrographs of sample No.2-1 from CORD39

Table 3.41. EDX data for sample No.2-1

No.		Zr	Fe	O
SQ1	mass %	65.81	26.18	8.01
	mol.%	42.67	27.73	29.60
	mol.% MeO_x	60.62	39.38	
SQ2	mass %	64.90	25.48	9.62
	mol.%	40.22	25.79	33.99
	mol.% MeO_x	60.93	39.07	
SQ3	mass %	65.17	26.05	8.79
	mol.%	41.29	26.96	31.74
	mol.% MeO_x	60.50	39.50	

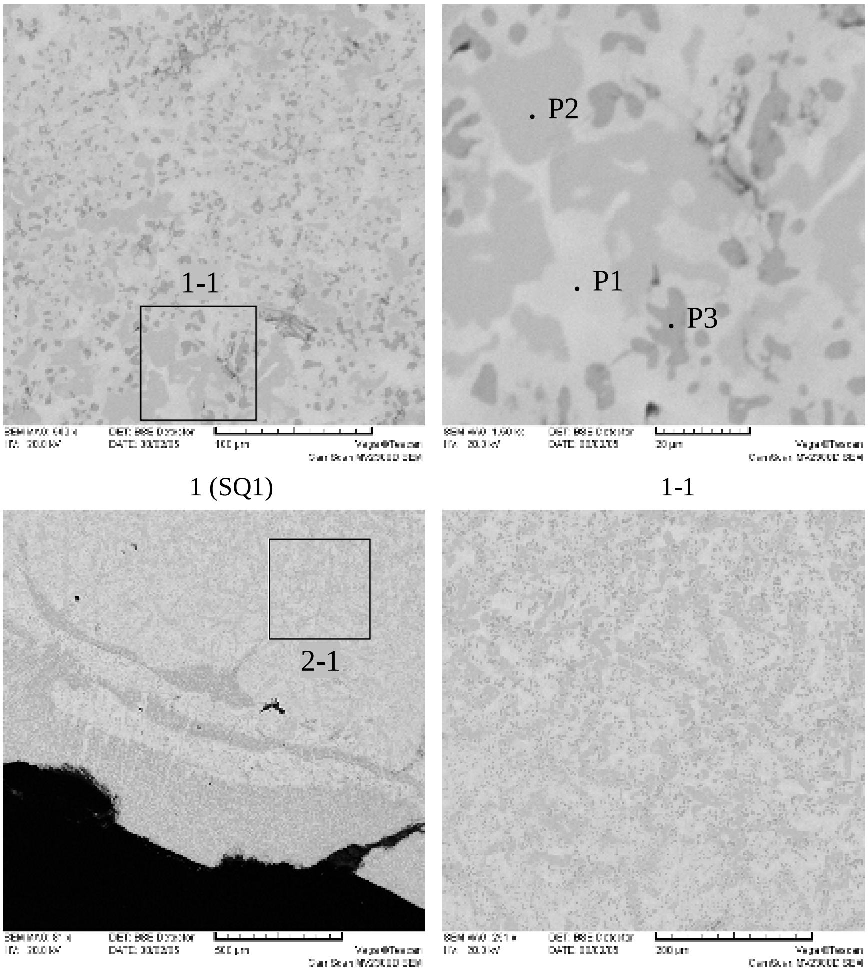

1 (SQ1) 1-1

2 2-1 (SQ2)

Fig. 3.50. Micrographs of sample No.2-2 from CORD39

Table 3.42. EDX data for sample No.2-2

No.		Zr	Fe	O
SQ1	mass %	59.56	32.07	8.38
	mol.%	37.29	32.80	29.91
	mol.% MeO_x	53.21	46.79	
SQ2	mass %	61.73	31.00	7.27
	mol.%	40.13	32.92	26.95
	mol.% MeO_x	54.94	45.06	
P1	mass %	66.13	27.22	6.66
	mol.%	44.52	29.93	25.55
	mol.% MeO_x	59.80	40.20	
P2	mass %	40.58	55.95	3.47
	mol.%	26.74	60.23	13.03
	mol.% MeO_x	30.74	69.26	
P3	mass %	73.18	1.08	25.74
	mol.%	33.01	0.8	66.19
	mol.% MeO_x	97.63	2.37	

After crystallization, the ingot was cut along the axis and a template was produced from one half (Fig. 3.51). The results of SEM/EDX analysis of the examined regions are presented in Figs. 3.52–3.55 and in Tabs. 3.43–3.46. Unlike in CORD33, the oxide-rich part was at the ingot top. It should be mentioned that like in CORD33, the boundary between the oxidic and metallic parts could be detected only after polishing. Microstructure of the oxide-rich top part of the ingot is dispersed and heterogeneous (Fig. 3.52); it confirms the high rate of melt crystallization. The primary crystallization phase is ZrO_{2-x} (Point P2 Fig. 3.52, Tab. 3.43), which dissociates at cooling into ZrO_2 and α-Zr(O) (small white inclusions in the ZrO_2 matrix). The second phase (Point P1 Fig. 3.52, Tab. 3.43), has apparently resulted from the secondary separation during melt cooling.

Microstructure of the metal-rich part of the ingot is more complicated. Regions 2, 4, 6 (Figs. 3.53–3.55) contain secondary oxide-rich isolates which apparently form at cooling of the metal-rich liquid. In regions 2, 5, 6 (Figs. 3.53–3.55) attention is drawn to the ~ 1 mm thick refractory phase (ZrO_2) that had crystallized on the crucible sections. The ZrO_2 matrix contains iron-rich inclusions. Due to the absence of standards, fuzziness of interphase boundaries and lack of contrast, phase composition of the metal-rich liquid is difficult to identify. Perhaps, the primary crystallization phase is ZrO_{2-x}. Its quantity should be small (Fig. 3.53, Tab. 3.44 Point P5). Then the Zr_6Fe_3O-based and $ZrFe_2(O)$-based phases crystallize (Points P3 and P4, Fig. 3.53, Tab. 3.44).

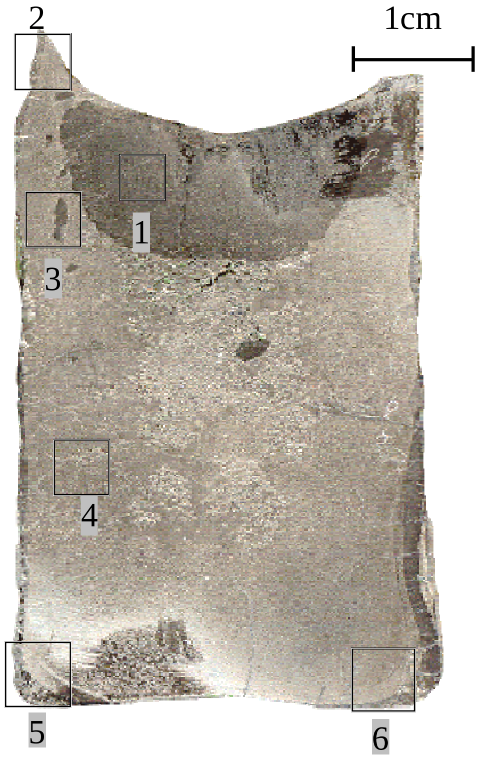

Fig. 3.51. Axial cut of the ingot from CORD39 (cooled from ~2520°C) with regions marked for SEM/EDX analysis

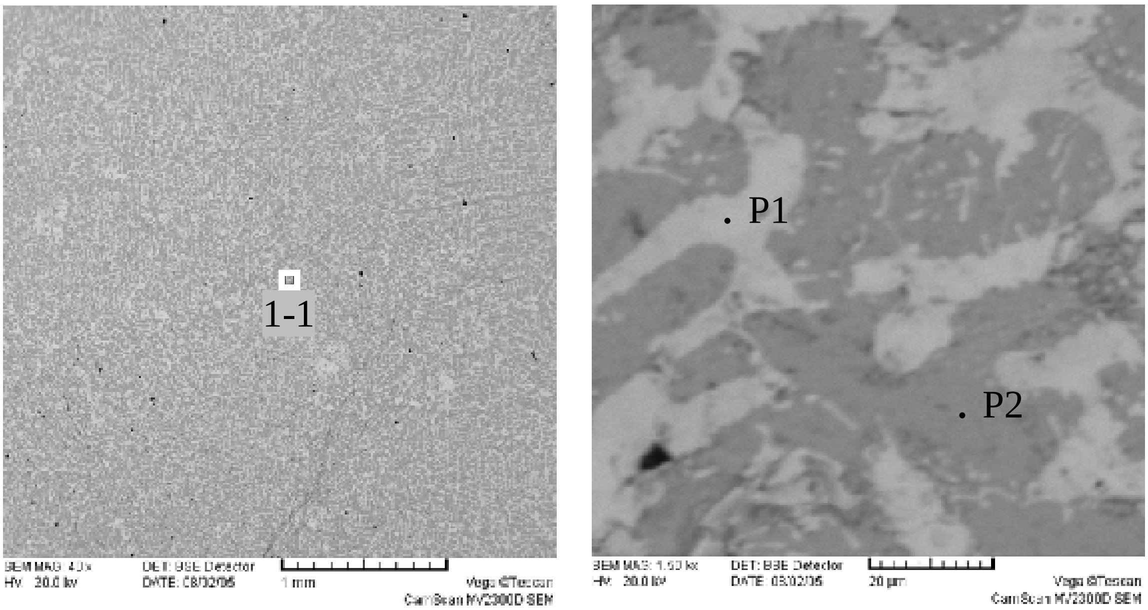

1 (SQ1) 1-1

Fig. 3.52. Micrographs of region 1 in the ingot from CORD39

Table 3.43. EDX data for region 1

No.		**Zr**	**Fe**	**O**
SQ1	mass %	73.64	7.26	19.11
	mol.%	37.87	6.10	56.03
	mol.% MeO$_x$	86.14	13.86	
P1	mass %	67.28	26.08	6.64
	mol.%	45.54	28.83	25.63
	mol.% MeO$_x$	61.23	38.77	
P2	mass %	75.95	-	24.05
	mol.%	35.64	-	64.36
	mol.% MeO$_x$	100	-	

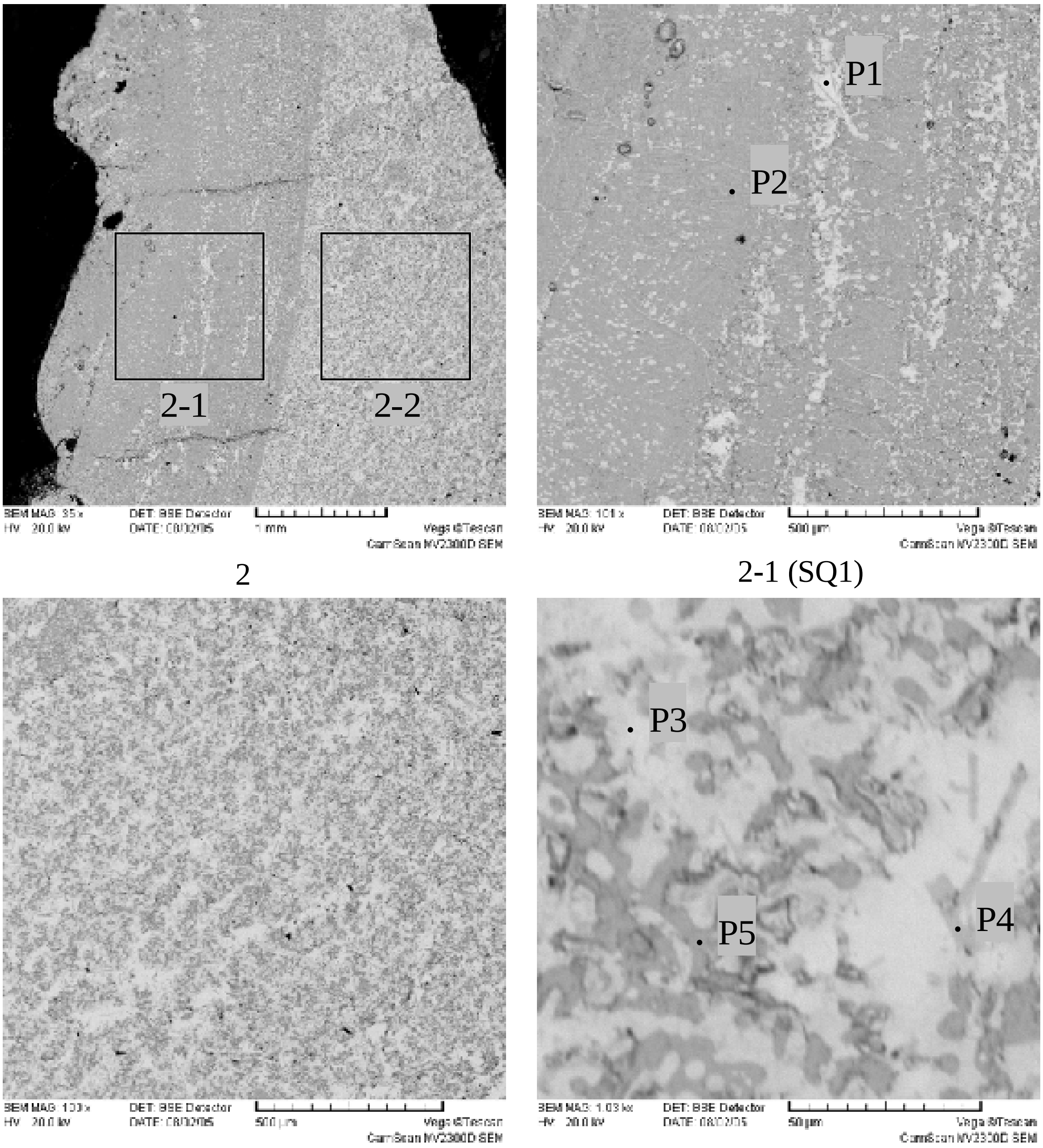

2 2-1 (SQ1)

2-2 (SQ2) 2-2-1

Fig. 3.53. Micrographs of region 2 in the ingot from CORD39

Table 3.44. EDX data for region 2

No.		Zr	Fe	O
SQ1	mass %	70.83	8.38	20.78
	mol.%	34.89	6.75	58.36
	mol.% MeO_x	83.8	16.2	
SQ2	mass %	64.47	25.03	10.5
	mol.%	39.02	24.74	36.23
	mol.% MeO_x	61.20	38.80	
P1	mass %	77.16	17.49	5.35
	mol.%	56.64	20.98	22.38
	mol.% MeO_x	72.97	27.03	
P2	mass %	74.95	-	25.05

	mol.%	34.42	-	65.58
	mol.% MeO_x	100	-	
P3	mass %	73.78	21.4	4.81
	mol.%	54.18	25.67	20.15
	mol.% MeO_x	67.85	32.15	
P4	mass %	40.99	54.12	4.89
	mol.%	26.06	56.2	17.73
	mol.% MeO_x	31.69	68.31	
P5	mass %	74.74	0.67	24.59
	mol.%	34.59	0.51	64.9
	mol.% MeO_x	98.55	1.45	

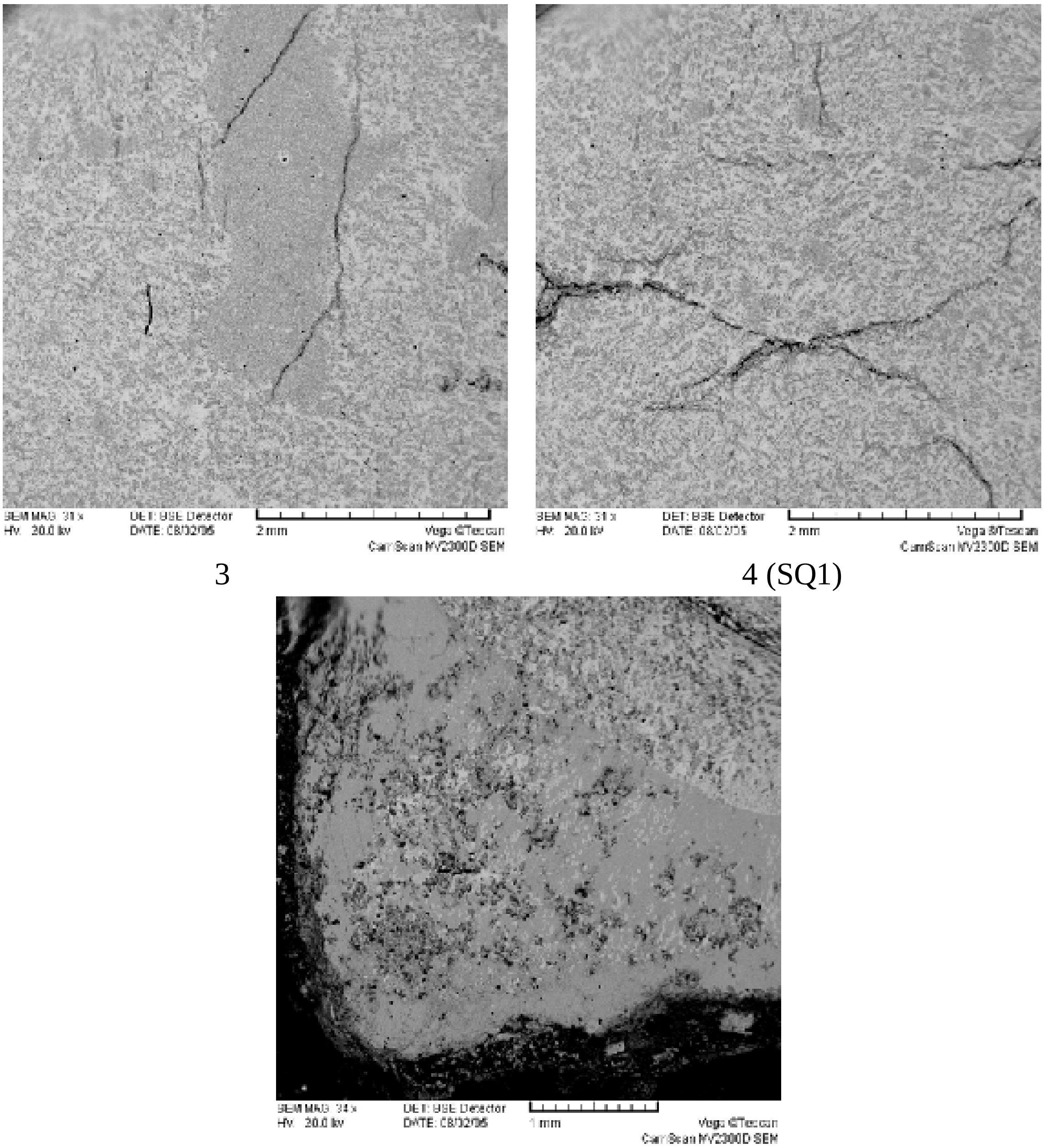

3 4 (SQ1)

5

Fig. 3.54. Micrographs of regions 3-5 in the ingot from CORD39

Table 3.45. EDX data for region 4

No.		Zr	Fe	O
SQ1	mass %	62.31	25.54	12.15
	mol.%	35.96	24.07	39.97
	mol.% MeO_x	59.90	40.10	

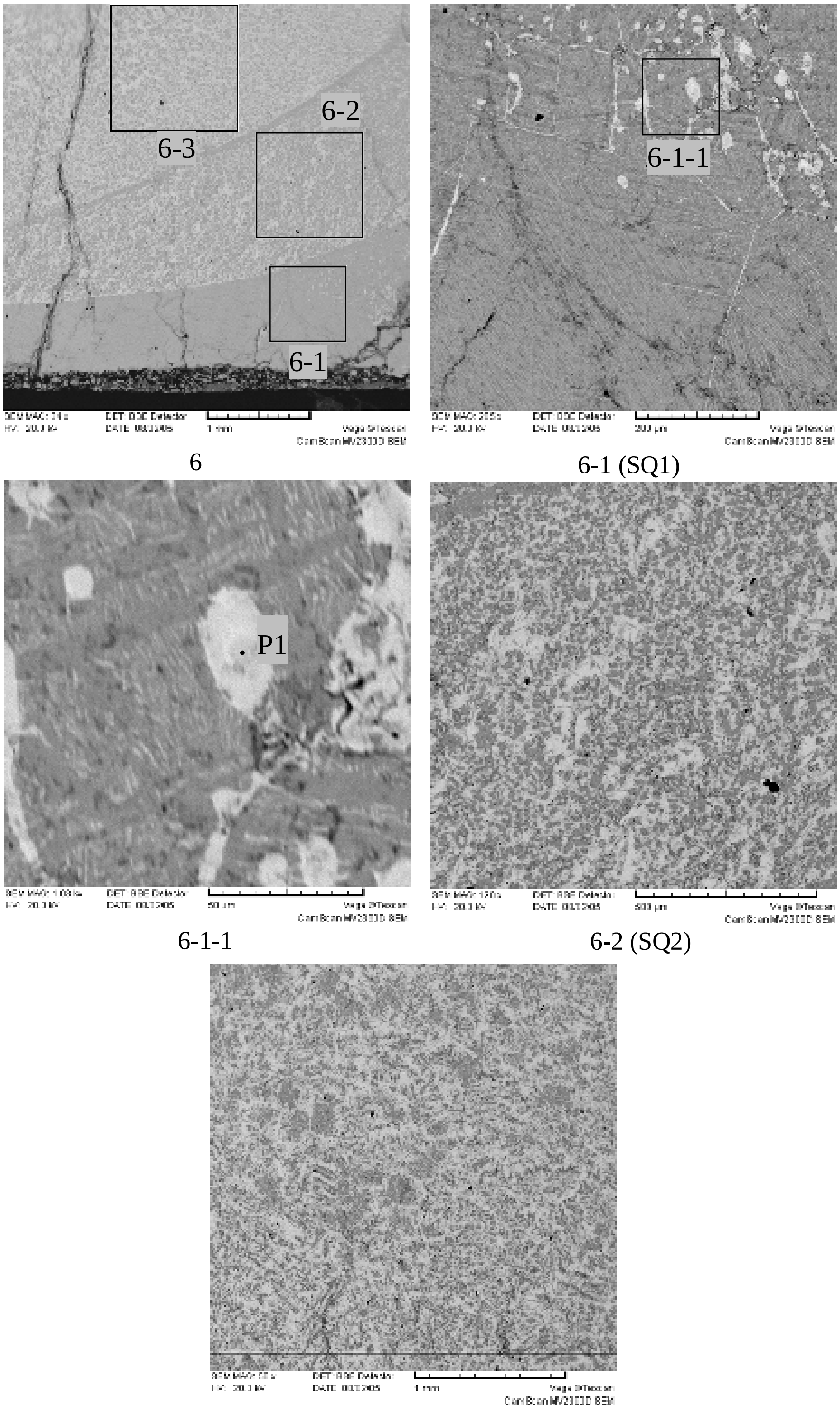

6 6-1 (SQ1)

6-1-1 6-2 (SQ2)

6-3 (SQ3)

Fig. 3.55. Micrographs of region 6 in the ingot from CORD39

Table 3.46. EDX data for region 6

No.		Zr	Fe	O
SQ1	mass %	73.79	1.89	24.32
	mol.%	34.24	1.44	64.33
	mol.% MeO_x	95.97	4.03	
SQ2	mass %	64.20	20.82	14.98
	mol.%	34.97	18.52	46.52
	mol.% MeO_x	65.38	34.62	
SQ3	mass %	63.46	25.57	10.97
	mol.%	37.82	24.89	37.28
	mol.% MeO_x	60.31	39.69	
P1	mass %	69.21	27.31	3.48
	mol.%	51.79	33.38	14.84
	mol.% MeO_x	60.81	39.19	

CORD44

Two rod samples were taken during the test. The results of SEM/EDX analysis of the samples are given in Figs. 3.56–3.57 and in Tabs.3.47–3.48. Microstructurally, the samples are fine-grained, it being an evidence that sampling was done under quenching conditions. Phase composition of the samples is difficult to determine because of the fine-grain structure and fuzziness of the phase boundaries. Fig. 3.58 presents microstructure of the crust. The crust had formed during the production and shrinking of the molten pool. At the time of T_{liq} measurement, the crust was solid and was overhanging the melt surface. The crust shows a decreased content of iron (Tab. 3.41 Region SQ1) and round inclusions of ZrO_2 (Tab. 3.49 Point P1).

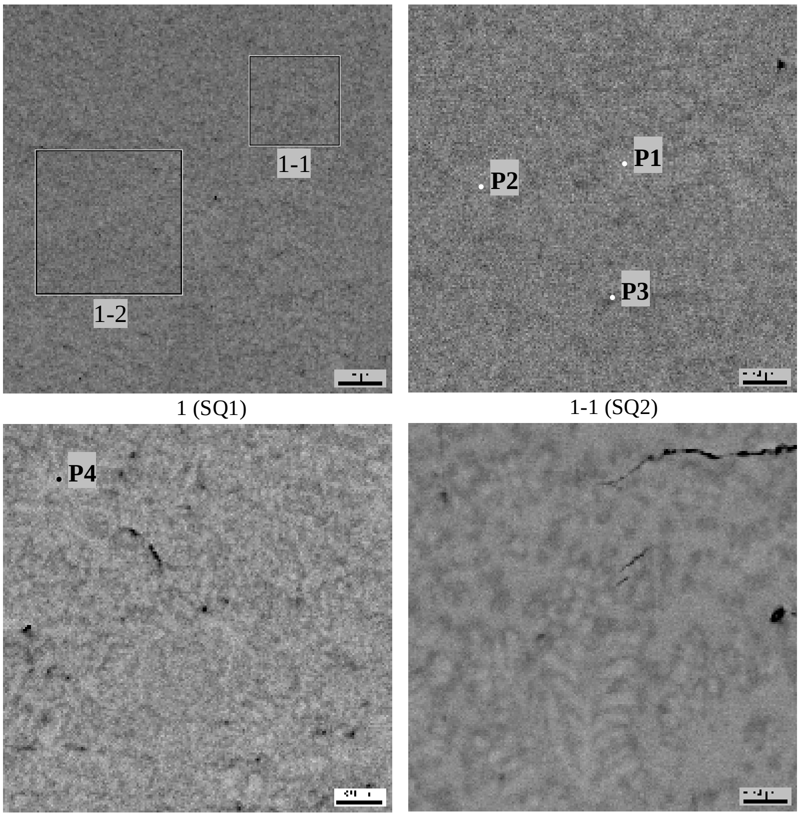

1 (SQ1) 1-1 (SQ2)

1-2 2 (SQ3)

Fig. 3.56. Micrographs of sample No.1 from CORD44 (1800°C)

Table 3.47. EDX data for sample No.1

No.		Zr	Fe	~O
SQ1	mass %	75.65	24.35	-
	mol.%	65.54	34.46	-
SQ2	mass %	75.17	24.37	0.46
	mol.%	63.93	33.86	2.21
	mol.% MeO_x	65.37	34.63	
SQ3	mass %	73.50	26.50	-
	mol.%	62.94	37.06	-
P1	mass %	69.45	30.55	-
	mol.%	58.19	41.81	-
P2	mass %	70.00	30.00	-
	mol.%	58.82	41.18	-
P3	mass %	72.22	27.78	-
	mol.%	61.42	38.58	-
P4	mass %	86.22	1.41	12.38
	mol.%	54.19	1.44	44.37
	mol.% MeO_x	97.41	2.59	

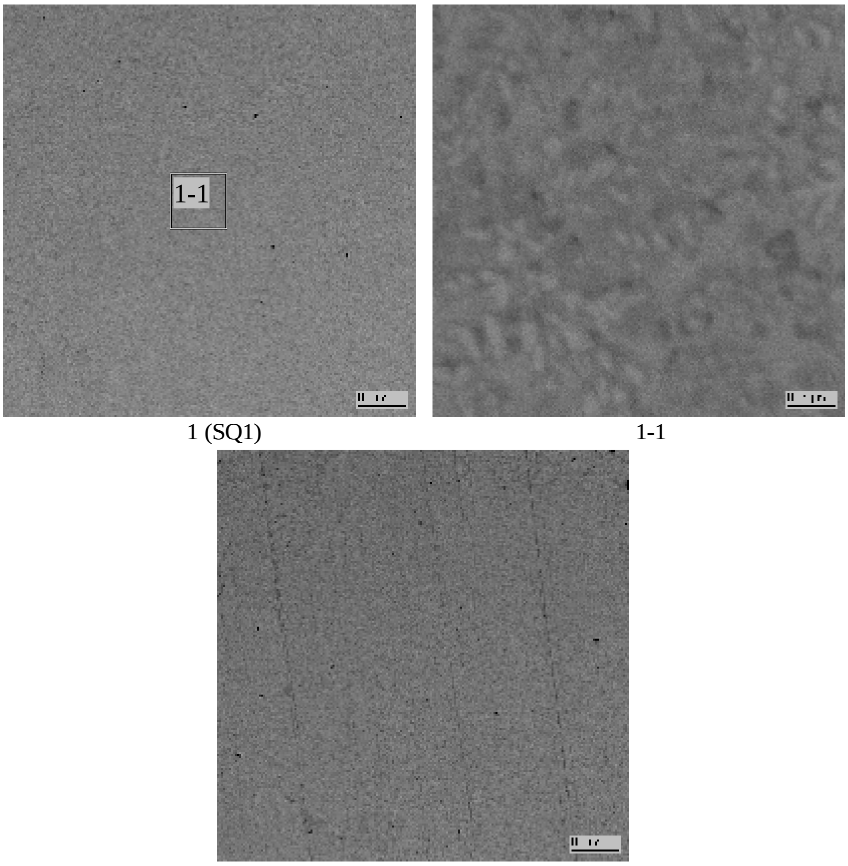

1 (SQ1)

1-1

2 (SQ2)

Fig. 3.57. Micrographs of sample No.2 from CORD44 (1820°C)

Table 3.48. EDX data for sample No.2

No.		Zr	Fe	~O
SQ1	mass %	75.39	24.14	0.46
	mol.%	64.18	33.57	2.25
	mol.% MeO$_x$	65.66	34.34	
SQ2	mass %	73.41	24.09	2.51
	mol.%	57.78	30.97	11.25
	mol.% MeO$_x$	65.11	34.89	

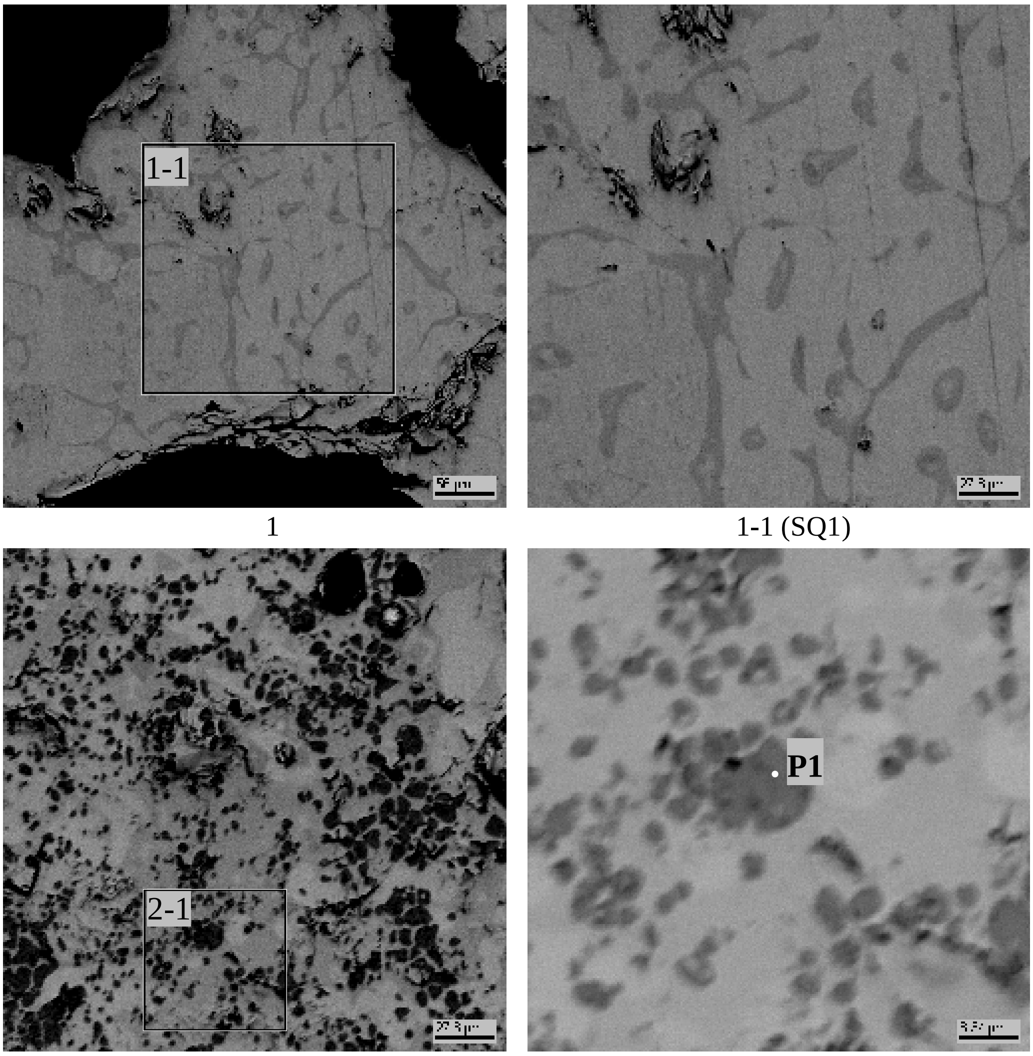

1 1-1 (SQ1)

2 (SQ2) 2-1

Fig. 3.58. Micrographs of the above-melt crust from CORD44

Table 3.49. EDX data for the above-melt crust

No.		Zr	Fe	~O
SQ1	mass %	83.20	5.41	11.39
	mol.%	53.00	5.63	41.37
	mol.% MeO_x	90.40	9.60	
SQ2	mass %	71.53	12.58	15.90
	mol.%	39.15	11.24	49.61
	mol.% MeO_x	77.69	22.31	
P1	mass %	63.60	0.45	35.95
	mol.%	23.62	0.27	76.11
	mol.% MeO_x	98.85	1.15	

After crystallization, the ingot was cut along the axis and a template was produced from one half (Fig. 3.59). The results of SEM/EDX analysis of the examined regions are presented in Figs. 3.60–3.69 and in Tabs. 3.50–3.56. Unusual crystallization with different microstructure inside and along periphery of the ingot was recorded. Inside, the ingot microstructure is uniform, with bulk composition that corresponds to that of the samples taken in the course of the test. The primary crystallization phase is apparently α-Zr(O) (Figs. 3.62, 3.65, Tabs. 3.51, 3.54 Point P1), while the secondary crystallization phases are intermetallides composed of $Zr_3Fe_2(O)$ in general. Noteworthy is high porosity which may be due to shrinking of the intermetallic phases and release of the dissolved gases during crystallization of the melt. Periphery of the ingot is depleted in iron and is rich in the refractory phase ZrO_2. Seemingly, a part of the refractory phase had crystallized on the cold crucible walls during the molten pool formation. At the time of T_{liq} measurement, the refractory phase remained solid and was surrounding the melt. Unusual crystallization in the ingot can also be observed, for instance in Region 5. At switching the HF heating off, a part of the above-melt crust broke into the cooling melt and dissolved in it. Probably, this caused a crystallization that differed from that at the molten pool bottom.

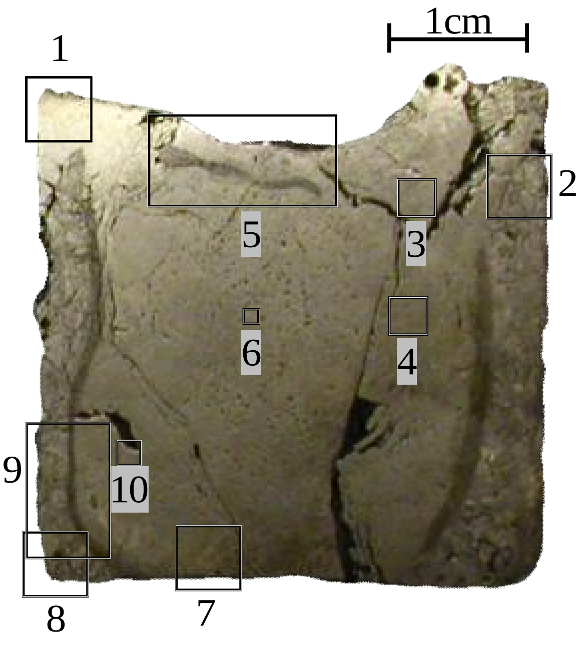

Fig. 3.59. Axial cut of the ingot from CORD44 (cooled from 1820°C) with regions marked for SEM/EDX examination

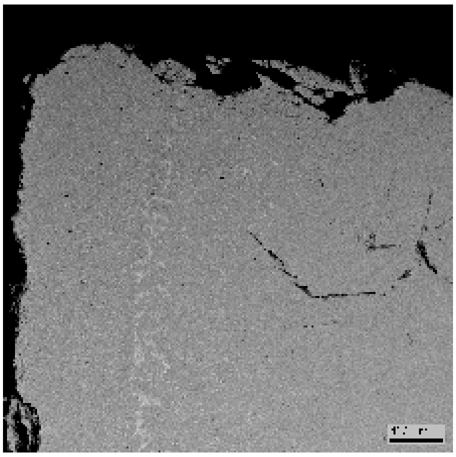

1

Fig. 3.60. Micrograph of region 1 in the ingot from CORD44

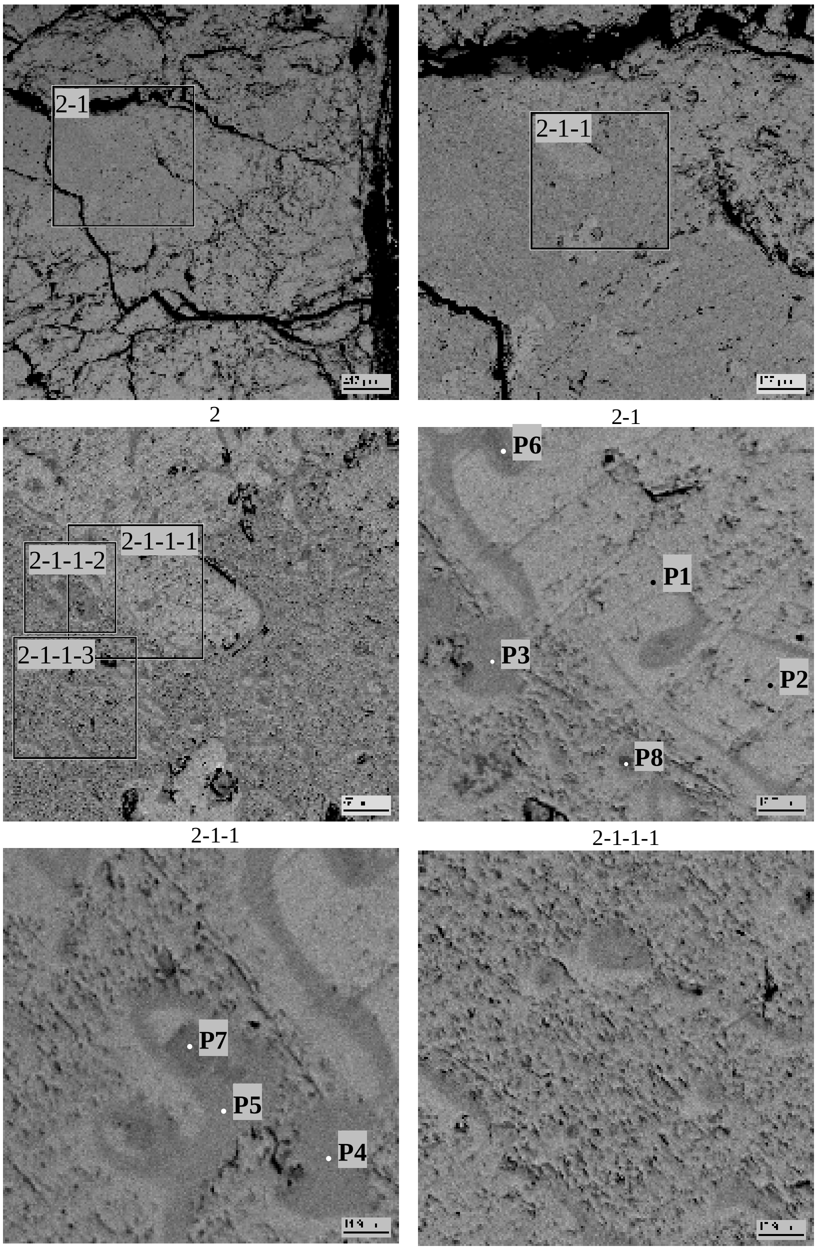

2

2-1

2-1-1

2-1-1-1

2-1-1-2

2-1-1-3 (SQ1)

Fig. 3.61. Micrographs of region 2 in the ingot from CORD44

Table 3.50. EDX data for region 2

No.		Zr	Fe	~O
SQ1	mass %	74.07	2.81	23.11
	mol.%	35.20	2.18	62.62
	mol.% MeO_x	94.16	5.84	
P1	mass %	73.65	0.29	26.06
	mol.%	33.07	0.21	66.71
	mol.% MeO_x	99.36	0.64	
P2	mass %	75.40	-	24.60
	mol.%	34.97	-	65.03
	mol.% MeO_x	100.0	-	
P3	mass %	60.13	27.42	12.46
	mol.%	34.18	25.46	40.37
	mol.% MeO_x	57.31	42.69	
P4	mass %	60.92	27.67	11.42
	mol.%	35.58	26.40	38.02
	mol.% MeO_x	57.41	42.59	
P5	mass %	62.66	27.56	9.79
	mol.%	38.33	27.54	34.13
	mol.% MeO_x	58.19	41.81	
P6	mass %	54.14	39.05	6.81
	mol.%	34.53	40.69	24.78
	mol.% MeO_x	45.91	54.09	
P7	mass %	53.84	39.53	6.62
	mol.%	34.48	41.35	24.18
	mol.% MeO_x	45.47	54.53	
P8	mass %	41.16	56.65	2.19
	mol.%	28.16	63.30	8.54
	mol.% MeO_x	30.79	69.21	

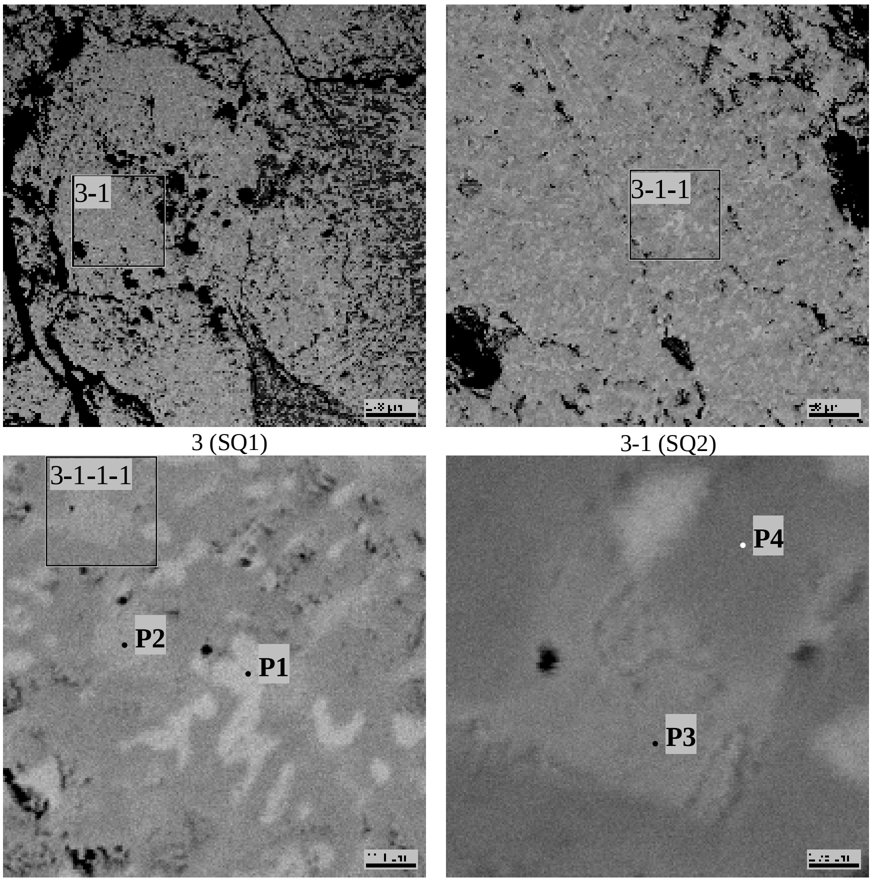

3 (SQ1) 3-1 (SQ2)

3-1-1 3-1-1-1

Fig. 3.62. Micrographs of region 3 in the ingot from CORD44

Table 3.51. EDX data for region 3

No.		Zr	Fe	~O
SQ1	mass %	57.90	17.07	25.03
	mol.%	25.34	12.20	62.46
	mol.% MeO_x	67.50	32.50	
SQ2	mass %	61.93	20.78	17.29
	mol.%	31.85	17.46	50.69
	mol.% MeO_x	64.59	35.41	
P1	mass %	79.66	0.55	19.79
	mol.%	41.19	0.46	58.35
	mol.% MeO_x	98.89	1.11	
P2	mass %	66.66	25.97	7.37
	mol.%	44.12	28.08	27.80
	mol.% MeO_x	61.11	38.89	
P3	mass %	66.57	26.27	7.16
	mol.%	44.29	28.55	27.16
	mol.% MeO_x	60.81	39.19	
P4	mass %	63.37	27.40	9.23
	mol.%	39.42	27.85	32.73
	mol.% MeO_x	58.60	41.40	

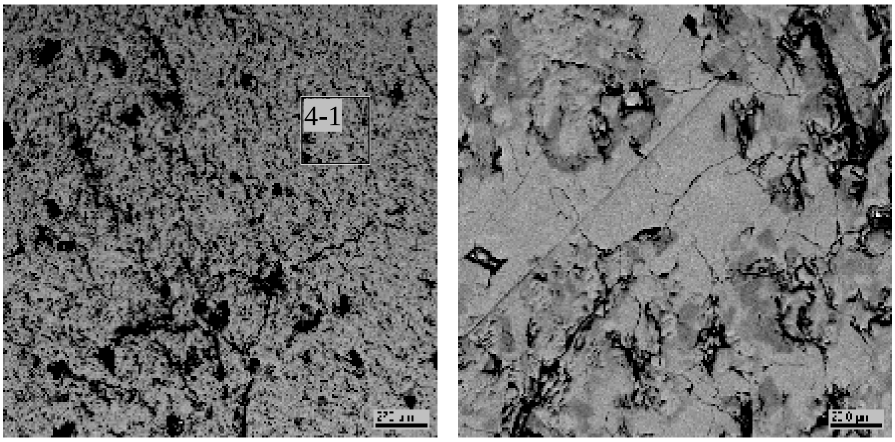

4 (SQ1) 4-1

Fig. 3.63. Micrographs of region 4 in the ingot from CORD44

Table 3.52. EDX data for region 4

No.		**Zr**	**Fe**	**~O**
SQ1	mass %	58.07	18.93	23.00
	mol.%	26.38	14.04	59.58
	mol.% MeO_x	65.26	34.74	

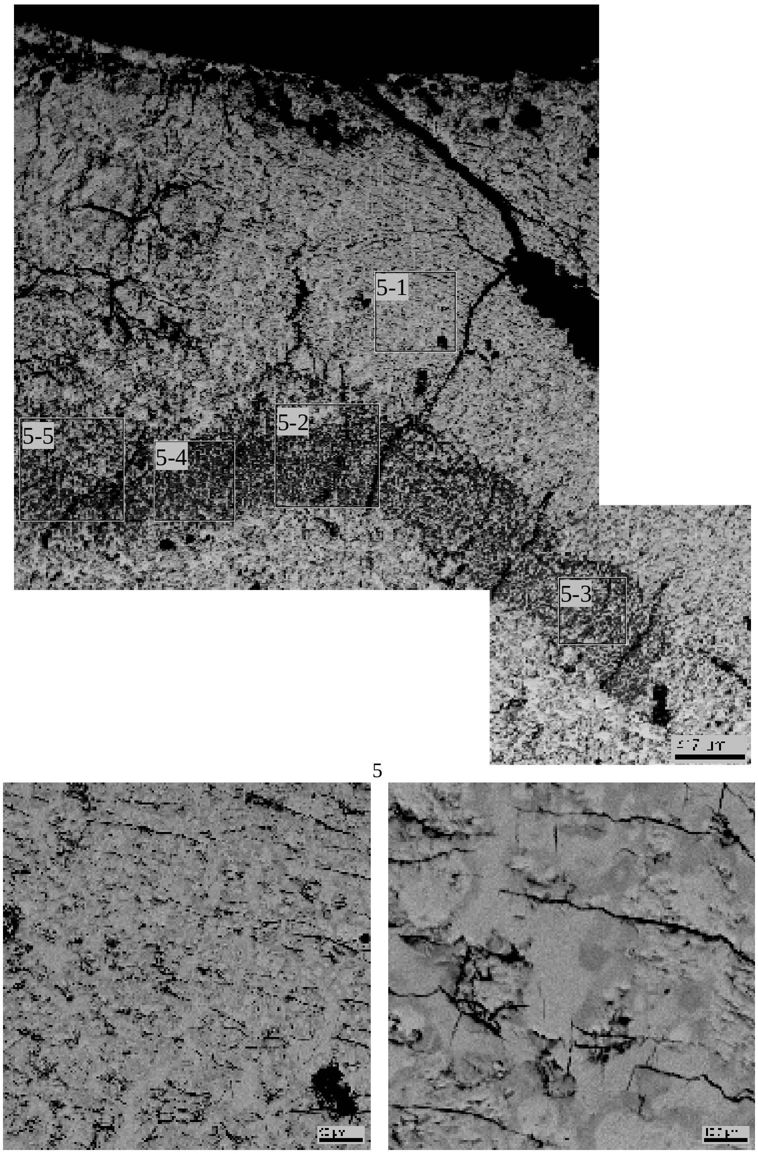

5

5-1 (SQ1) 5-1-1

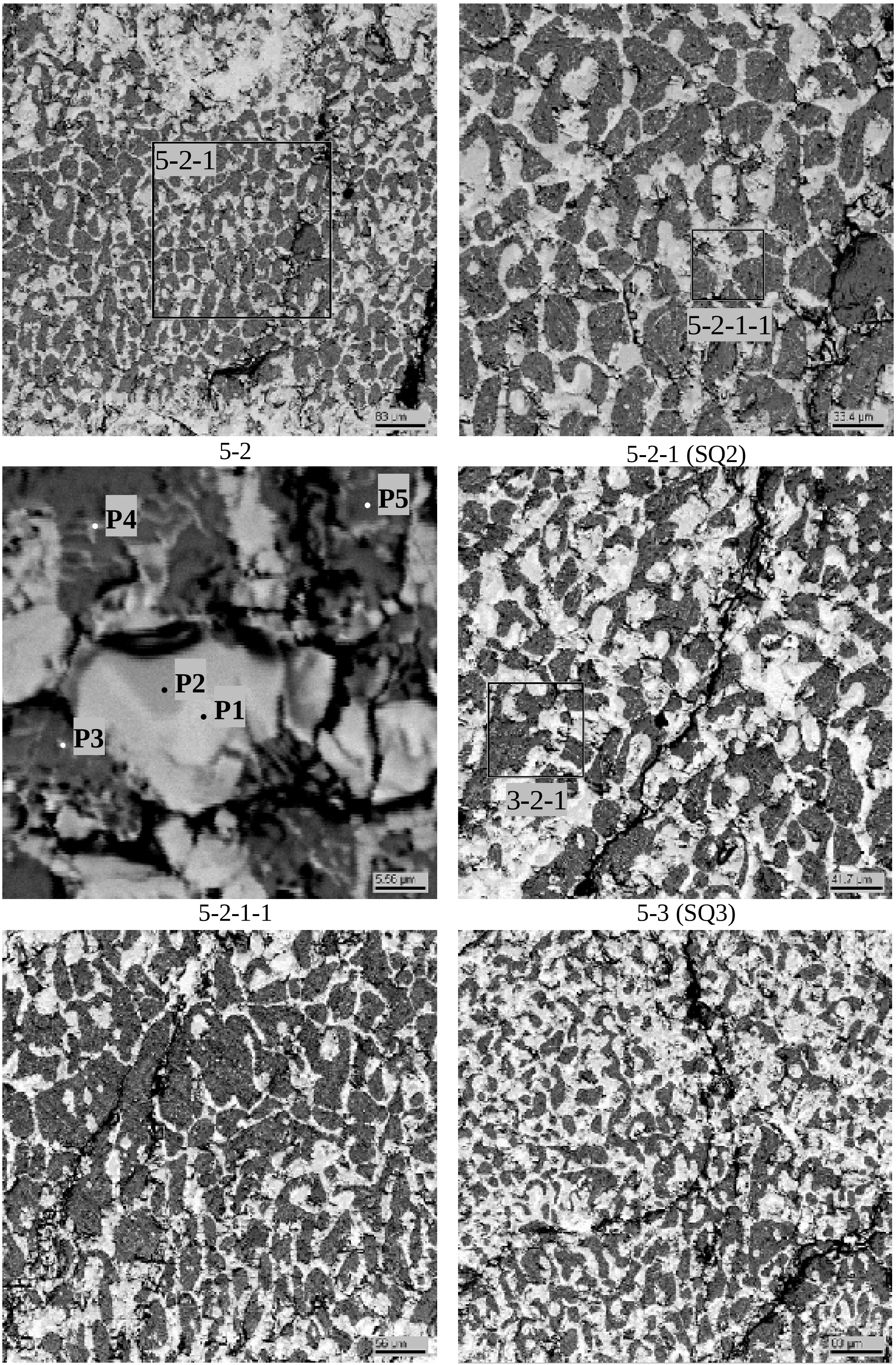

5-2

5-2-1 (SQ2)

5-2-1-1

5-3 (SQ3)

5-4 (SQ4)

5-5 (SQ5)

Fig. 3.64. Micrographs of region 5 in the ingot from CORD44

Table 3.53. EDX data for region 5

No.		**Zr**	**Fe**	**~O**
SQ1	mass %	67.12	19.48	13.40
	mol.%	38.27	18.15	43.58
	mol.% MeO_x	67.84	32.16	
SQ2	mass %	62.68	8.20	29.12
	mol.%	25.89	5.53	68.58
	mol.% MeO_x	82.40	17.60	
SQ3	mass %	63.27	10.26	26.47
	mol.%	27.40	7.25	65.35
	mol.% MeO_x	79.06	20.94	
SQ4	mass %	62.91	9.23	27.86
	mol.%	26.57	6.37	67.07
	mol.% MeO_x	80.67	19.33	
SQ5	mass %	62.81	12.45	24.74
	mol.%	28.01	9.07	62.92
	mol.% MeO_x	75.54	24.46	
P1	mass %	66.57	25.88	7.55
	mol.%	43.83	27.84	28.33
	mol.% MeO_x	61.16	38.84	
P2	mass %	56.09	40.88	3.03
	mol.%	40.03	47.66	12.31
	mol.% MeO_x	45.65	54.35	
P3	mass %	73.64	4.37	21.99
	mol.%	35.72	3.46	60.82
	mol.% MeO_x	91.17	8.83	
P4	mass %	61.48	3.76	34.76
	mol.%	23.13	2.31	74.56
	mol.% MeO_x	90.92	9.08	
P5	mass %	58.34	0.34	41.32
	mol.%	19.81	0.19	80.00
	mol.% MeO_x	99.07	0.93	

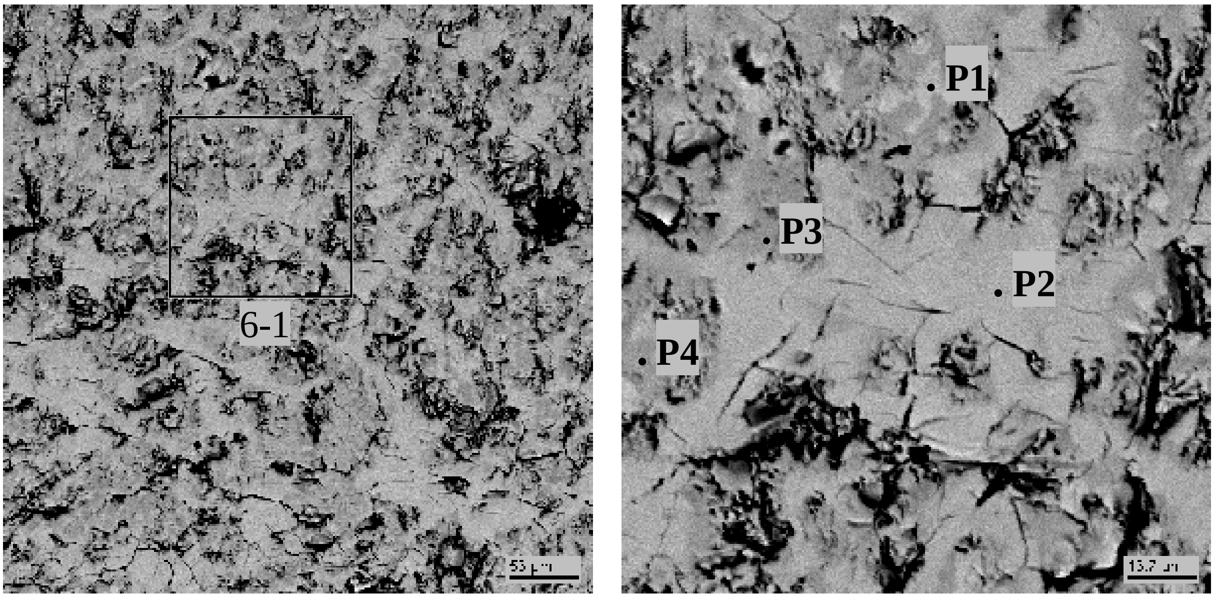

6 (SQ1) 6-1 (SQ2)

Fig. 3.65. Micrographs of region 6 in the ingot from CORD44

Table 3.54. EDX data for region 6

No.		**Zr**	**Fe**	**~O**
SQ1	mass %	64.88	21.64	13.47
	mol.%	36.64	19.97	43.39
	mol.% MeO_x	64.73	35.27	
SQ2	mass %	64.97	23.44	11.59
	mol.%	38.37	22.61	39.03
	mol.% MeO_x	62.92	37.08	
P1	mass %	79.16	0.93	19.92
	mol.%	40.75	0.78	58.47
	mol.% MeO_x	98.13	1.87	
P2	mass %	66.48	27.07	6.45
	mol.%	45.08	29.99	24.92
	mol.% MeO_x	60.05	39.95	
P3	mass %	63.56	27.71	8.73
	mol.%	40.08	28.54	31.38
	mol.% MeO_x	58.41	41.59	
P4	mass %	63.76	27.90	8.34
	mol.%	40.65	29.05	30.30
	mol.% MeO_x	58.32	41.68	

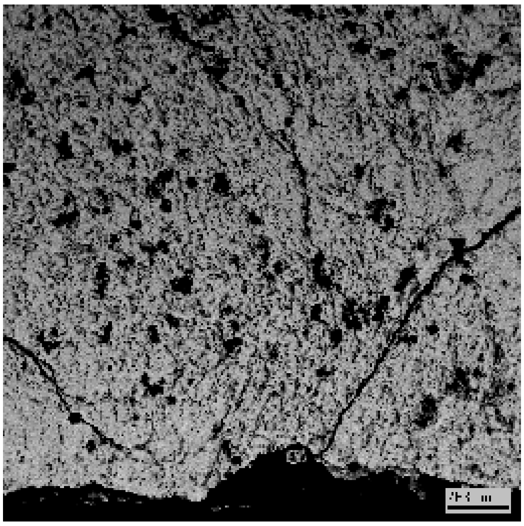

7 (SQ1)

Fig. 3.66. Micrograph of region 7 in the ingot from CORD44

Table 3.55. EDX data for region 7

No.		Zr	Fe	~O
SQ1	mass %	54.73	17.87	27.40
	mol.%	22.79	12.15	65.06
	mol.% MeO_x	65.22	34.78	

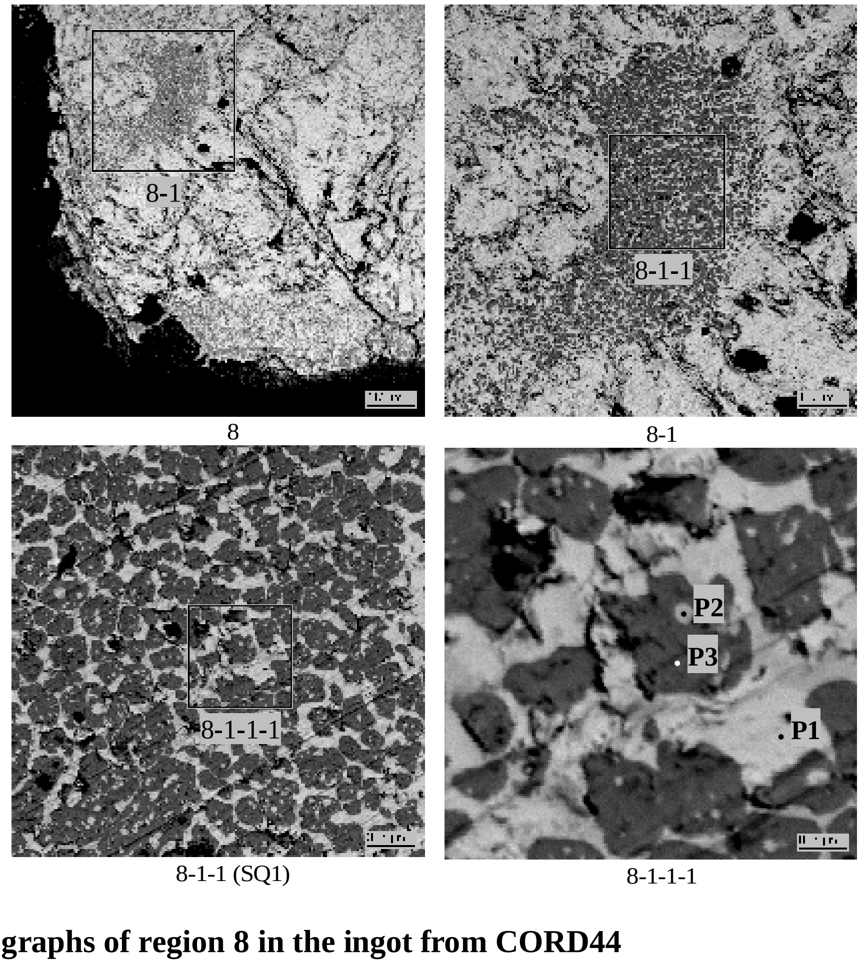

8 8-1

8-1-1 (SQ1) 8-1-1-1

Fig. 3.67. Micrographs of region 8 in the ingot from CORD44

Table 3.56. EDX data for region 8

No.		Zr	Fe	~O
SQ1	mass %	62.44	3.68	33.88
	mol.%	23.87	2.30	73.83
	mol.% MeO_x	91.21	8.79	
P1	mass %	63.96	27.91	8.13
	mol.%	41.02	29.23	29.74
	mol.% MeO_x	58.39	41.61	
P2	mass %	74.76	-	25.24
	mol.%	34.19	-	65.81
	mol.% MeO_x	100.0	-	
P3	mass %	58.64	-	41.36
	mol.%	19.91	-	80.09
	mol.% MeO_x	100.0	-	

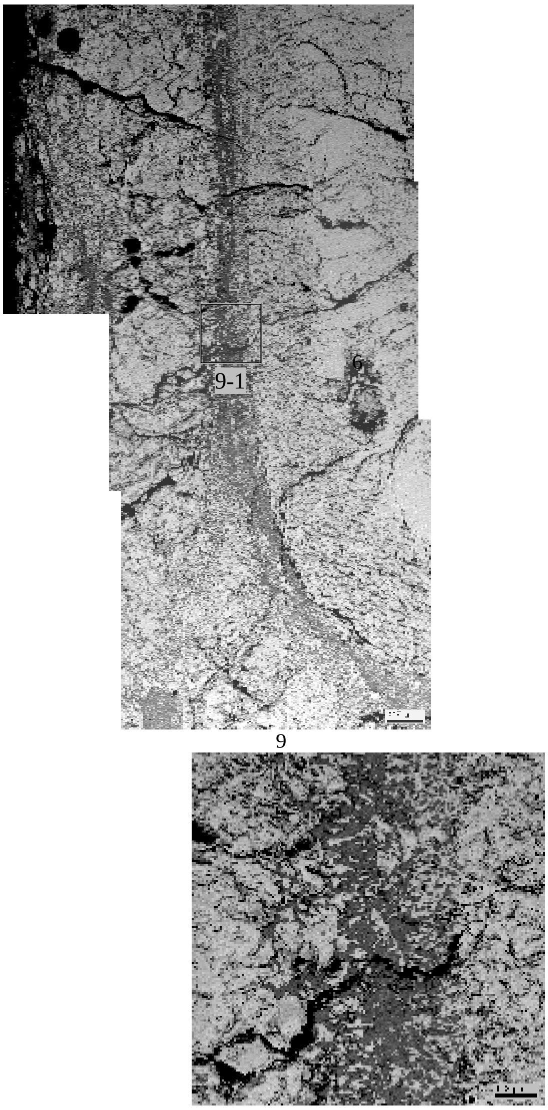

9

9-1

Fig. 3.68. Micrographs of region 9 in the ingot from CORD44

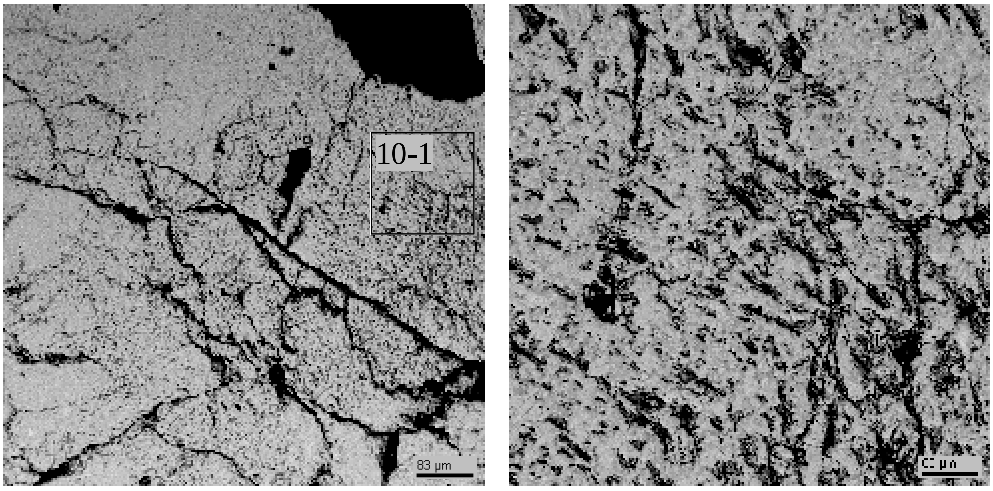

10 10-1

Fig. 3.69. Micrographs of region 10 in the ingot from CORD44

CORD45

Two rod samples were taken in the course of the test. The results of SEM/EDX analysis of rod samples are given in Figs. 3.70–3.71 and in Tabs. 3.57–3.58. Microstructure of the samples is composed by grains of the $ZrFe_3(O)$ phase (Fig. 3.70 Point P1), along the boundaries of which beads of metallic iron are located (Fig. 3.70 Point P2). Of special interest are spherical inclusions of ZrO_{2-x} with small content of iron (Fig. 3.70 Point P3). Their spherical shape indicates that they were liquid at the time of sampling and were quenched later. Thus, it may be supposed that the melt was within the miscibility gap.

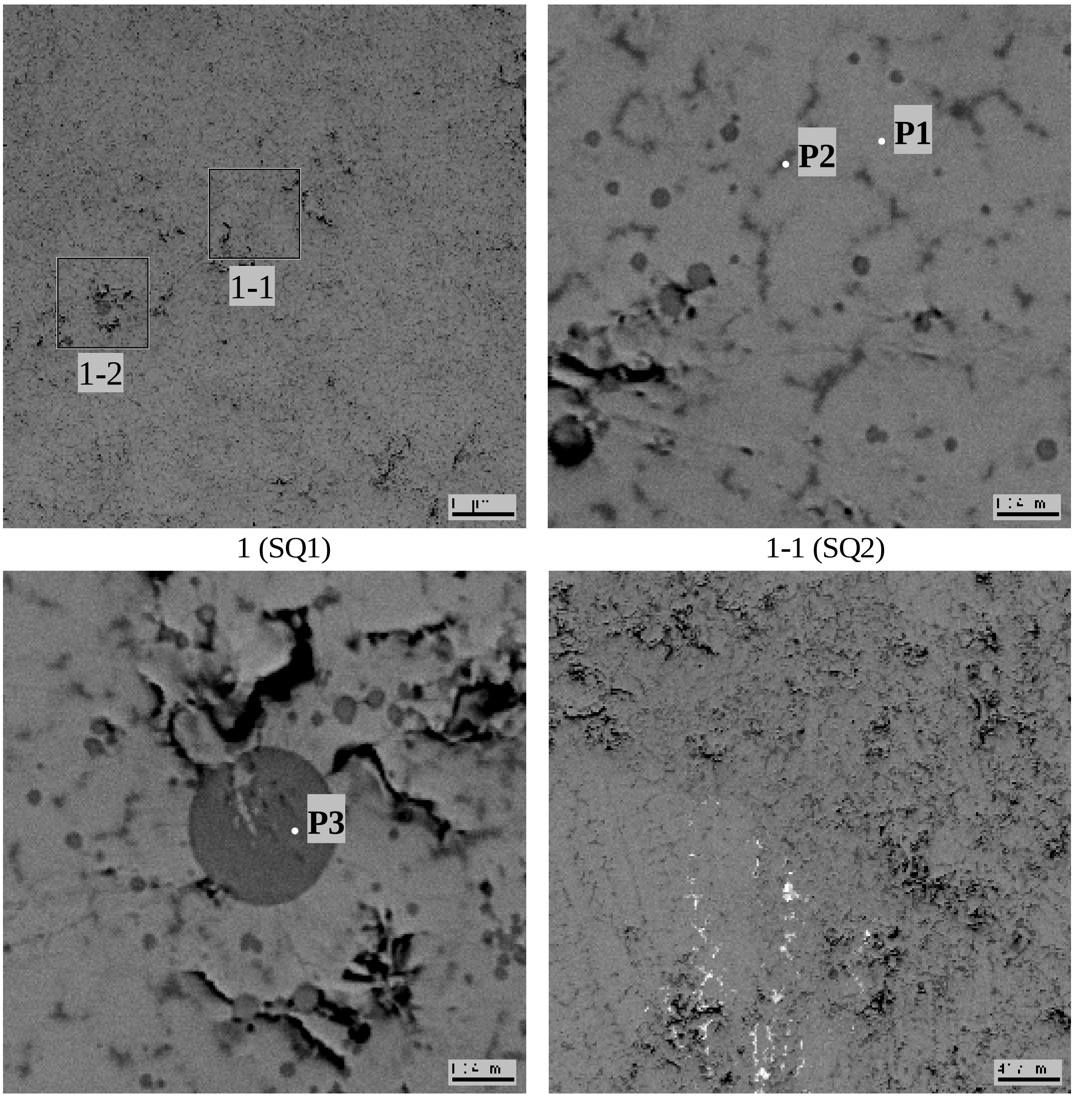

1 (SQ1) 1-1 (SQ2)

1-2 2 (SQ3)

Fig. 3.70. Micrographs of sample No.1 (T=2540°C) from CORD45

Table 3.57. EDX data for sample No.1

No.		Zr	Fe	O
SQ1	mass %	35.45	64.55	-
	mol.%	25.16	74.84	-
SQ2	mass %	35.84	64.16	-
	mol.%	25.48	74.52	-
SQ3	mass %	36.42	63.58	-
	mol.%	25.96	74.04	-
P1	mass %	36.40	63.60	-
	mol.%	25.95	74.05	-
P2	mass %	17.64	82.36	-
	mol.%	11.59	88.41	-
P3	mass %	63.08	6.19	30.74
	mol.%	25.39	4.07	70.54
	mol.% MeO_x	86.19	13.81	

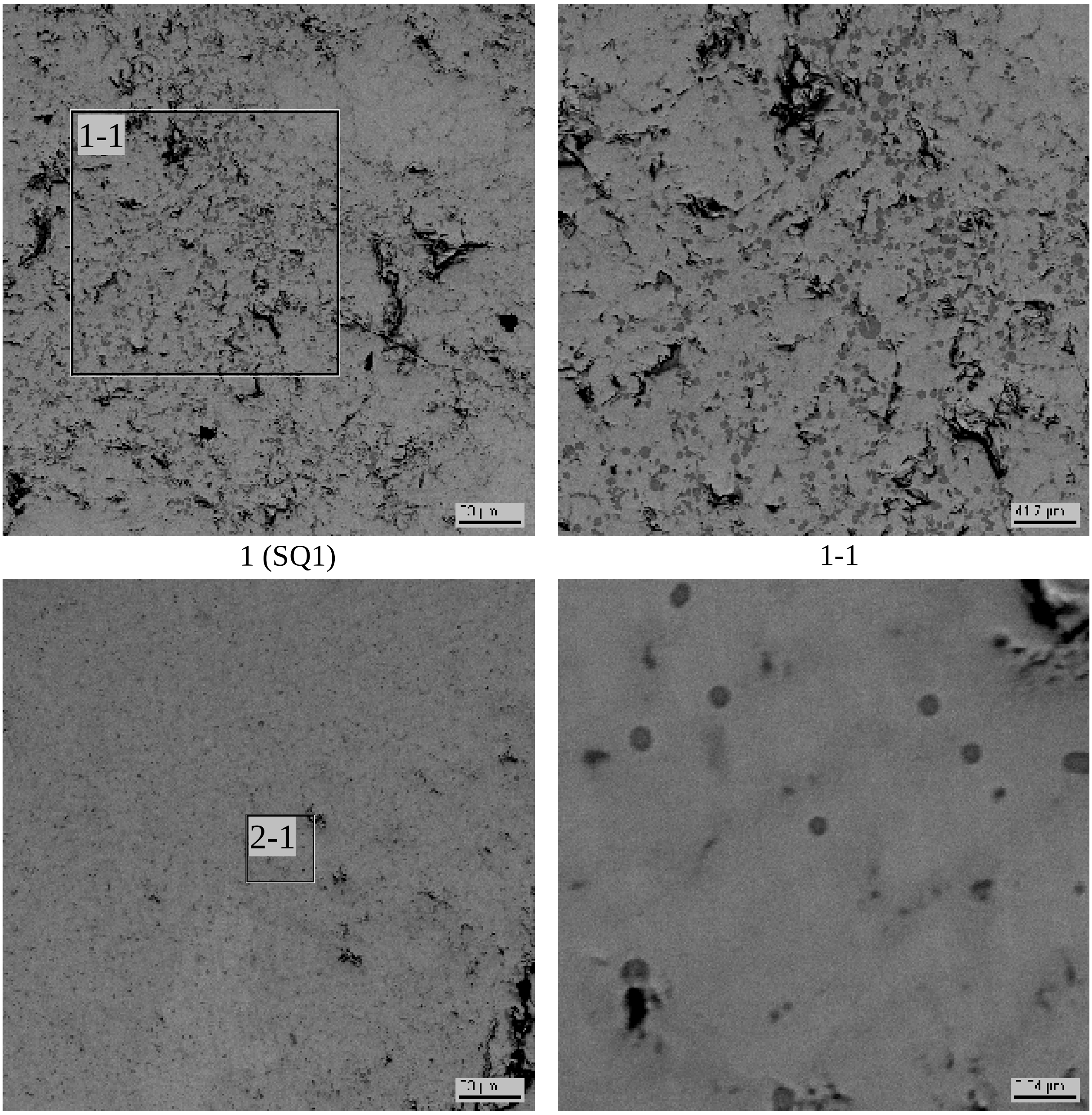

1 (SQ1) 1-1

2 (SQ2) 2-1

Fig. 3.71. Micrographs of sample No.2 (T=2600°C) from CORD45

Table 3.58. EDX data for sample No.2

No.		Zr	Fe	O
SQ1	mass %	37.48	62.52	-
	mol.%	26.84	73.16	-
SQ2	mass %	35.47	64.53	-
	mol.%	25.18	74.82	-

After crystallization, the ingot was cut along the axis and a template was produced from one half (Fig. 3.72). The results of SEM/EDX analysis of the examined regions are presented in Figs. 3.73–3.76 and in Tab. 3.50–3.56. The whole section of the ingot shows uniform microstructure, the analysis of which allows a conclusion about coexistence of three phases, that is $ZrFe_3(O)$, metallic iron and inclusions of $Zr(Fe)O_{2-x}$ (Fig. 3.73, Tab.3.59, Points P4, P6 and Fig.3.76, Tab. 3.62, Point P1). Besides, round formations of ZrO_2 are observed throughout the investigated volume of the ingot (2, 2-1, 4, 5-1), it being the evidence that here lies the miscibility gap boundary. In this case, the ZrO_2-based liquid is present in insignificant quantity and is spread throughout the volume as separate drops. Like in other tests, the refractory phase ZrO_2 crystallizes in the regions that adjoin the cooled crucible surfaces (Fig.3.73 Region 1-1, Tab. 3.59 Point P3). Thickness of the crust is approximately 0.5 mm.

Fig. 3.72. Axial cut of the ingot from CORD45 (cooled from 2540°C) with regions marked for SEM/EDX examination

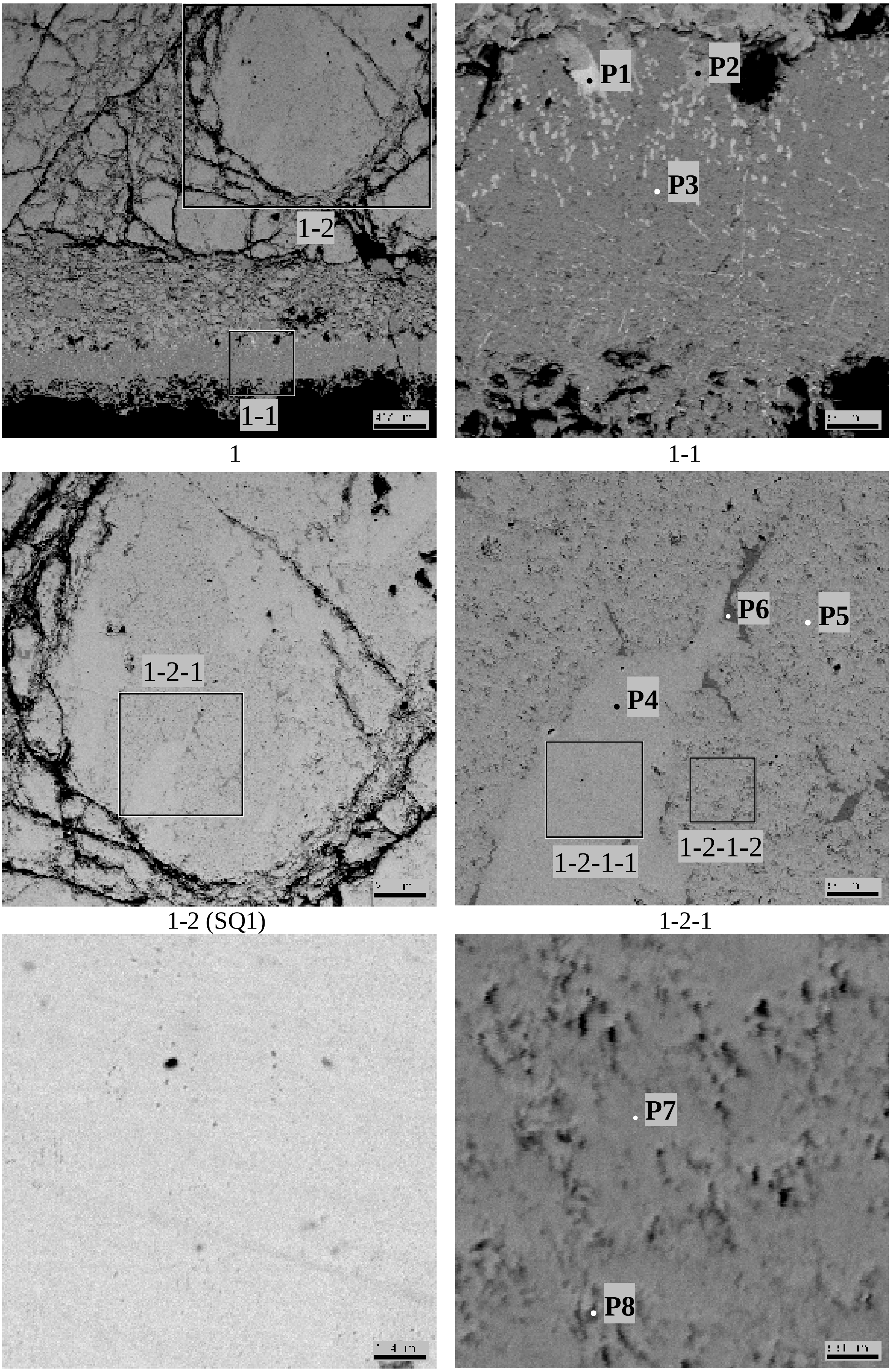

1 1-1

1-2 (SQ1) 1-2-1

1-2-1-1 (SQ2) 1-2-1-2 (SQ3)

Fig. 3.73. Micrographs of region 1 in the ingot from CORD45

Table 3.59. EDX data for region 1

No.		Zr	Fe	O
SQ1	mass %	35.88	64.12	-
	mol.%	25.51	74.49	-
SQ2	mass %	37.10	62.90	-
	mol.%	26.53	73.47	-
SQ3	mass %	37.10	62.90	-
	mol.%	26.53	73.47	-
P1	mass %	72.89	27.11	-
	mol.%	62.20	37.80	-
P2	mass %	39.36	60.64	-
	mol.%	28.44	71.56	-
P3	mass %	75.41	-	24.59
	mol.%	34.98	-	65.02
	mol.% MeO_x	100.0	-	
P4	mass %	37.20	62.80	-
	mol.%	26.61	73.39	-
P5	mass %	36.94	63.06	-
	mol.%	26.40	73.60	-
P6	mass %	10.87	89.13	-
	mol.%	6.95	93.05	-
P7	mass %	36.69	63.31	-
	mol.%	26.19	73.81	-
P8	mass %	35.22	64.78	-
	mol.%	24.97	75.03	-

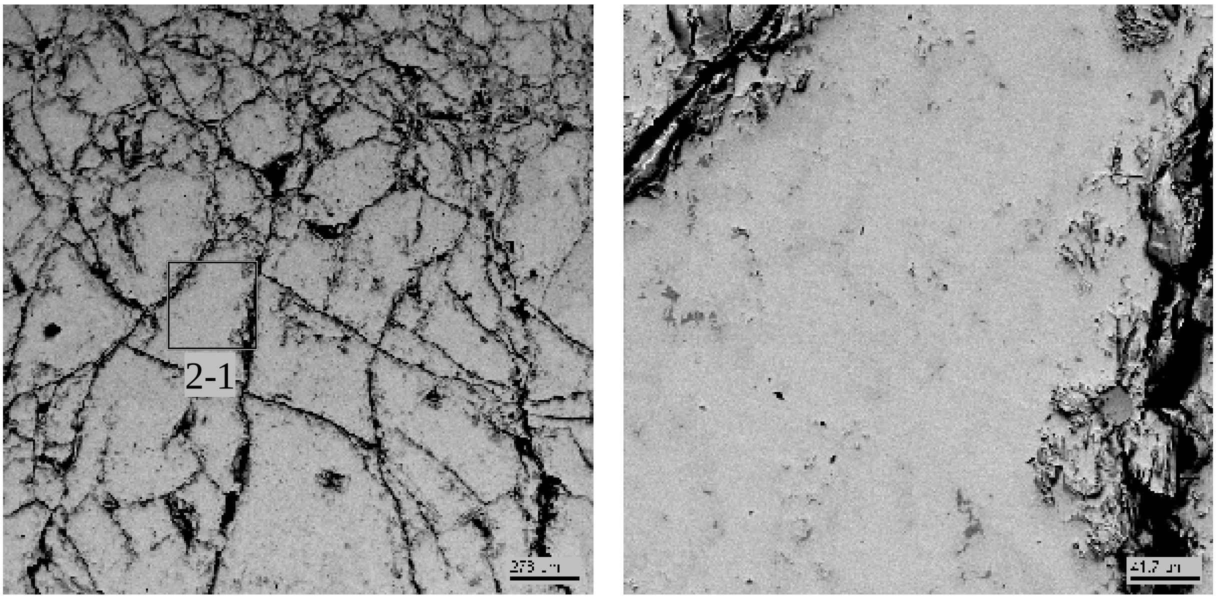

2 (SQ1) 2-1

Fig. 3.74. Micrographs of region 2 in the ingot from CORD45

Table 3.60. EDX data for region 2

No.		Zr	Fe	O
SQ1	mass %	36.54	63.46	-
	mol.%	26.06	73.94	-

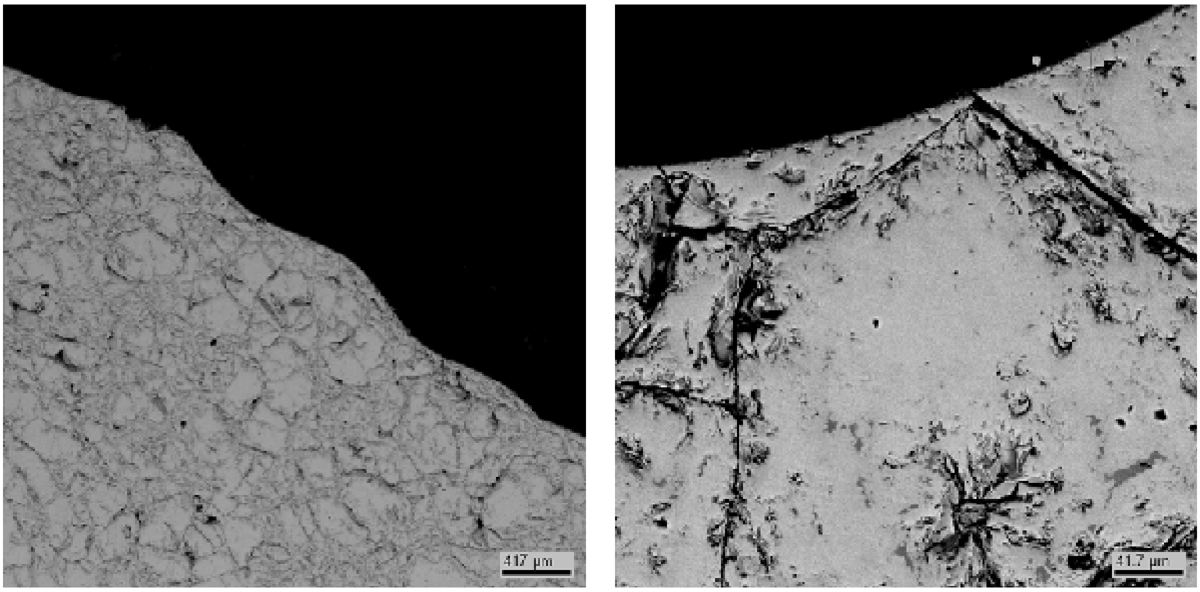

3 4

Fig. 3.75. Micrographs of regions 3-4 in the ingot from CORD45

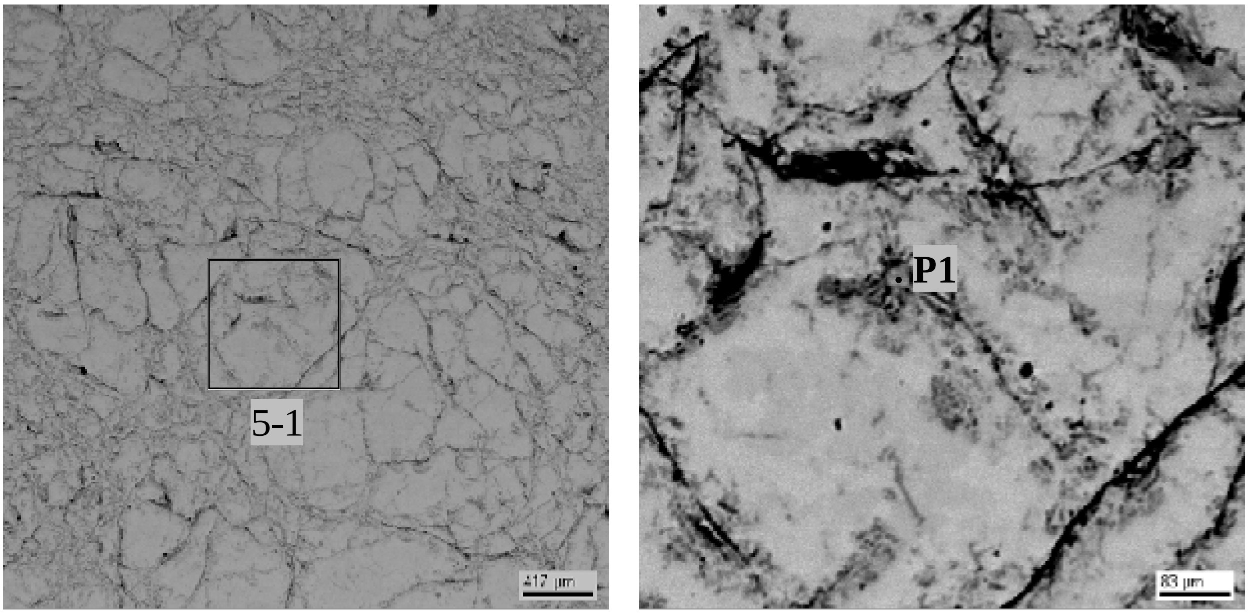

5 (SQ1) 5-1 (SQ2)

Fig. 3.76. Micrographs of region 5 in the ingot from CORD45

Table 3.62. EDX data for region 5

No.		Zr	Fe	O
SQ1	mass %	36.89	63.11	-
	mol.%	26.35	73.65	-
SQ2	mass %	35.48	64.52	-
	mol.%	25.19	74.81	-
P1	mass %	81.82	2.06	16.12
	mol.%	46.20	1.90	51.90
	mol.% MeO_x	96.05	3.95	

3.5. Visual polythermal analysis in the cold crucible (VPA IMCC).

Figs. 3.77–3.82 and Tabs. 3.63 contain the processed and generalized data from the CORD experimental series. The data were obtained from studies of the Zr-Fe-O system by means of VPA IMCC. The figures show fragments of thermograms with videoframes of the melt at the instant of T_{liq} measuring.

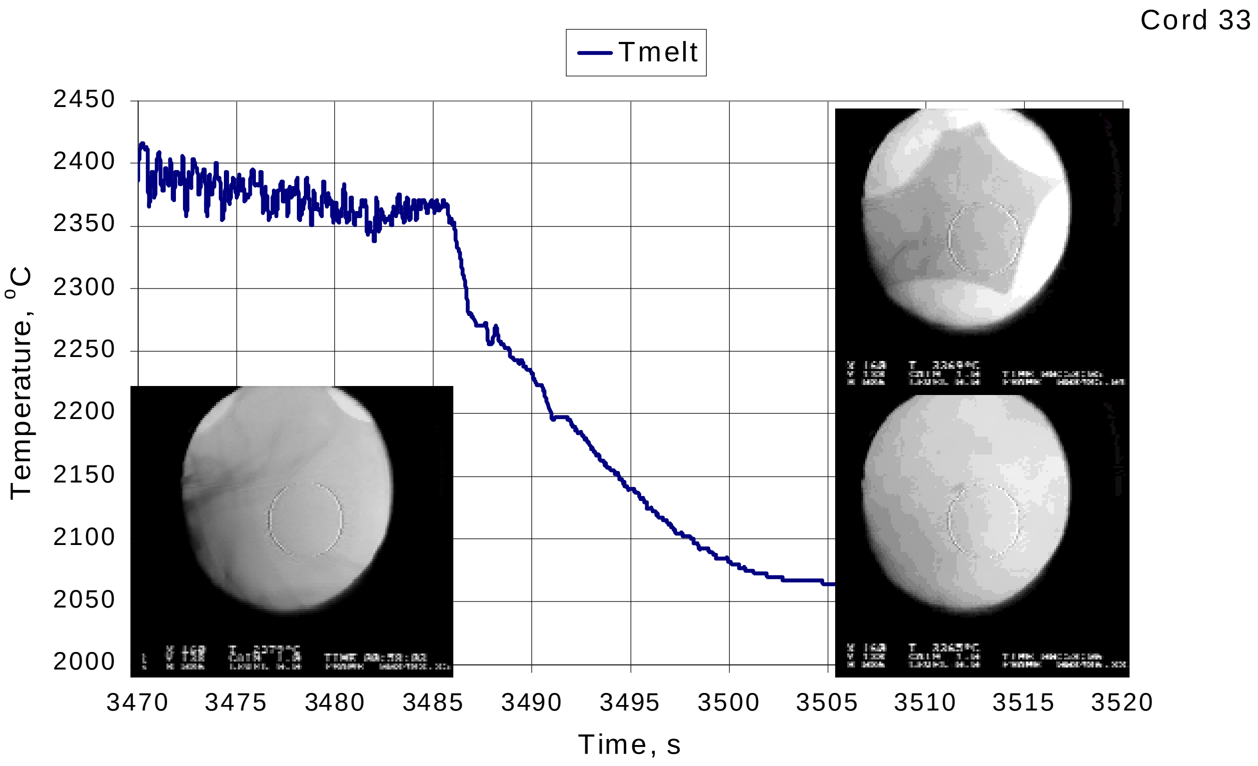

Fig. 3.77. Thermogram with the molten pool surface videoframes from CORD33

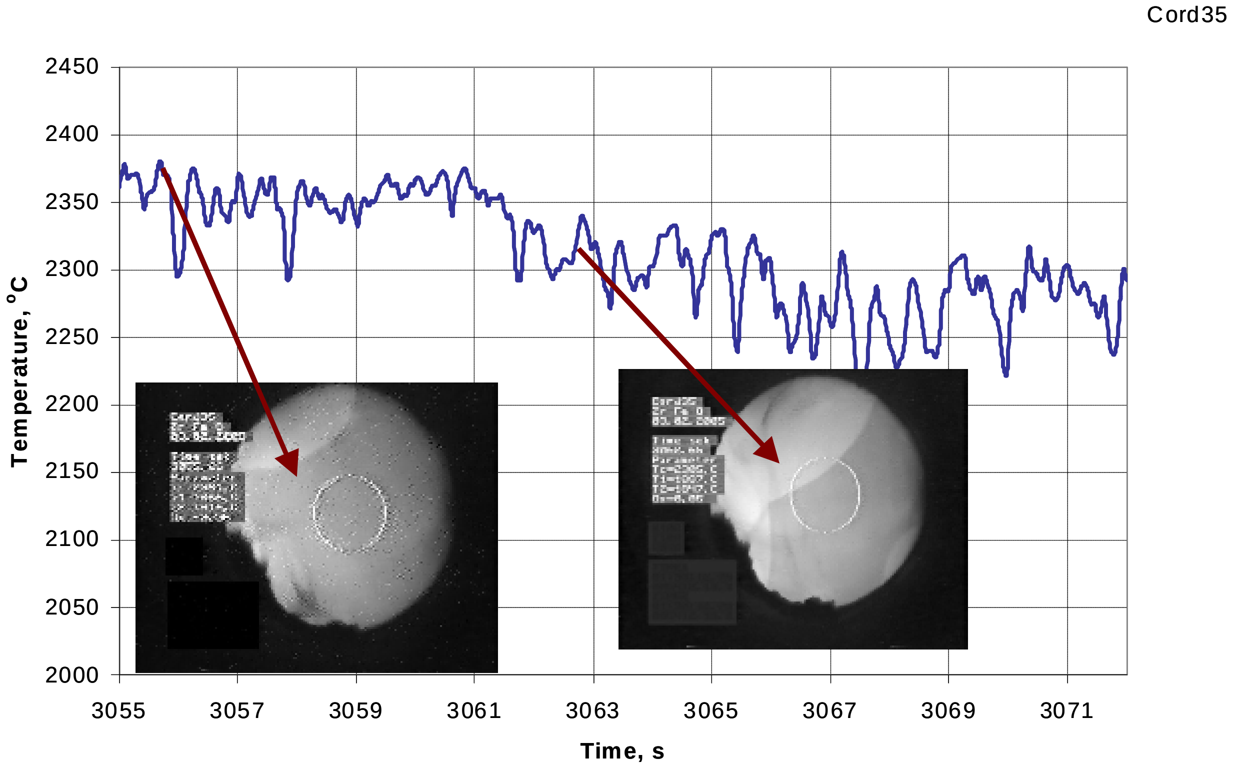

Fig. 3.78. Thermogram with the molten pool surface videoframes from CORD35 c (measurement made before crystallization of the refractory phase)

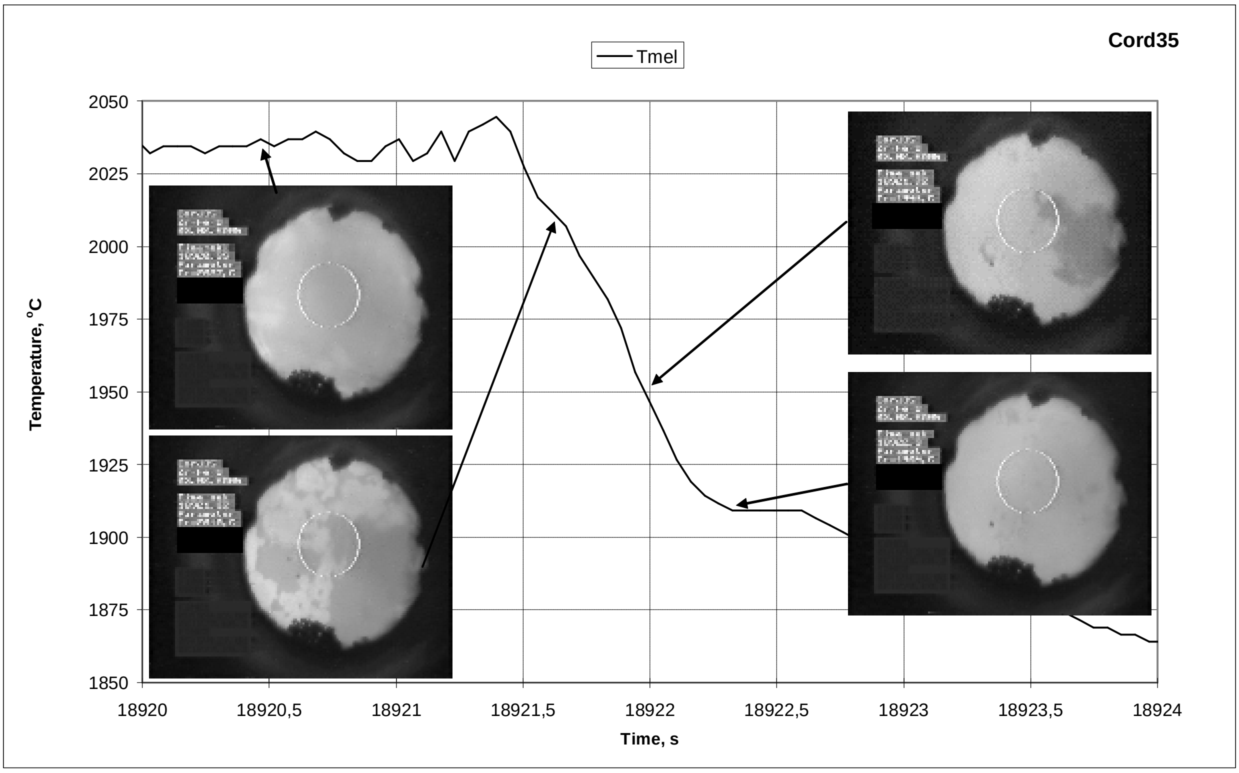

Fig. 3.79. Thermogram with the molten pool surface videoframes from CORD35 (measurement made after crystallization of the refractory phase)

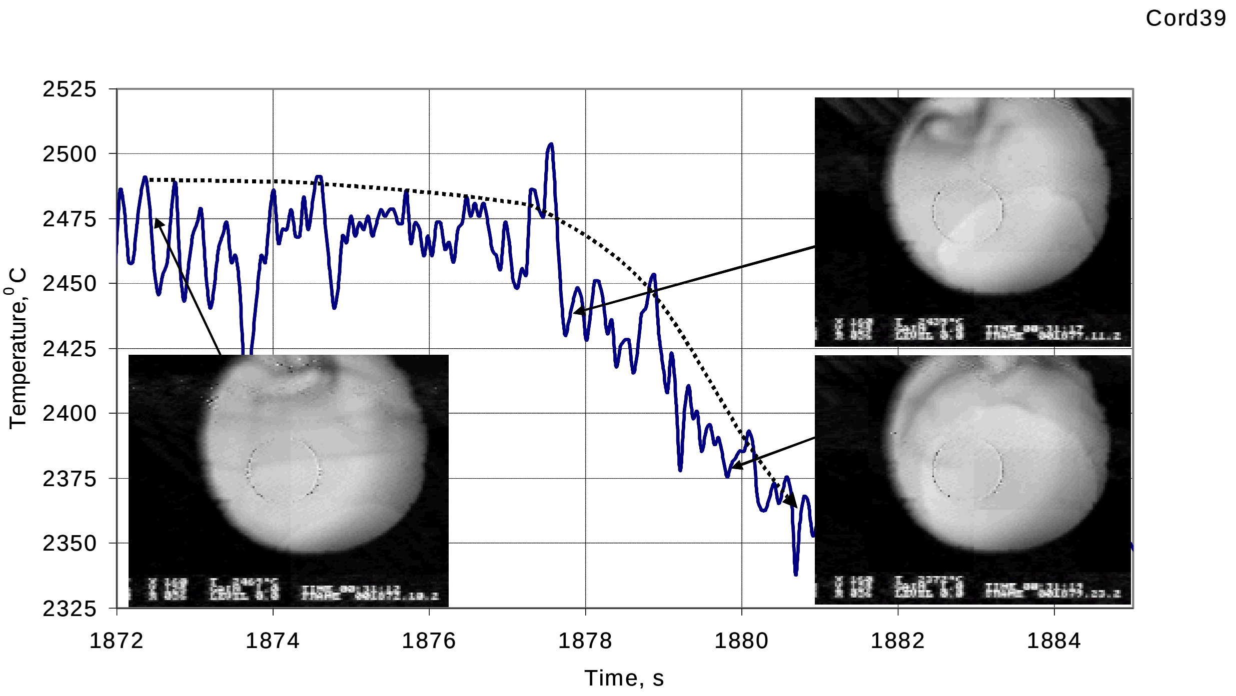

Fig. 3.80. Thermogram with the molten pool surface videoframes from CORD39

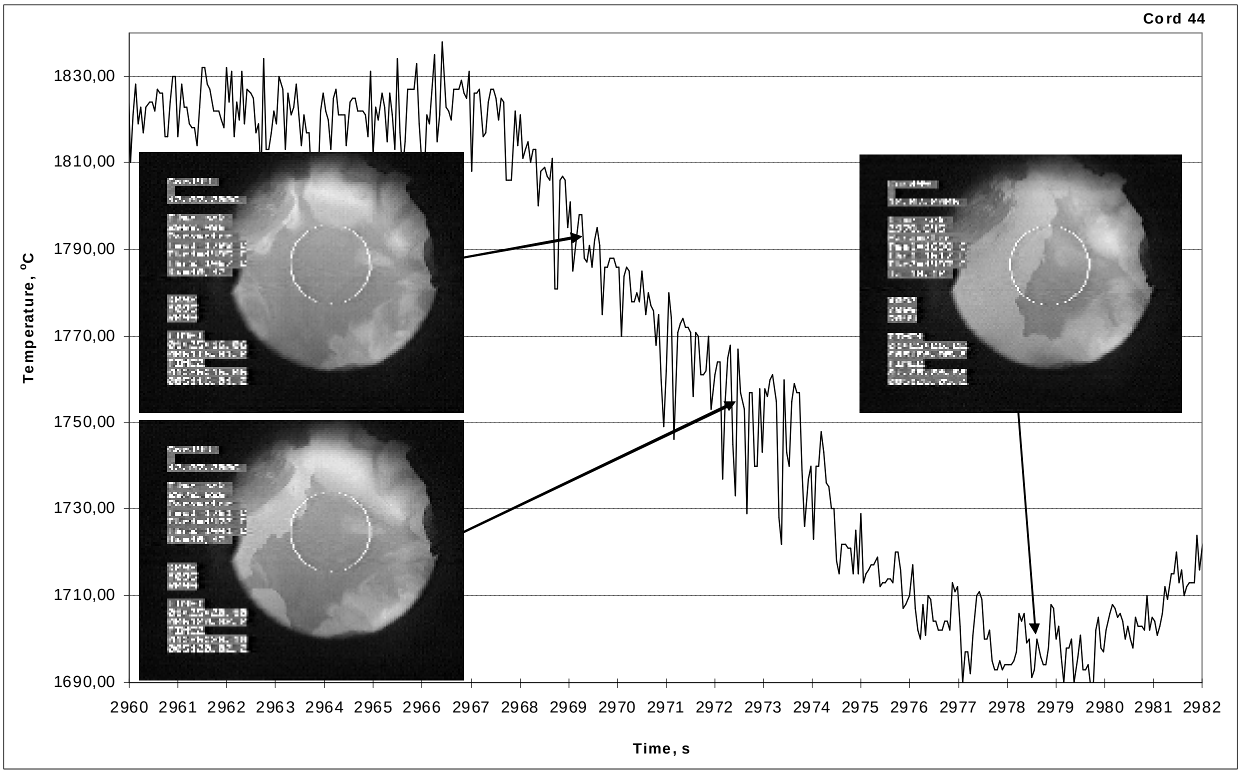

Fig. 3.81. Thermogram with the molten pool surface videoframes from CORD44

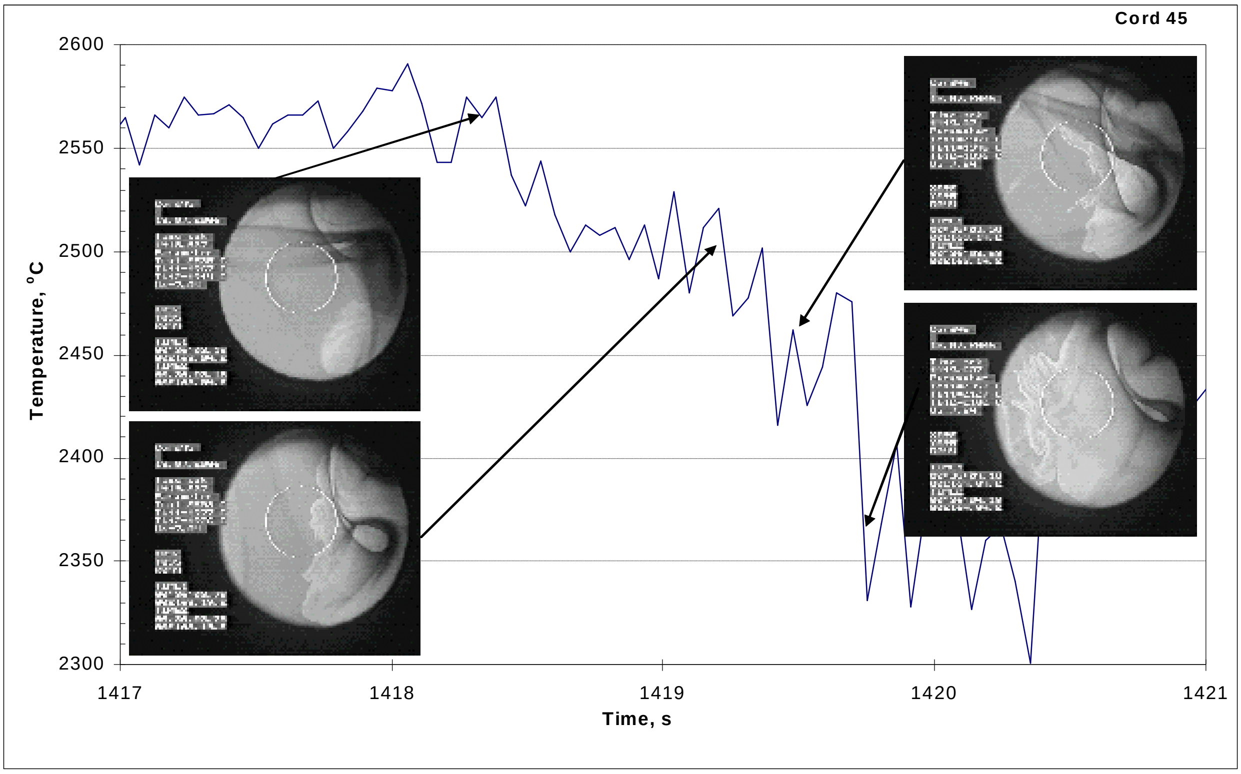

Fig. 3.82. Thermogram with the molten pool surface videoframes from CORD45

Table 3.63. Results of T_{liq} measuring by VPA IMCC in the Zr-Fe-O system

Test	Melt composition calculated from the charge, spillages, debalance and aerosols included, at. %			Melt samples composition, at. % [1]			T_{liq}, °C
	Zr	Fe	O	Zr	Fe	O	
CORD33	50.5	19.8	29.7	-	-	-	2379 2382 2385
CORD35	52.4	19.5	28.2	–	-	-	2380
CORD35[2]				60.3	27.4	12.3	2293
CORD39	46.4	25.3	28.3	-	-	-	2453 2457 2490
CORD44[3]				66.2	30.7	3.1	1770 1780 1790
CORD45	30.9	61.5	7.6	-	-	-	2505 2535

[1] – averaged values from Tab.4.1

[2] - for sample No.3

[3] - for sample No.2

The calculated melt compositions are given for T_{liq} values measured in the tests with melt stratification (CORD33, 35, 39, 45). In CORD44, not all crucible charge melted down, therefore the melt sample composition corresponds to the measured T_{liq}. In CORD35, the long-term equilibrium crystallization of the melt was followed by melt sampling and T_{liq} measurement of the remaining melt.

3.6. X-ray diffraction (XRD)

In order to identify the coexisting phases, the samples from CORD33, 44 and 45 were subjected to XRD using the DRON-3M automatic diffractometer with FeK_{α} emission. Phases were identified by comparison with the standard difractograms from the JCPDS file /25/. Fig. 3.83 shows difractograms of samples prepared from rod samples and from the oxide-rich part of the ingot from CORD33.

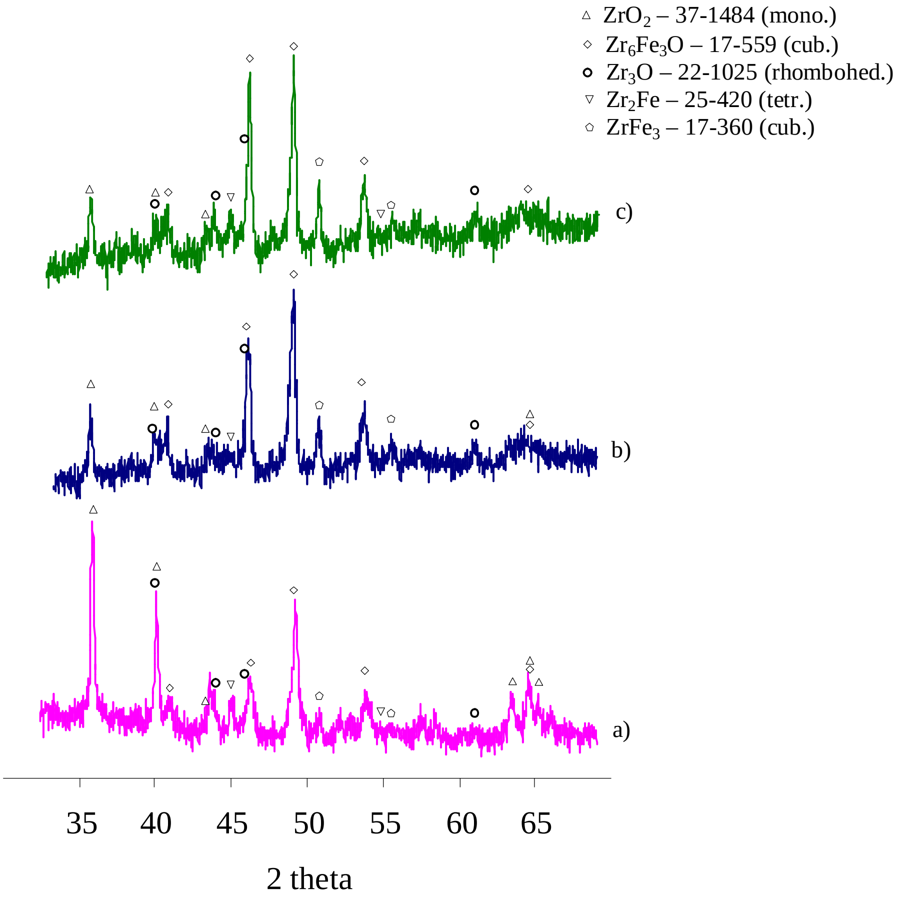

Fig. 3.83. Difractograms of samples from CORD33: a) ingot (oxide-rich part); b) rod sample No.1; c) rod sample No.2

The offered difractograms give a qualitative characteristic of the phase composition of samples from CORD33. Such phases as ZrO_2, α-Zr(O) and Zr_6Fe_3O and a small quantity of intermetallides Zr_2Fe and $ZrFe_2$ (Fig. 3.83, a) have been recorded for the oxide-rich bottom part of the ingot. Two of these phases are nonequilibrium. The same phases, though in different ratios, have been identified in the melt samples corresponding to the metal-rich part of the ingot (Fig. 3.83, b, c).

Fig. 3.84 presents difractograms of the samples prepared from rod samples from CORD44 and 45. Such phases as α-Zr(O), Zr_6Fe_3O, ZrO_2 and Zr_2Fe have been identified for CORD44, and ZrO_2, $ZrFe_2$ and Zr_2Fe for CORD45. Besides, iron may be present in insignificant quantities. In each of these tests one of the phases is nonequilibrium.

The presence of unidentified reflexes in difractograms should be noted. Probably, their presence is related to the existence of oxygen-containing intermetallic compounds, formation of which in this domain of the diagram is possible, but data on them are not available in any literature sources.

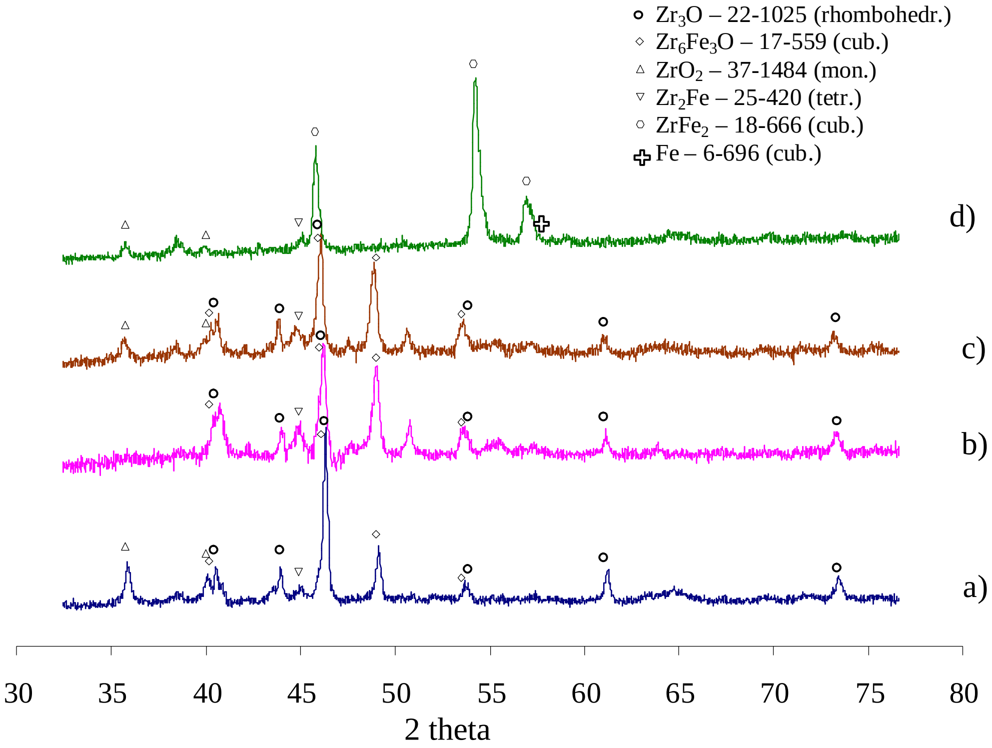

Fig. 3.84. Difractograms of samples from CORD44: a) crust; b) rod sample No.1; c) rod sample No.2; CORD-45: d) rod sample No.2

3.7. Differential Thermal Analysis (DTA)

The method of differential thermal analysis (DTA) was used for T_{sol} determination. Specimen were prepared from the melt samples and ingots from CORD33, 35, 44 and 45. The SETSYS Evolution-2400 analyzer was used for DTA and the SETSOFT 2000 software package for processing the results.

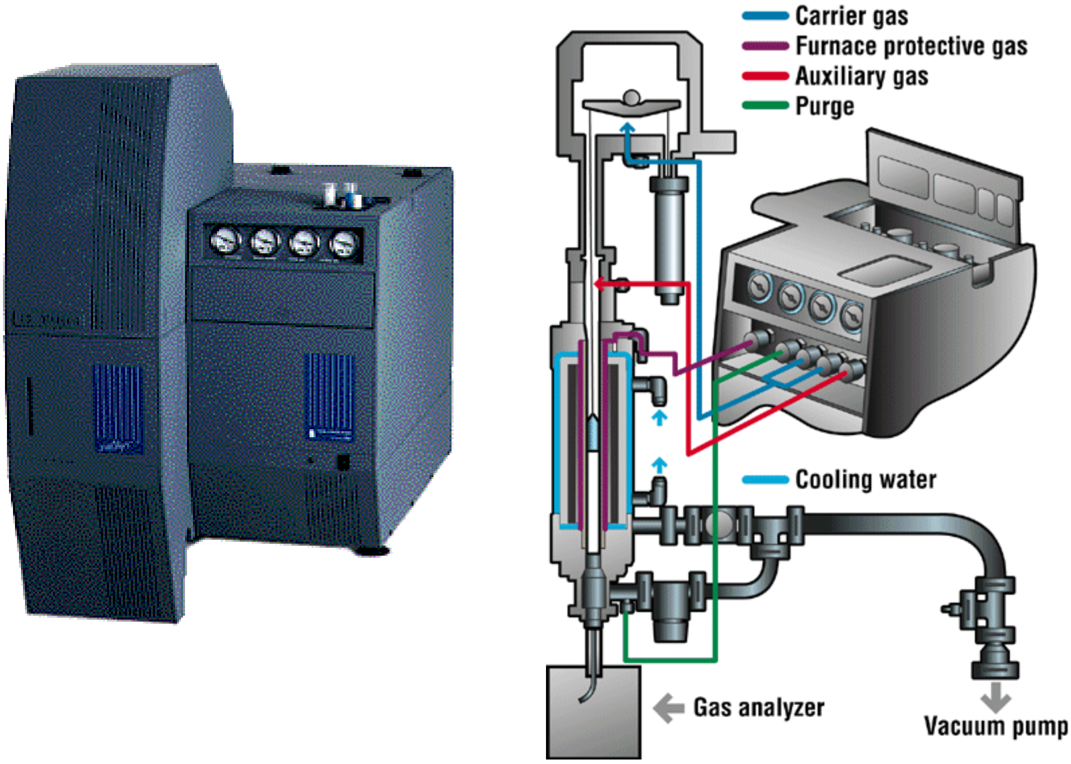

Fig. 3.85. SETSYS Evolution-2400, appearance and schematics

SETSYS Evolution-2400 (Fig. 3.85) covers an extremely wide temperature range from 196°C up to 2400°C and is designed for performing DSC, DTA, TG-DTA and TG-DSC measurements. The accuracy of temperature determination is ±2.5°C. The furnace working space may be either vacuumized, or filled with different gases, e.g., air, argon, helium, carbon dioxide. Such a system provides priceless information about the oxidation-sensitive samples.

The analysis employed alumina crucibles. It should be noted that all samples contain big amounts of intermetallic compounds, since samples for these measurements were taken from metallic parts of the ingots, and this complicates the analysis. T_{sol} of the samples was noted to identify well by this analysis. Interaction with the crucible was recorded upon appearance of the liquid phase, therefore it was impossible to measure T_{liq} by this method. Figs. 3.86–3.90 show fragments of DTA curves with the results of measurements.

<u>Analysis specifications</u>:

The mass of samples was ≈ 38-118 mg, the measuring cell was purged with helium at 4 ml/min. The heating rate was 5°C/min, and a B-type thermocouple (Pt-30%Pt/Rh - 6% Rh) was used.

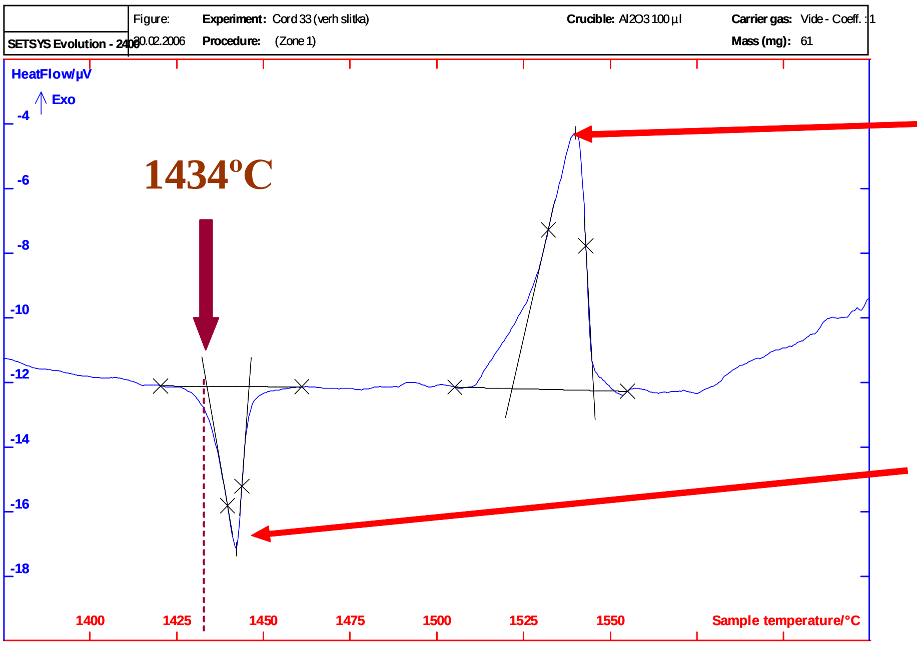

exothermal effect of interaction with crucible a material

endothermic effect of sample melting

Fig. 3.86. DTA curve during heating of the sample from the metal-rich part of the ingot from CORD33

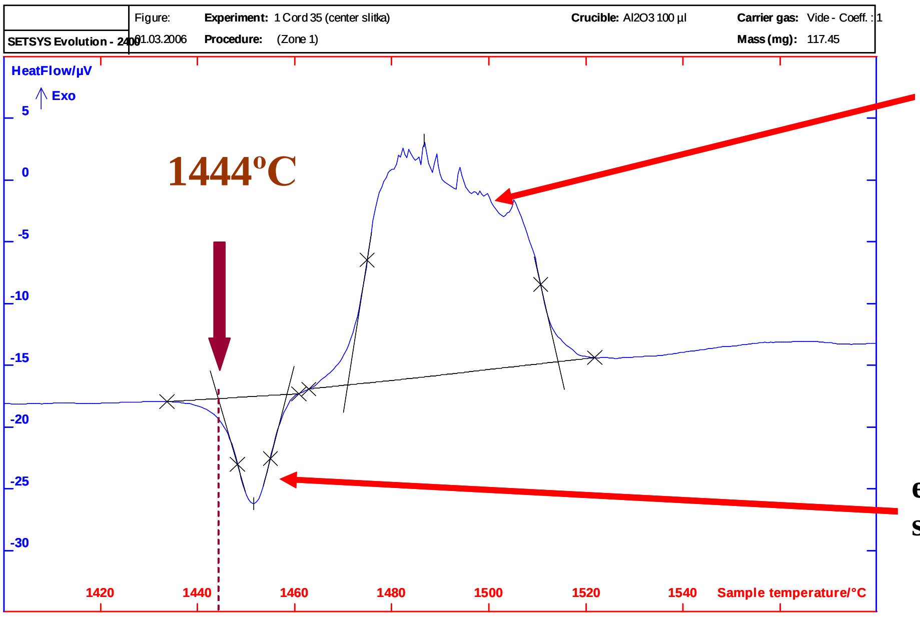

exothermal effect of interaction with crucible a material

endothermic effect of sample melting

Fig. 3.87. DTA curve during heating of the sample from the metal-rich part of the ingot from CORD35

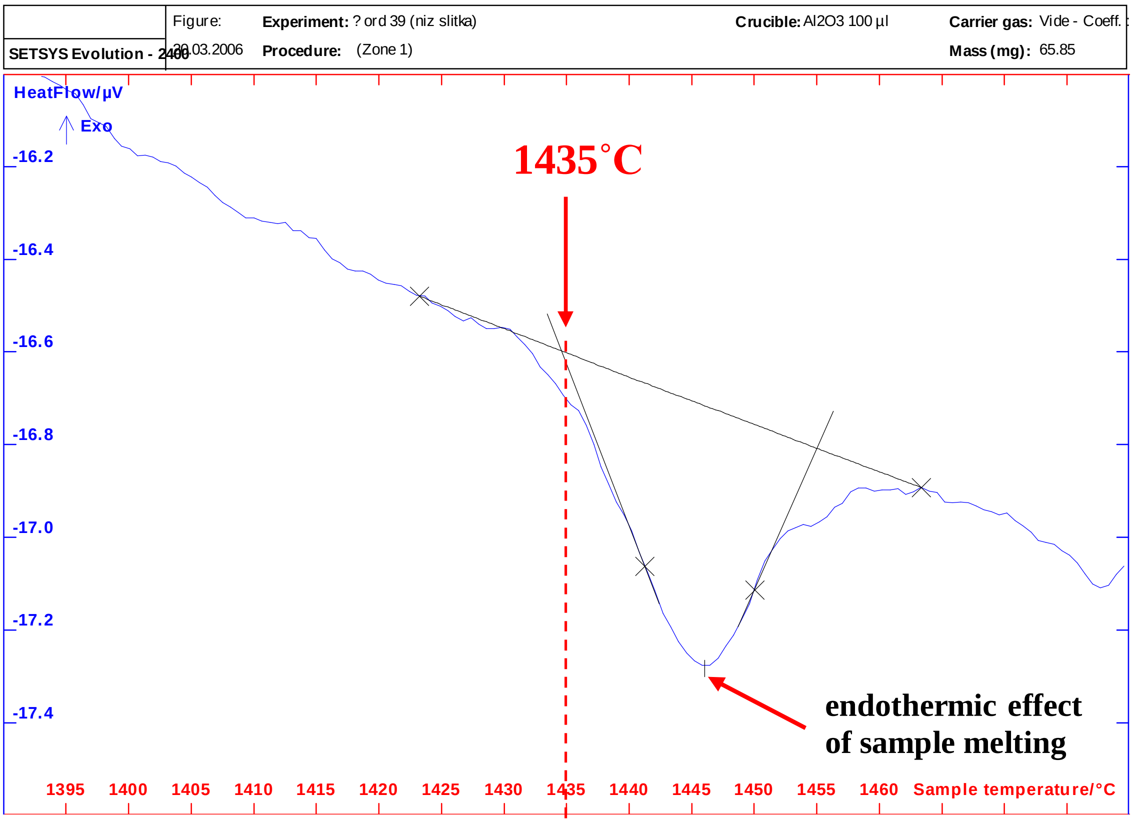

Fig. 3.88. DTA curve during heating of the sample from the metal-rich part of the ingot from CORD39

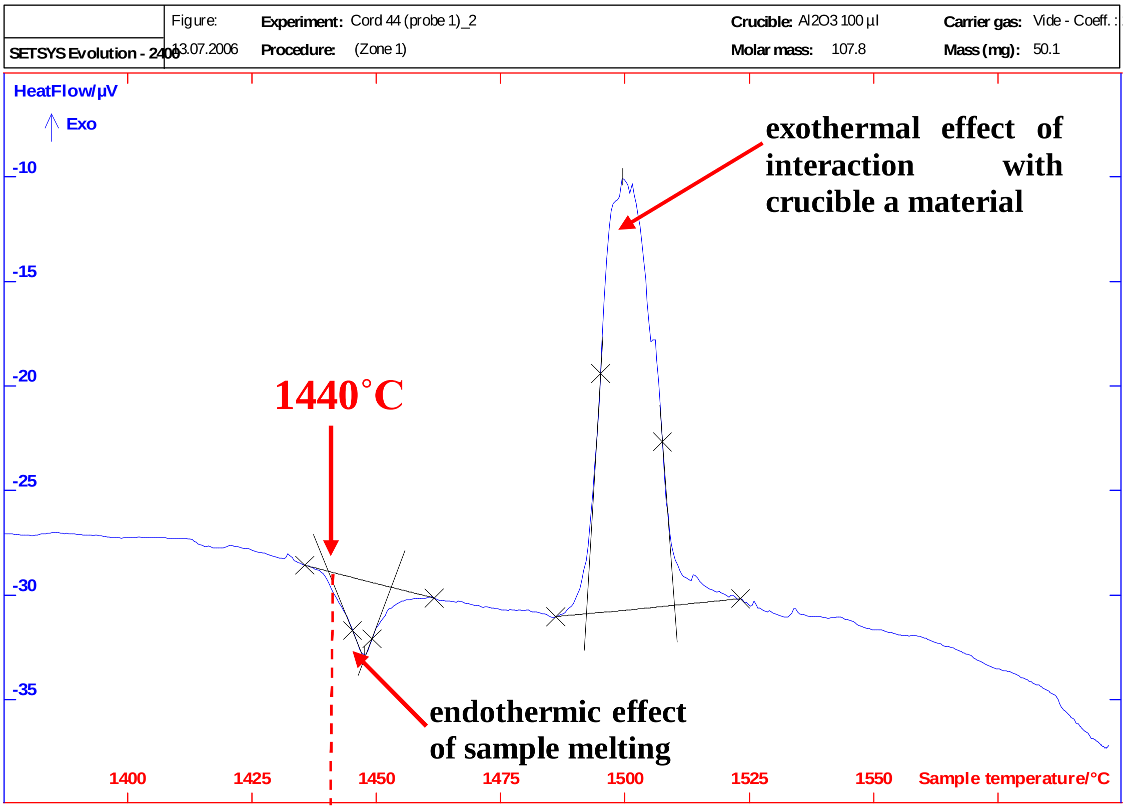

Fig. 3.89. DTA curve during heating of the sample from the ingot from CORD44.

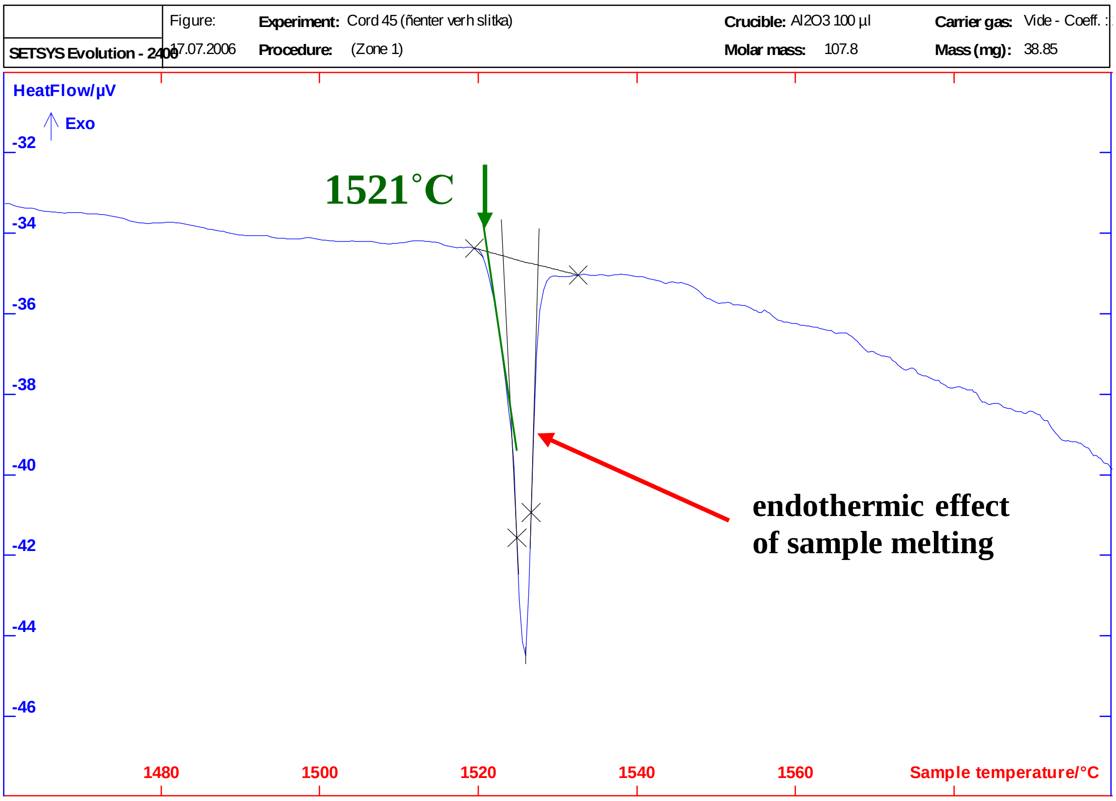

Fig. 3.90. DTA curve during heating of the sample from the ingot from CORD45

This is the way used for measuring T_{liq} at heating the samples. The first endothermic peak is interpreted as a thermal effect during the liquid phase formation (T_{sol} is determined at the point of tangent line crossing with the base line and is automatically registered by the software). The second exothermic peak is interpreted as a thermal effect at the interaction of the sample liquid part with the crucible material. As can be seen from Figs. 3.86 and 3.87, T_{sol} values measured by DTA in CORD33 (T_{sol}=1434°C) and in CORD35 (T_{sol}=1444°C) agree well. Though the melt composition in CORD44 was different from that in CORD33 and 35, it belonged to the particular triangle of concentrations and the value of T_{sol} (1440°C) coincided with the previous measurements. T_{sol} measured for CORD45 has practically coincided with the temperature of pure iron melting (T_{sol}=1521°C).

3.8. Reducing melting of corium samples in carbon crucibles (CTR)

In order to specify oxygen content in the oxidic and metallic parts of ingots, the method of carbothermal reduction (CTR) was applied. The method is described in /13/ and is based on the release of CO–CO_2 at the reduction of the molten sample with carbon, followed by the analysis of the gaseous phase and determining the mass loss. The mass of samples used for the analysis is ~ 500 mg, the exposure time is 1 min at 2500ºC in a neutral atmosphere (argon).

Tab. 3.64 contains the results of measuring oxygen content in samples from CORD30, 33, 35, 39, 44 and 45 together with their averaged values used for correcting compositions of samples and making up the elemental material balances.

Table 3.64. Oxygen content in samples from CORD30, 33, 35, 39, 44 and 45

CORD	Sample	O content, mass %	
		Experimental value	Averaged value
30	Sample No.1	2.69; 2.67	2.68
	Sample No.2	1.88; 1.9	1.89
	Sample No.3	1.55; 1.58	1.57
	Sample No.4	1.77; 1.75	1.76
33	Ingot (oxide.)	14.18; 14.22	14.20
	Ingot (met.)	4.78; 4.57	4.70
	Sample No.3	5.72; 5.69	5.70
35	Sample No.2	5.71; 5.48	5.60
	Sample No.3	2.68; 2.75	2.72
39	Ingot (oxide.)	15.10; 14.32; 14.91; 15.30	14.90
	Ingot (met.)	6.52; 6.35	6.40
	Sample No.1	6.03; 6.45	6.20
	Sample No.2	6.98; 5.82	6.40
44	Ingot (oxide.)	21.05; 21.12; 21.00	21.05
	Ingot (met.)	1.05; 1.11; 0.93	1.03
	Sample No.2	0.65; 0.63; 0.62	0.63
45	Ingot-center	1.69; 1.65; 1.83; 1.88	1.76
	Sample No.1	1.93; 1.95	1.94
	Sample No.2	2.12; 1.84	1.98

4. Discussion of results

The analysis of binary diagrams included in the Zr-Fe-O system, the experience accumulated by the metallurgical industry concerning iron melting in the ZrO_2 crucibles, as well as the thermodynamic predictions indicate the miscibility gap existence in the melts rich in metallic Zr and Fe. There are practically no experimental data for the domain rich in the metals. A series of our tests has shown the existence of the miscibility gap and made it possible to measure T_{liq} of the melts having compositions required for thermodynamic modeling.

The results of physicochemical analysis of rod samples and of those prepared from ingots are summarized in Tab. 4.1. Noteworthy is the scattering of data obtained by different analytical methods. Of importance is the determination of composition of the coexisting liquids, since it were not the liquids, but products of their crystallization that have been analyzed. Mass-transfer processes could occur during crystallization of liquids, and crystallization of an individual liquid could be influenced by the thermogradient conditions of phases and oxygen repartitioning. Therefore, the knowledge of the liquids bulk composition is necessary for determining compositions of the coexisting liquids. Taking into account mass of the material and the impossibility to prepare an averaged sample, for instance, from metal, it can be predicted that the compositions of samples taken from different zones of the ingot may differ from bulk composition. Therefore, data averaging, evaluation of the error of composition determination during the analysis, and various methodological mistakes are of importance.

Table 4.1 Results of analyses for CORD30, 33, 35, 39, 44 and 45

Test	Sample	Zr			Fe			O		
		ChA	XRF	EDX	ChA	XRF	EDX	ChA	XRF	EDX
		at. %								
30	Ingot (top part, metal.)	not determ.	not determ.	49.2	not determ.	not determ.	28.2	not determ.	not determ.	22.6[1]
	Rod sample No.1	58.7	55.7	58.6	29.2	32.5	29.3	12.0	11.9	12.0
	Rod sample No.2	59.5	56.3	58.9	31.9	35.1	32.5	8.7	8.5	8.7
	Rod sample No.3	57.0	55.0	59.4	35.8	37.9	33.3	7.2	7.1	7.3
	Rod sample No.4	59.9	57.3	60.1	32.0	34.7	31.8	8.1	8.0	8.1
33	Rod sample No.2	53.7	52.2	49.5	23.0	24.6	22.5	23.3	23.2	28.0[1]
	Rod sample No.3	54.7	53.1	52.7	21.8	23.6	24.0	23.5	23.3	23.2
	Ingot (top part, metal)	59.6	59.9	54.9	20.1	19.9	25.3	20.2	20.3	19.8
	Ingot (bottom part, oxide)	45.8	47.5	45.8	6.9	4.9	7.0	47.2	47.6	47.2
35	Rod sample No.2	52.8	53.0	52.3	24.3	24.1	24.8	22.9	22.9	22.8
	Rod sample No.3	60.8	59.2	61.0	26.8	28.5	26.7	12.3	12.2	12.3
	Ingot (monophase layer)	not determ.	33.2	33.8	not determ.	0.2	-	not determ.	66.6	66.2[1]
39	Rod sample No.1	46.7	44.7	45.3	29.0	31.3	30.5	24.3	24.1	24.1
	Rod sample No.2	46.8	46.7	45.5	28.2	28.3	29.7	25.0	25.0	24.8
	Ingot (top part, oxide)	45.9	44.3	44.3	5.1	7.1	7.1	49.0	48.6	48.6
	Ingot (bottom part, metal)	49.1	49.6	47.5	25.7	25.1	27.5	25.3	25.3	25.1
44[1]	Rod sample No.1	68.2	67.7	62.7	28.6	29.3	34.3	3.1	3.1	3.0[1]
	Rod sample No.2	68.3	66.9	63.4	28.6	30.0	33.6	3.1	3.1	3.0
	Ingot (central part)	72.8	76.4	64.5	22.1	18.4	30.6	5.1	5.2	4.9
	Above-melt crust	32.8	34.1	34.1	9.0	7.2	7.2	58.2	58.6	58.6[1]
45	Rod sample No.1	30.2	27.3	23.6	62.1	65.1	69.0	7.7	7.6	7.4
	Rod sample No.2	29.9	27.2	24.0	62.3	65.0	68.4	7.8	7.7	7.6
	Ingot (central part)	31.4	30.2	24.6	61.5	62.8	68.6	7.1	7.0	6.8

[1] EDX data not normalized using CTR results for oxygen, as no analysis was made

CORD30 was the first test performed with the investigated system. The induction system was tuned so that superheating of the melt could not be achieved and uncontrolled melt crystallization at the pool bottom was going on in the course of the test. Stabilization of the molten pool was reached only after the refractory component had crystallized at the final stage of the test, and then sample No.4 was taken and T_{liq} measured. The results of the sample No.4 elemental analysis performed by different methods with account for the correction for oxygen according to the CTR data have coincided within the measurement error limits (Tab. 4.1). Tab. 4.4 offers a comparison of T_{liq} measured for the composition of sample No.4 with the value obtained by thermodynamic calculations.

In CORD33 the melt was superheated above the monotectic temperature (2382°C) and homogenized. The measurement of depth and bottom crust thickness speak in favour of complete melting of the specified charge. The SEM/EDX analysis of the polished and etched thin section from the ingot axial cut has clearly shown a boundary between the oxide- and metal-rich parts of the ingot. Physicochemical investigations have shown that the composition of melt samples differs from that of the charge. All these facts confirm stratification of the melt in the liquid state. However, some experimental observations should be mentioned. Firstly, the oxide-rich part of the ingot is located in the bottom part, it being not typical for slags. Secondly, there is virtually no difference in microstructure of the oxide-rich part from CORD33 (Fig. 3.25) and of the crystallized refractory phase from CORD30 (Fig. 3.17). Thirdly, the oxygen content measured for the metal-rich part of the ingot from CORD33 is lower than that measured for sample No.3 (Tab. 4.1). Probably, these observations indicate that like in CORD 30, the refractory phase together with the oxide-rich part of the ingot crystallized prior to the ingot quenching. This supposition prohibits constructing a tie-line on the basis of analytical results for the oxide- and metal-rich parts of the ingot. A thorough analysis of the molten pool thermal condition makes it possible to insist that at the moment of taking all melt samples the pool was in a completely liquid state and crystallization of the refractory phase has probably occurred only after the 3rd sample had been taken in the end of the test. Therefore, the composition of melt samples can help determine composition of the metal-rich liquid that coexists with the oxide-rich one. At the same time, it is impossible to determine composition of the oxide-rich liquid. The results of melt samples analysis performed by different methods show their good agreement (Tab. 4.1). Tab. 4.2 contains averaged values for the metal-rich liquid in sample No.3 from CORD33, for which CTR has been performed and calculations using the GEMINI thermodynamic code made.

In CORD35, crystallization of the melt from the miscibility gap by means of pulling the molten pool out of the inductor at 10 mm/h has yielded an equilibrium layer with the primary crystallization phase. Volume of this layer exceeded that of the oxidic liquid from CORD33. Apparently, the primary crystallization phase was formed of both oxidic and metallic liquids. Analysis of the layer along the ingot height has not revealed any microstructural differences. A possible reason is that the primary crystallization phase is similar for the coexisting liquids. According to the SEM/EDX results, this layer consists of ZrO_2 and α-Zr(O). Most likely, the α-Zr(O) phase formed as the result of prolonged annealing of the primary crystallization phase, that is ZrO_{2-x} –(Fig. 1.3).

Table 4.2. Results of analyses for CORD33 ($Zr_{0.505}Fe_{0.198}O_{0.297}$) and thermodynamic calculation of the coexisting phases composition at 2663K (the temperature of sample No.3 quenching)

CORD	Method of analysis	Element	Experimental		Calculated	
			Oxide-rich liquid	Metal-rich liquid	Oxide-rich liquid	Metal-rich liquid
			Composition, at. %			
33	ChA	Zr	-	54.7	48.5	51.8
	XRF		-	53.1		
	EDX		-	52.7		
	average		-	***53.5±1.2***		
	ChA	Fe	-	21.8	2.7	31.3
	XRF		-	23.6		
	EDX		-	24		
	average		-	***23.1±1.3***		
	XA	O	-	23.5	48.8	16.9
	XRF		-	23.3		
	EDX		-	23.2		
	average		-	***23.3±0.3***		
	Mass fraction, mass %		32.2	67.8	34.7	65.3

The paradoxical phenomenon of the ZrO_{2-x} monophase layer that had formed at crystallization of two different liquids can be explained if one takes into account the nonisothermal nature of the monotectic surface in a ternary system and the univariant crystallization on this surface. In this case, the polythermal cross-section drawn across the crystallizing component (or compound) and traversing the miscibility gap, is similar to the **A-k** section shown in the diagram in Fig. 4.1 /24/. Here, in the **ABC** ternary system, the monotectic transformation of the liquid **L1** yielding the component **A** and **L2** proceeds on the slanting surface **g-h** at a varying temperature, i.e. univariantly. When **L1** gets depleted, crystallization of **A** continues, now from the liquid **L2** on the slanting surface **h-f**, also univariantly**.** Thus, on a nonisothermal monotectic surface crystallization of a melt with two liquids proceeds in the same way as of the homogeneous melt of one of the liquids. Component **A** in the given system corresponds to the compound ZrO_2 in our diagram, while the liquids **L1** and **L2** correspond to the oxide-rich and metal-rich liquids. The inexplicable peculiarity of the equilibrium crystallization is the fact that the primary crystallization phase spreads in the ingot periphery as a practically uniform layer, while in the molten pool the main quantity of this phase is located as a layer presumably in the bottom part.

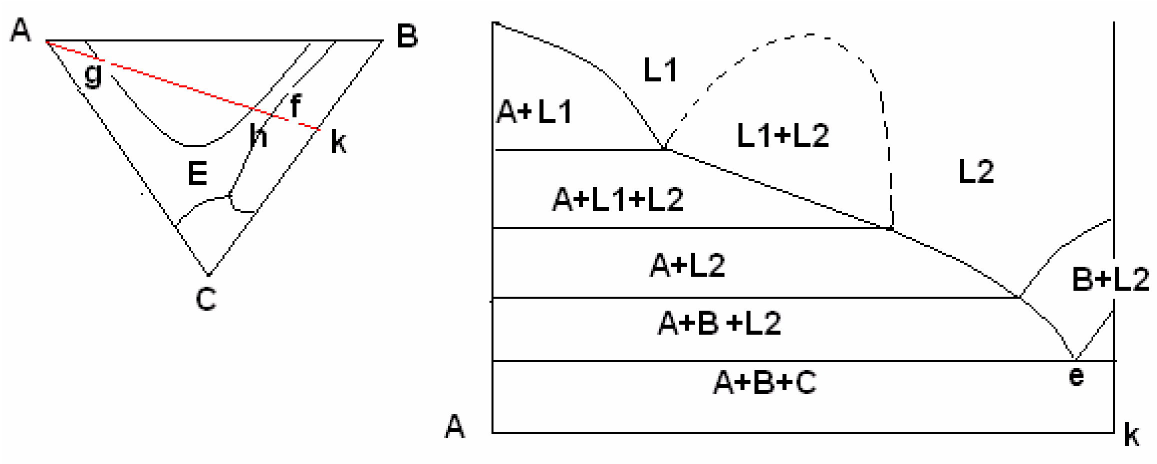

Fig.4.1. Constitution diagram of a ternary system with the miscibility gap /24/

In CORD35, a sample was taken and T_{liq} measured by VPA IMCC after homogenization of the molten pool. A comparison of the melt composition between samples and with T_{liq} values from CORD33 has shown a good agreement between them (Tabs. 4.1 and 4.4). After a long-term extraction of the ingot, melt sample No.3 was taken and T_{liq} measured prior to the HF heating termination. These data are also given in Tab. 4.4.

The work on determining coordinates of a tie-line for the composition differing from that used in CORD33 was continued in CORD39. Microanalysis of the ingot axial section shows that the specified charge had melted down completely, and a boundary between oxide-rich and metal-rich parts is clearly visible. The oxide-rich part of the ingot was located above the metal-rich part. The absence of the oxide-rich liquid at the pool surface as is evident from direct observations during the test, the data on the composition of melt samples taken in the test, and the shape of the crystallized oxide-rich part of the ingot allow a supposition that this liquid was located in the central part of the molten pool and emerged to the surface when heating was switched off.

According to the results of SEM/EDX analysis of samples from CORD39, separation of the second liquid has been registered. Maybe, this is the secondary separation, but a possibility of capturing the second liquid by the rod at melt sampling cannot be excluded. Microstructure of the oxide-rich part of the ingot is dispersed, heterogeneous, characteristic of the monotectic transformation under the conditions of invariant crystallization. The SEM/EDX analysis suggests that the oxidic liquid undergoes the monotectic transformation, when ZrO_{2-x} is the primary crystallization phase (a SEM image shows ZrO_{2-x} to dissociate into ZrO_2 and α-Zr(O) – small light-coloured inclusions against the dark matrix (Fig. 3.52)), and the liquid that coexists with the solid phase has the Zr/Fe ratio equal to 1.5. Microstructure of the metal-rich part of the ingot is dendritic and different regions show separation of what may be regarded as the second liquid. Chemical analysis, XRF and EDX of the composition of samples from different parts of the ingot have shown them to be in good agreement in terms of the cationic composition (Tab. 4.1). The differences in oxygen determination are due to the absence of standard specimens with the fixed oxygen content. Therefore, all analytical results have been normalized using the data on oxygen provided by the CTR analysis. Compositions of the coexisting liquids which have been determined by averaging the data on the oxide-rich and metal-rich parts of the ingot, are presented in Tab. 4.3. Tab. 4.4 offers a comparison of the measured T_{liq} with that calculated using the thermodynamic code.

Tab.4.3. Results of analyses for CORD39 ($Zr_{0.464}Fe_{0.253}O_{0.283}$) and thermodynamic calculation of the coexisting phases composition at 2793K (the temperature of ingot quenching)

CORD	Method of analysis	Element	Experimental		Calculated	
			Oxide-rich liquid	Metal-rich liquid	Oxide-rich liquid	Metal-rich liquid
			Composition, at. %			
39	ChA	Zr	45.9	49.1	45.3	47.2
	XRF		44.3	49.6		
	EDX		44.3	47.5		
	average		***44.8±1.1***	***48.7±1.2***		
	ChA	Fe	5.1	25.7	1.7	40.2
	XRF		7.1	25.1		
	EDX		7.1	27.5		
	average		***6.4±1.3***	***26.1±1.4***		
	ChA	O	49.0	25.3	53.0	12.7
	XRF		48.6	25.3		
	EDX		48.6	25.1		
	average		***48.7±0.3***	***25.2±0.1***		
	Mass fraction, mass %		10.9	89.1	32.1	67.9

In CORD44 not all the charge melted down due to the insufficient power supplied by the used HF equipment. Technologically, the ZrO_2 powder loaded into the crucible appears to be near cold walls of the crucible. In our case, a part of ZrO_2 did not melt down when the maximum possible power was applied. Thus, the molten pool happened to be poorer in oxygen and zirconium. The microphase analysis of a thin section prepared from the axial cut of the ingot has shown a ZrO_2 layer with small amount of iron in the ingot periphery, and homogeneous microstructure in the central part. The fine-grain character of the melt samples microstructure does not make it possible to clearly determine its phase composition, still the XRD analysis of melt samples managed to identify such phases as ZrO_2, α-Zr(O), Zr_2Fe and $Zr_6Fe_3(O)$. It can be said assuredly that the samples contain neither round inclusion characteristic of the stratifying compositions, nor inclusions of the nonmelted phases. During the test the melt was homogeneous and composition of the samples should correspond to the measured T_{liq}. It should be also mentioned that according to the XRD results ZrO_{2-x} is presumably the primary crystallization phase, like in the previous tests. Tab. 4.4 offers a comparison of the measured T_{liq} with that calculated using the thermodynamic code.

In CORD45 all the charge melted down. The microphase analysis of the quenched rod samples has registered spherical inclusions of ZrO_{2-x} with the content of iron (in terms of Zr/Fe ratio) identical to that in the oxide-rich part of the ingot from CORD39. The character of these inclusions allows a supposition that they may exist in the molten pool. Inclusions of ZrO_{2-x} have also been found in the crystallized ingot. The presence of inclusions and their number suggest that the melt was located in the miscibility gap near the binodal. A significant amount of aerosols complicated measurement of T_{liq} of the melt. Therefore, Tab. 4.4 offers the maximum measured value, which may be underestimated.

The results of XRF, ChA, EDX and of CTR for oxygen have been used as the final data on the melt compositions corresponding to the measured T_{liq} values. Besides, the measured T_{liq} and T_{sol} with the results of thermodynamic calculations obtained using the GEMINI-2 code and NUCLEA-05 database (see Tab. 4.4). T_{sol} was measured by the conventional DTA method in alumina crucibles. Sampling for these measurements was don from metallic parts of ingots. The analysis of DTA curves confirms correctness of the performed measurements.

Table 4.4. Experimentally obtained and calculated T_{liq} and T_{sol} values for the melt compositions from CORD30, 33, 35, 39, 44 and 45

CORD	concentration, at.%			experiment		calculation	
	Zr	Fe	O	T_{liq}, K	T_{sol}, K	T_{liq}, K	T_{sol}, K
30[1)]	59.1	32.8	8.1	2125	-	2140	1257
33	50.5	19.8	29.7	2655	1707	2650	1750
35	52.4	19.5	28.2	2653	1717	2620	1750
35[2)]	60.3	27.4	12.3	2293		2266	1369
39	46.4	25.3	28.3	2763	1708	2770	1750
44	66.2	30.7	3.1	2053	1713	2031	1220
45	30.9	61.5	7.6	2808	1796	2923	1759

[1)] - Measurement was made at the final stage of the test after the 'bottom crust - melt' equilibrium had established. Melt composition determined from sample No.4.

[2)] - Measurement was made at the final stage of the test after the 'primary crystallization phase - melt' equilibrium had established. Melt composition determined from sample No.3.

The analysis of T_{sol} in CORD45 shows that this is apparently the temperature of melting of iron, the beads of which have been identified by SEM/EDX.

5. Conclusion

A combination of original and conventional research methods has yielded the first experimental results which characterize the Zr-Fe-O phase diagram in the domain of low oxygen concentrations.

The recommended experimental data on T_{liq} and T_{sol} of different compositions are summarized in Tab. 5.1.

Table 5.1

Concentration, at. %			T_{liq}, K	T_{sol}, K
Zr	Fe	O		
59.1±2.8	32.8±1.7	8.1±0.4	2125±30	-
50.5±2.5	19.8±0.9	29.7±1.4	2655±40	1707±5
60.3±2.9	27.4±1.4	12.3±0.6	2293±35	-
46.4±2.3	25.3±1.2	28.3±1.4	2763±40	1708±5
66.2±3.3	30.7±1.5	3.1±0.1	2053±30	1713±5
30.9±1.5	61.5±3.1	7.6±0.3	2808±70	1796±5

These data agree satisfactorily with the calculated values obtained using the GEMINI-2 code and NUCLEA-05 database.

The presence of the miscibility gap in the system has been confirmed. For the composition $\mathbf{Zr_{0.464}Fe_{0.253}O_{0.283}}$, contents of the liquids that coexist at 2793±42K have been found to be as follows:

- oxidic, at. %, Zr-44.8±2.2; Fe-6.4±0.3; O-48.7±2.4;

- metallic, at. %, Zr-48.7±2.4; Fe-26.1±1.3; O-25.2±1.2.

In the composition $\mathbf{Zr_{0.505}Fe_{0.198}O_{0.297}}$ at 2693±40K, the content of the metallic liquid is: Zr-53.5±2.7; Fe-23.1±1.2; O-23.3±1.2 at. %. Composition of the oxidic liquid has not been identified.

Experimental data on coordinates of tie-lines and position of the miscibility gap differ from predictions made using the GEMINI-2 code. In order to understand this discrepancy and specify data, a significantly wide range of compositions has to be investigated. It should be noted that solubility of iron in the oxidic liquid in the miscibility gap is higher than the predicted.

The obtained information on the character of crystallization of the studied compositions is extensive. In the case of equilibrium crystallization of the liquid composition $\mathbf{Zr_{0.505}Fe_{0.198}O_{0.297}}$ from the miscibility gap, the primary crystallization phase for both oxidic and metallic liquids is the phase ZrO_{2-x}.

6. References

1. NUCLEA. Nuclear Thermodynamic Database. Version 2005-01 / Editor B.Cheynet. THERMODATA 2005.
2. Toropov N.A., Barzakovsky V.P., Bondar I.A. et al. Phase diagrams of silicate systems. Reference book. Issue 2. Metal-oxygen compounds of silicate systems. Nauka Publishers, Leningrad. 1969. 372 P. (in Russian).
3. Domagala R.F., McPherson D.J. // Trans. AIME. 1954. V. 200. P. 238.
4. Gebhardt E., Seghezzi H.-D., Dürrschnabel W. Untersuchungen im System Zirkonium-Sauerstoff. Teil 1. Der Elektrische Widerstand von Sauerstoffhaltigem Zirkonium. // J. Nucl. Mat. 1961. V. 4. № 3. P. 241–254.
5. Gerhardt E., Seghezzi H.-D., Dürrschnabel W. Untersuchungen im System Zirkonium-Sauerstoff. Teil 2. Untersuchungen zur Kinetik der Reaktion Zwischen Zirkonium und Sauerstoff, Sowie über die Konstitution des Systems Zirkonium Sauerstoff. // J. Nucl. Mat. 1961. V.4. N 3. P. 255–268.
6. Ackermann R.J., Garg S.P., Rauh E.G. High-temperature phase diagram for the system Zr–O // J. Am. Ceram. Soc. 1977. V. 60. No. 7-8. P. 341-345.
7. Abriata J.P., Barces J., Versaci R.. The O–Zr (Oxygen–Zirconium) system // Bull. Alloy Phase Diagrams. 1986. V.7. P. 116-123.
8. Arroyave R, Kaufman L., Eagar T.W.. Thermodynamic Modeling of the Zr–O system // CALPHAD. 2002. V. 26. N. 1. P. 95-118.
9. Phase diagrams of metallic systems. Issue XLI/103. Moscow. 1999. NUCLEA HANDBOOK of PHASE DIAGRAMS. Nuclear Thermodynamic Database Thermodata Version 2003-01.Developed by THERMODATA – INPG – CNRS and AEA – Technology. Editor B. Cheynet. France. 2003.
10. Wriedt H.A. The Fe–O (Iron–Oxygen) system /J. Phase Equilibria. 1991. V. 12. No. 2. P. 170-200.
11. Jones T., Kimura S., Muan A. … // J. Amer.Cer.Soc. 1967. V. 50. N 3. P. 137.
12. Y. Petrov, J. Slovak, J. Sussmilch, R. Rybka, J. Brozik. *“Preparation of a furnace and experimental technique to a prototypic corium melting.* Report SAM-ECOSTAR - M14/01, Project ECOSTAR, Contract FICS-CT1999-00003. (EC 5-th Framework). NRI, Rez, Czech Republic. (2001).
13. Investigation of ternary oxidic systems. System U–Zr–O. / In: ISTC PROJECT No. 1950.2. Final report.
14. Khabensky V.B. et al. Phase diagrams for multicomponent systems containing corium and products of its interaction with NPP materials (CORPHAD). Phase 2. 1st year. Annual technical report No. 1-1950.2-2004 (Appendix 1. Investigation of binary oxidic systems. The UO_2-FeO system) // NITI.
15. Butyrin G.M. Highly porous carbonic materials. Moscow. Khimiya (Chemistry), 1976 (in Russian).
16. GOST 12365-84 Alloy and high-alloy steels. Methods for determination of zirconium. (in Russian)
17. Yelinson S.V., Nezhnova T.I. // Factory laboratory. Vol. 30, No.4, 1964. P. 396-399. in Russian)

18. Goryushina V.G., Romanova E.V., Archakova T.A. // Factory laboratory. Vol. 27, No.7, 1961. P.795-797 (in Russian)
19. GOST 4011-72. Drinking water. Methods for determination of total iron. (in Russian)
20. Sendel E. Methods of metal traces determination by colorimetry. Moscow, Mir Publishers, 1964. P. 902. (in Russian)
21. Yeremina B.G. Gas analysis. Moscow, Mir Publishers. 1955. (in Russian)
22. Baksanova L.E., Budnikov V.I., Valtsifer V.A. Gas volumetric method of active aluminium determination in polymeric materials. Factory laboratory. No.7, Vol. 66. 2000. (in Russian)
23. Losev N.F. Quantitative X-ray fluorescence analysis. Moscow, Nauka Publishers, 1969. P.336. (in Russian)
24. V.Ya. Anosov, M.I. Ozerova, Yu.Ya. Fialkov. Fundamentals of physicochemical analysis. Moscow, Nauka Publishers, 1976. P. 503. (in Russian)
25. JCPDS 6-696, 17-360, 17-559, 18-666, 22-1025, 25-420, 37-1484.